



**VALIDATION AND CHARACTERIZATION
OF IONOSPHERIC DENSITIES
MEASURED BY DMSP**

THESIS

Herbert L. Keyser, Captain, USAF

AFIT/GAP/ENP/01M-05

**DEPARTMENT OF THE AIR FORCE
AIR UNIVERSITY**

AIR FORCE INSTITUTE OF TECHNOLOGY

Wright-Patterson Air Force Base, Ohio

APPROVED FOR PUBLIC RELEASE; DISTRIBUTION UNLIMITED.

20010730 038

The views expressed in this thesis are those of the author and do not reflect the official policy or position of the United States Air Force, Department of Defense, or the U. S. Government.

AFIT/GAP/ENP/01M-05

VALIDATION AND CHARACTERIZATION
OF IONOSPHERIC DENSITIES
MEASURED BY DMSP

THESIS

Presented to the Faculty
Department of Engineering Physics
Graduate School of Engineering and Management
Air Force Institute of Technology
Air University
Air Education and Training Command
In Partial Fulfillment of the Requirements for the
Degree of Master of Science in Applied Physics

Herbert L. Keyser, B.S.

Captain, USAF

March 2001

APPROVED FOR PUBLIC RELEASE; DISTRIBUTION UNLIMITED.

AFIT/GAP/ENP/01M-05

**VALIDATION AND CHARACTERIZATION
OF IONOSPHERIC DENSITIES
MEASURED BY DMSP**

Herbert L. Keyser, B.S.

Captain, USAF

Approved:

Devin J. Della-Rose

Devin J. Della-Rose (Chairman)

1 Feb 01

date

Wm. F. Bailey

William F. Bailey (Member)

5 Mar 01

date

Jan J. Sojka

Jan J. Sojka (Member)

1 Feb 01

date

Acknowledgments

I would like to express my sincere appreciation to my faculty advisor, Maj. Devin Della-Rose, for his guidance and support throughout the course of this thesis effort. His insight and experience were certainly appreciated. Also, I would like to thank my committee, Dr. William F. Bailey and Dr. Jan Sojka; their insight and direction were critical to my effort. I would be remiss without thanking the entire Engineering Physics faculty and staff for the knowledge and wisdom they tried to impart to me during my short stay at AFIT. I want to thank Dr. Mark Hairston from the University of Texas at Dallas for the DMSP SSIES data, Dr. Phil Erickson from the Millstone Hill Observatory, and Mary McCready from SRI International for their Incoherent Scatter Radar data from the Millstone Hill and Sondrestrom radars, respectively. This thesis would have been impossible without their data and expertise. Of course, thanks to Capt Brad Green who, while working on a complementary topic, kept me honest by questioning all my results, ensuring a better research outcome.

The list of people who helped me is innumerable, but I'd like to specifically thank Drs. Peter Sultan and Fred Rich from the Air Force Research Laboratory and Dr. Barbara Emery from the National Center for Atmospheric Research's High Altitude Observatory (and CEDAR guru), who took the time to help when needed and not laugh at me when I asked the obvious.

I am perennially indebted to my wife, _____ for her understanding and patience-not only during this research effort but also throughout our marriage. She is a constant source of inspiration and support in all I do.

Herbert L. Keyser

Abstract

Future models of the thermosphere-ionosphere-magnetosphere system will require near real-time assimilation of ionospheric parameters to specify and forecast these regions. One of the current sensors that will be used in the GAIM model is the DMSP SSIES. Knowledge of the SSIES's reliability and data characteristics is key to using the data when relying on automated processes to ingest the data. To validate the DMSP value, the DMSP-measured density is compared to ground-based ISR measurements from solar minimum to solar maximum. The DMSP data are compared to data from the ISRs located at the Millstone Hill Observatory in Massachusetts and Sondrestrom in Greenland. The DMSP was found to measure densities 10 percent - 20 percent lower than Millstone Hill and 90 percent lower than Sondrestrom, however both were within the uncertainties of the ISR measurements. The DMSP data over Millstone Hill were analyzed for variability. After de-trending the data, the variability was found to range from 0.2 percent in geomagnetically quiescent periods to over 20 percent during active periods.

Table of Contents

<u>Section</u>	<u>Page</u>
Acknowledgments.....	iii
Abstract	iv
List of Abbreviations.....	vii
List of Figures	ix
List of Tables.....	xi
I. Introduction.....	1
1.1 Problem Statement	1
1.2 Research Objectives	2
1.3 Air Force Impact	3
II. Background.....	4
2.1 The Ionosphere.....	4
2.1.1 General Description.....	4
2.1.2 Global Structure of the Ionosphere	6
2.1.3 Ionospheric Electrodynamics.	10
2.1.4 The Subauroral Ion Drift.....	11
2.1.5 The Mid-Latitude Trough.....	12
2.1.6 The Light Ion Trough.....	15
2.1.7 The Aurora.	17
2.2 Incoherent Scatter Radar	17
2.3 POLITE Campaigns	23
2.4 Defense Meteorological Satellite Program (DMSP).....	24

2.5 GAIM Proposal	31
III. Methodology	33
3.1 Prior Research	33
3.2 Description of ISR data	34
3.2.1 Millstone Hill.	34
3.2.2 Sondrestrom.	37
3.3 Description of DMSP Data	38
3.4 Comparison of ISR and DMSP Data.....	41
IV. Results and Analysis	49
4.1 Comparison of DMSP <i>versus</i> ISR.....	49
4.1.1 Millstone Hill Overpasses	49
4.1.2 Millstone Hill Case Study.	64
4.1.3 Sondrestrom Overpasses	67
4.2 Density Variations in the DMSP Measurements.....	70
V. Conclusions and Recommendations.....	77
5.1 Conclusions	77
5.2 Recommendations	79
Appendix A: Millstone Hill Comparison	81
Appendix B: Sondrestrom Comparison	105
Appendix C: Ionospheric Layers.....	110
Appendix D: The Air Force Research Laboratory Auroral Boundary Index.....	115
Bibliography.....	117
Vita.....	119

List of Abbreviations

CEDAR	Coupling, Energetics, and Dynamics of Atmospheric Regions
e	unsigned charge on an electron
EQB	The Air Force Research Laboratory Auroral Boundary Index (Equivalent Midnight Equatorward Boundary)
EISCAT	European Incoherent Scatter Radar
DMSP	Defense Meteorological Satellite Program
DNEL	Error in Corrected Electron Density
DPOPL	Error in Uncorrected Electron Density measurement
DTe	Error in measured Electron Temperature
DTi	Error in measured Ion density
ϵ_0	permittivity of free space
EP	Electron Probe (Langmuir Probe)
GAIM	Global Assimilation of Ionospheric Measurements
k_B	Boltzmann's Constant
IMF	Interplanetary Magnetic Field
ISR	Incoherent Scatter Radar
LIT	Light Ion Trough
m_e	electron mass
MLH	Haystack Observatory Millstone Hill ISR
MSIS	Mass Spectrometer Incoherent Scatter Model
MT	Mid-latitude Trough (Main Trough)

N_e	Electron Concentration
NEL	Corrected Electron Density
NOAA	National Oceanographic and Atmospheric Administration
NPOES	National Polar Orbiting Environmental Satellite
NSF	National Science Foundation
POLITE	Plasmaspheric Observation of Light Ions in the Topside and Exosphere
POPL	Uncorrected Electron Density
RPA	Retarding Potential Analyzer
SAID	Sub-Auroral Ion Drift
SENROT	Sensor Potential from SSIES
SM	Scintillation Meter
SSIES	Special Sensor for thermal Ions, Electrons, and their Spatial variations (Topside Ionospheric Plasma Monitor)
SON	Sondrestrom ISR
T_e	Electron Temperature (K)
T_i	Ion Temperature (K)
Λ	Invariant Latitude

List of Figures

<u>Figure</u>	<u>Page</u>
Figure 1: Vertical profile of the Ionosphere.....	5
Figure 2: Structure of the high-latitude ionosphere	7
Figure 3: Typical density structure of the ionosphere.....	8
Figure 4: DMSP density plot showing He+-predominance from 54° to 58° Λ.	9
Figure 5: Signature of SAID event from the Dynamics Explorer 2 satellite	12
Figure 6: Mid-latitude trough.....	15
Figure 7: LIT demonstrated by isometric projection of H+ and Ni profiles	16
Figure 8: The power spectrum of radio waves incoherently backscattered by the ionosphere	19
Figure 9: The power spectrum of the incoherent scatter echoes when T_e exceeds T_i	20
Figure 10: Map of ISR sites worldwide	22
Figure 11: Location of Nominal DMSP Ascending/Descending Nodes.....	25
Figure 12: SSIES/SSIES2 sensors mounted on the DMSP spacecraft	27
Figure 13: External view of the SSIES2 ion sensors	28
Figure 14: Total Ion Density Sensor (Scintillation Meter)	29
Figure 15: Retarding Potential Analyzer.....	30
Figure 16: Example of one complete DMSP orbit.....	40
Figure 17: Example of Incoherent Scatter Radar Returns.....	44
Figure 18: Example of random noise associated with DMSP.....	50

Figure 19: DMSP-measured (a) density, (b) velocity, and (c) T_e for case M1-1.....	52
Figure 20: DMSP-measured (a) density, (b) velocity, and (c) T_e	53
Figure 21: Millstone Hill conjunctions showing ISR and DMSP measurements.	55
Figure 22: DNEL / NEL for Millstone Hill 1000 μ sec pulse length at 874 km.....	56
Figure 23: DNEL / NEL for Millstone Hill 2000 μ sec pulse length at 844 km.....	57
Figure 24: DMSP σ / DMSP Average for Millstone Hill Overpasses.	58
Figure 25: Relative error DMSP v. MLH 1000 μ sec measured at 874 km.	59
Figure 26: Relative error DMSP v. MLH 2000 μ sec measured at 844 km.	60
Figure 27: Case M2-1, 2000 μ sec. Case of fit performing better than measured data....	61
Figure 28: Relative error DMSP v. MLH 1000 μ sec fit data at DMSP altitude.	62
Figure 29: Absolute error DMSP v. MLH 1000 μ sec fit.....	62
Figure 30: Relative error DMSP v. MLH 2000 μ sec fit at DMSP altitude.....	63
Figure 31: Relative error DMSP v. MLH 410 μ sec fit at DMSP altitude.....	64
Figure 32: Sondrestrom conjunctions showing ISR and DMSP measurements	68
Figure 33: DMSP σ / DMSP Avg for Sondrestrom Overpasses.....	68
Figure 34: DNEL/NEL for Sondrestrom at 840 km.....	69
Figure 35: Relative error DMSP v. SON near 840 km.....	70
Figure 36: M9-1 shows too much physical structure for a linear fit.	73
Figure 37: M2-2 shows linear fit removing good data.....	74
Figure 38: Examples requiring another application of filtering algorithm.	75

List of Tables

<u>Table</u>	<u>Page</u>
Table 1: ISR Radar Locations	22
Table 2: POLITE Campaign Dates	23
Table 3: Local Times of DMSP Overpass	25
Table 4: Millstone Hill Data Description	35
Table 5: DMSP Data Description	38
Table 6: Ionospheric features found during Millstone Hill overpasses.....	54
Table 7: Comparison of case study measurements	65
Table 8: Comparison of the upper bound error propagation formula to the lower bound error propagation formula for selected Millstone Hill cases.....	66
Table 9: DMSP Density Variability	76
Table 10: Case M1-1	83
Table 11: Case M1-2	83
Table 12: Case M2-1	84
Table 13: Case M2-2	84
Table 14: Case M2-3	85
Table 15: Case M3-1	85
Table 16: Case M3-2	86
Table 18: Case M3-4	86
Table 19: Case M3-5	87
Table 20: Case M4-1	87

Table 21: Case M4-2	88
Table 22: Case M4-2 Modified Error.....	88
Table 23: Case M4-3	89
Table 24: Case M4-3 Modified Error.....	89
Table 25: Case M4-4.....	90
Table 26: Case M4-5.....	90
Table 27: Case M5-1	91
Table 28: Case M5-2.....	91
Table 29: Case M5-3	92
Table 30: Case M5-4	92
Table 31: Case M6-1	93
Table 32: Case M6-2.....	93
Table 33: Case M6-3	94
Table 34: Case M7-1	95
Table 35: Case M7-1 Modified Error.....	95
Table 36: Case M7-2.....	96
Table 37: Case M7-2 Modified Error.....	96
Table 38: Case M7-3	97
Table 39: Case M8-1	97
Table 40: Case M8-2.....	98
Table 41: Case M8-3	98
Table 42: Case M9-1	99
Table 43: Case M10-1	99

Table 44: Case M10-2	100
Table 45: Case M10-3	100
Table 46: Case M10-4	101
Table 47: Case M10-5	101
Table 48: Case M10-6	102
Table 49: Case M10-7	103
Table 50: Case M10-7 Modified Error.....	103
Table 51: Case 10-8	104
Table 52: Case M10-8 Modified Error.....	104
Table 53: Case S2-1	106
Table 54: Case S3-1	106
Table 55: Case S3-2	107
Table 56: Case S5-1	107
Table 57: Case S5-2	108
Table 58: Case S8-1	108
Table 59: Case S9-1	109
Table 10: Ionospheric Layers and Their Properties	110
Table 11: EQB Regression Statitics.....	116

**VALIDATION AND CHARACTERIZATION
OF IONOSPHERIC DENSITIES
MEASURED BY DMSP**

I. Introduction

1.1 Problem Statement

The next generation space environment models will combine physics-based algorithms with near real-time data from both ground- and space-based sensors. To date, such data assimilation has been accomplished on a very limited basis. This effort will require an in-depth knowledge of the data characteristics. Characterization of the data from the various sensor systems -- such as the Defense Meteorological Satellite Program's (DMSP) Topside Ionosphere Plasma Monitor (SSIIES) -- will be required to accurately initialize the physical models. Also, since much of the data will be ingested automatically with a minimal amount of human intervention, characterization of the expected error--as well as the dynamic range away from climatology during geomagnetic storm conditions--will be required.

1.2 Research Objectives

There are two distinct parts of this research. The first will essentially expand the previous work of Sultan and Rich (2000) that compared DMSP-measured ionospheric densities against that measured by the Incoherent Scatter Radar (ISR) located at the Millstone Hill Observatory, a geomagnetic mid-latitude station. Their study looked at DMSP satellites F08, F09, and F10 during 1989 and 1991, near the maximum of Solar Cycle 22. They found the SSIES measured ionospheric densities within the advertised 10 percent error of the instruments, compared to the ISR. This research will extend the comparison to Millstone Hill covering the period from before solar minimum (solar minimum is taken to be winter 1996) to solar maximum (summer 2000) of Solar Cycle 23, the current solar cycle. Also it will briefly compare the SSIES densities against data from the Sondrestrom ISR located at higher latitude in the auroral oval during the day and the polar cap region at night.

The second objective of the research will examine over 1100 sets of data, each representing one orbit from five DMSP satellites and perform initial instrument error estimates. The Global Assimilation of Ionospheric Measurements (GAIM) project will initially require these error estimates for the SSIES data to be specified in five-degree latitude increments for the entire globe, further delineated into whether the sensor is sunlit or eclipsed. Additional grouping of the data to determine whether the satellite is poleward of the equatorward auroral boundary or not will help in this characterization effort.

1.3 Air Force Impact

The Air Force, the entire Department of Defense, and many civilian interests are affected by the evolving structure of the ionosphere. Ionospheric irregularities can distort the propagation of trans-ionospheric radio waves. Beyond line-of-site communications and over-the-horizon radar rely on the ionospheric plasma to refract and reflect the long wavelength radio waves. Irregularities in the plasma affect the reliability of HF and satellite communication, two systems critical to today's war-fighters. Also, the composition and dynamics of the magnetosphere-ionosphere system are intimately linked to the well being of personnel conducting manned space flight, not to mention the integrity and operation of the space vehicles themselves. Changes in the neutral density and extent of the ionosphere-thermosphere system can cause drag on satellites that can shorten their operational lifetime and change their expected location, whereas decreases in the plasma density even at DMSP altitudes can lead to significant spacecraft charging. Also, currents in the ionosphere cause unexpected, magnetically induced currents in ground-based power grids, which can lead to unexpected fluctuations in power grids, and possibly the entire grid shutting down.

This initial effort to characterize DMSP measurements will be integrated into future real-time specification and forecasting of the ionosphere. An accurate and timely model of the current conditions from satellite and other measurements will help operators predict and exploit ionospherically induced effects on friendly as well as enemy systems.

II. Background

2.1 The Ionosphere

2.1.1 General Description. The ionosphere is a weakly ionized plasma that extends from approximately 100 km to 1000 km, and is composed of ionized and neutral atoms, molecules, and the associated free electrons. As with most plasmas, the ionosphere is quasi-neutral, so the total number of positive ions of all species is nearly equal to the sum of electrons and negative ions. The ionosphere is created principally via photoionization with some additional ionization attributable to high-energy particle precipitation. It is maintained by a complex interplay of chemistry and transport.

The ionosphere was initially discovered at the turn of the 20th century shortly after the advent of radio communications. The existence of a charged layer in the atmosphere was proposed to explain the propagation of radio waves across the Atlantic Ocean. It was proposed independently by Heavyside and Kennelly to explain how radio waves could be received beyond the range predicted by refraction through the earth's atmosphere. Hence, from its earliest classification up through the 1960s, it was referred to as the Kennelly-Heavyside layer. Experimentation by Appleton and Barnett proved the existence of this layer. (Evans, 1975)

Further experiments over the years brought about the discovery of several ionized layers in the atmosphere which in modern times are designated the D, E, F₁, and F₂ layers. Each layer is characterized by the ionization source, the predominant ions, and the chemistry involved in these processes. See Appendix C for details of the composition and structure of the lower ionospheric layers.

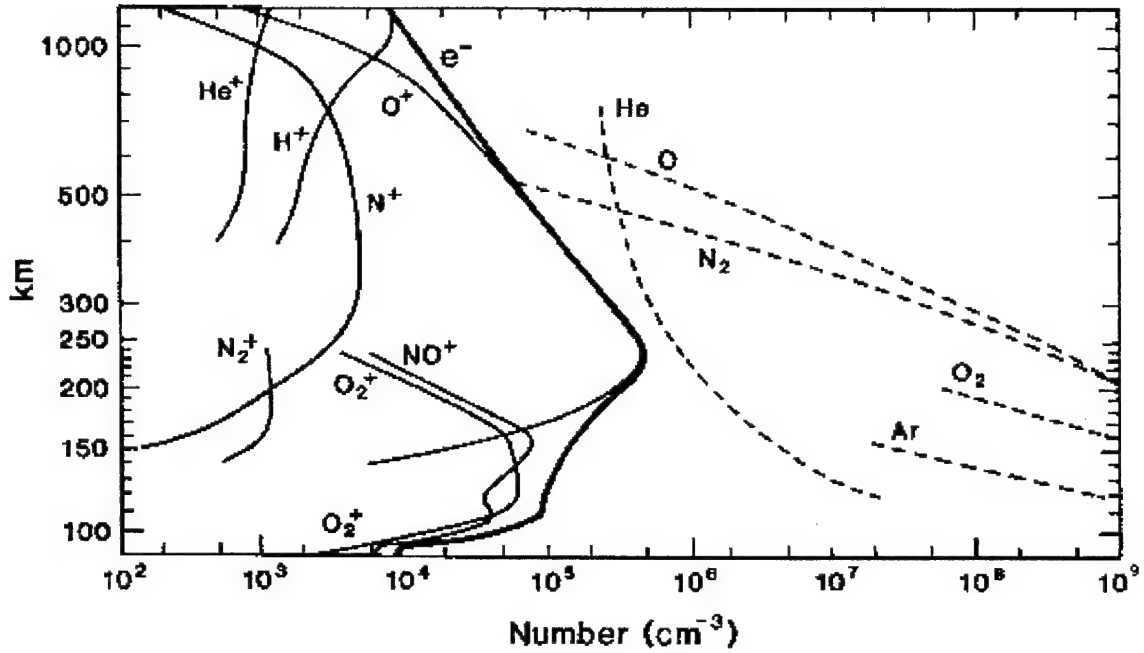


Figure 1: Vertical profile of the Ionosphere (From Kivelson and Russell, 1996)

The topside of the ionosphere is defined as the region above the F₂ peak where O⁺ dominates, which can extend 600 km to 1500 km above the F₂ peak (Schunk and Nagy, 2000:333). Above this H⁺ is predominant, and the region is termed the protonosphere or plasmasphere. When sufficient numbers of O⁺ exist (low altitudes), chemical equilibrium is the predominant process, and the reversible charge exchange reaction



controls the relative density of O⁺ and H⁺. H⁺ density can be obtained by the equation (Schunk and Nagy, 2000:334):

$$[H^+] = 1.13 * \frac{[O^+][H]}{[O]} \quad (2)$$

where the coefficient represents the ratio of the forward to reverse reaction rates. Given that oxygen is sixteen times heavier than hydrogen, O⁺ decreases exponentially more

rapidly with altitude than hydrogen. As a result, H^+ increases exponentially with altitude until O^+ is no longer a major constituent. Diffusive equilibrium controls the topside above this level, when the decreasing H^+ pressure in the plasmasphere helps decrease both the density and pressure of ionospheric H^+ , especially at high latitudes.

Thermal diffusion can be important when the density structure is controlled by diffusive equilibrium. The transfer of heat energy between the various constituents when there are large temperature gradients helps separate the light and heavy ions. The O^+ move up in altitude toward higher energy and the light H^+ ions downward toward cooler temperatures. This transport of O^+ can have the effect of raising the transition height from heavy to light ions several hundred kilometers (Schunk and Nagy, 2000:335).

Above the plasmasphere is the magnetosphere. The magnetosphere is the region where the earth's magnetic field interacts with the Interplanetary Magnetic Field (IMF) originating from the sun. The magnetosphere effectively shields the earth from the direct effects of the solar wind and traps some of the high-energy solar wind plasma. The ionosphere connects to the magnetosphere through the magnetic and electric fields. At the earth's magnetic dipole, the magnetosphere and plasmasphere interact more readily with the upper reaches of the atmosphere. The cusp region occurs 10 degrees to 15 degrees south of the magnetic pole on the dayside and in this region the ionosphere is linked to the magnetosphere and IMF and high-energy particles can penetrate to the atmosphere.

2.1.2 Global Structure of the Ionosphere. Much of the large-scale features of the ionosphere occur when the z -component of the IMF is directed southward (Schunk and Nagy 2000:393). Figure 2 shows the relationship of features such as polar holes

(dashed line in midnight sector poleward of 70 degrees Λ), ionization troughs (light gray shading on the nightside), and the auroral oval, (dark shaded circle) plotted against magnetic local time (MLT) and invariant latitude (Λ). The ionospheric current systems, the field-aligned currents, and particle precipitation interact to drive much of the dynamics that creates and sustains these features.

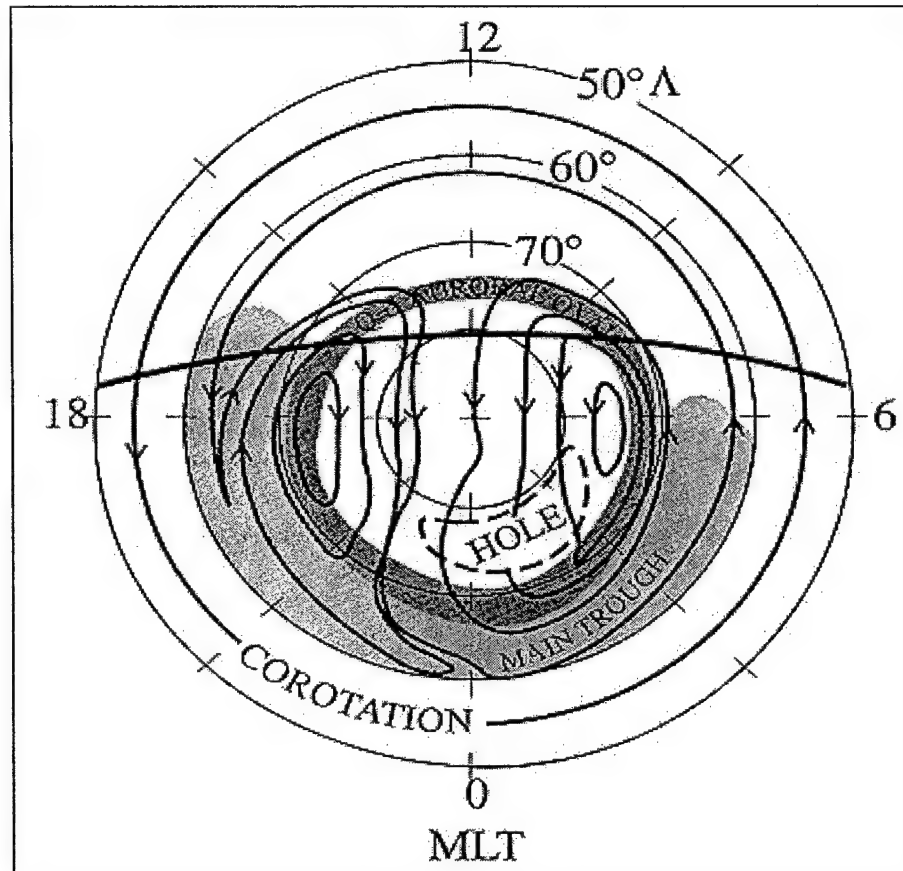


Figure 2: Structure of the high-latitude ionosphere (Schunk and Nagy, 2000)

Most of the structure has been characterized for the D, E, F₁, and F₂ layers. Structure can also be discerned in the topside, although sometimes not as readily or using the same criteria. Figure 3 shows the transition from O⁺ dominance to H⁺ dominance

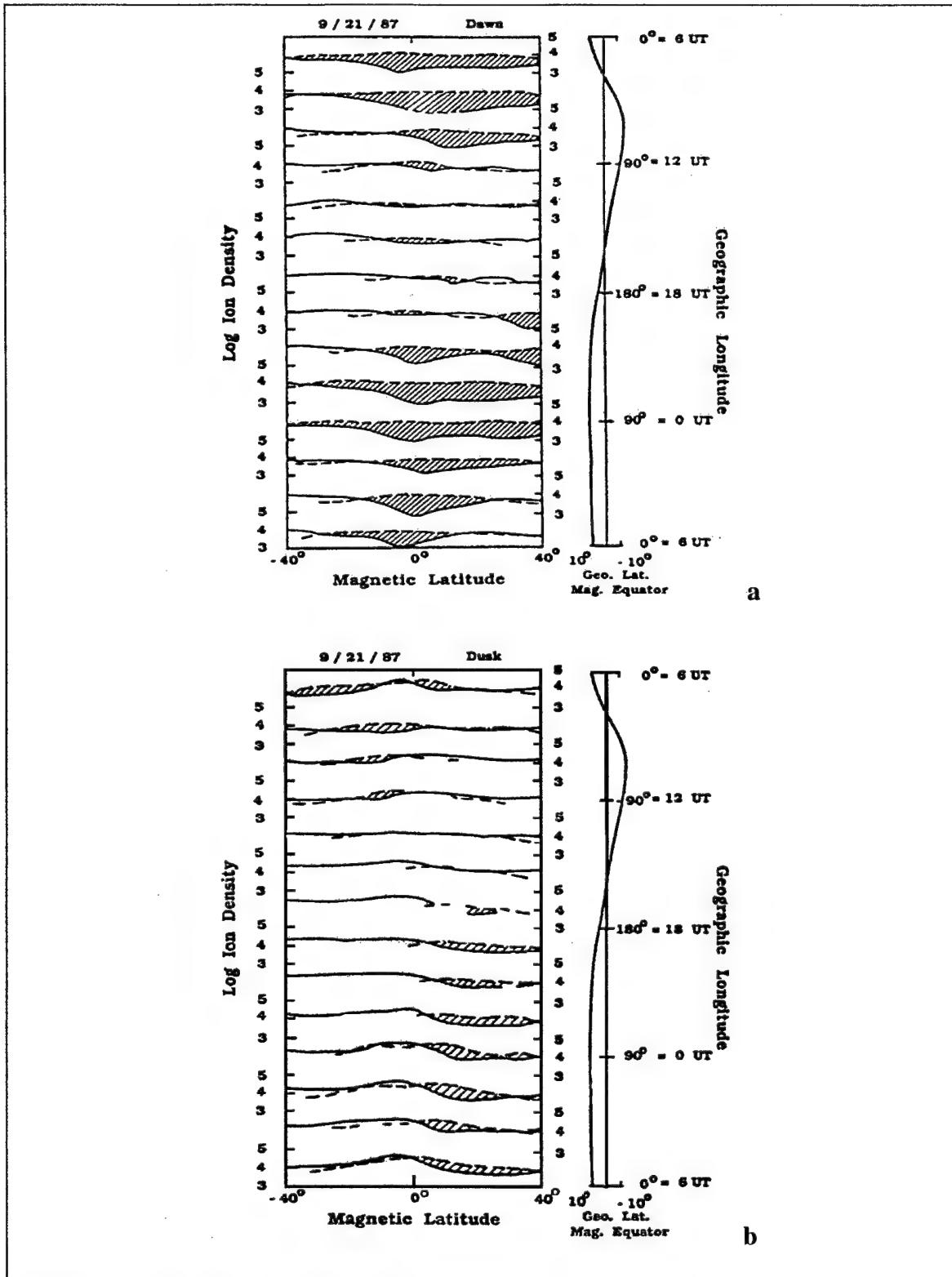


Figure 3: Typical density structure of the ionosphere at (a) dawn and at (b) dusk during solar minimum. (Greenspan *et al.*, 1994)

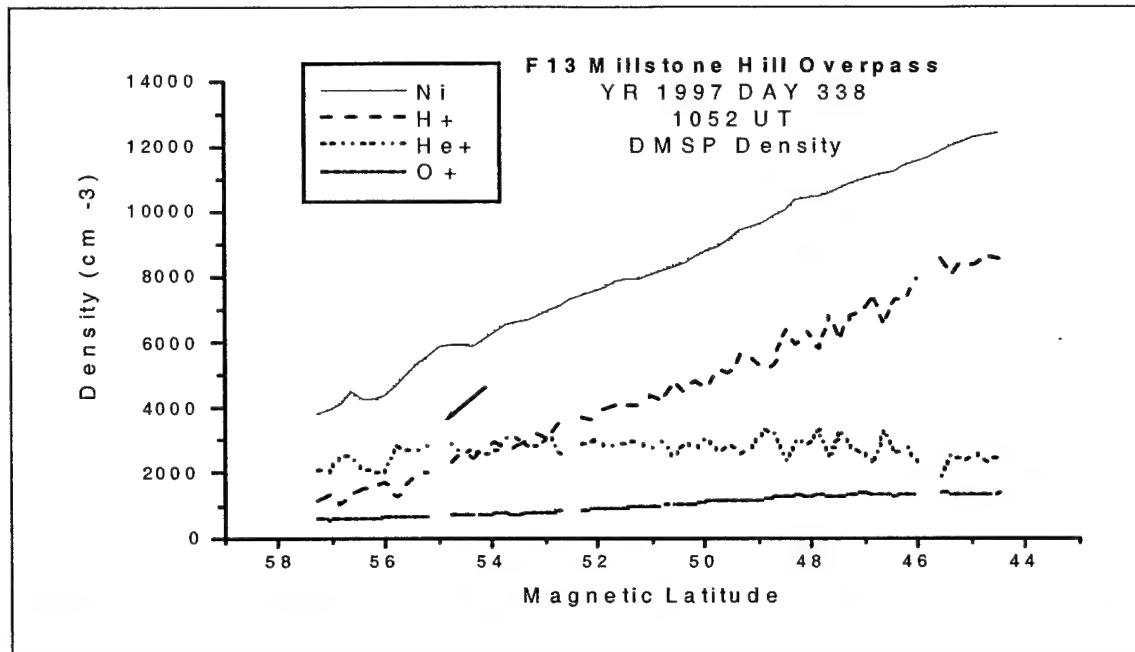


Figure 4: DMSP density plot showing He⁺-predominance from 54° to 58° Λ.

frequently occurs below the DMSP altitude of 840 km. According to Greenspan *et al.* (1994), the topside ionosphere displays considerable variability between dawn and dusk sectors that vary depending on longitude and magnetic activity, but has marked day-to-day consistency. Also, the $E \times B$ drift and neutral wind flow allows He⁺ to become dominant in some regions of the topside, mid-latitude ionosphere. Figure 4 illustrates just such an occurrence found during our research.

The mid-latitude ionosphere can vary on several time scales -- daily, seasonal, and solar cycle. The diurnal variation below the F₂ peak is ascribed to the decrease in the solar zenith angle during the day that increases the ionization rate resulting in a higher plasma density around noon. On the topside, this maximum is later in the afternoon, due in part to diffusion, flow between the hemispheres, and effects of the neutral wind. The seasonal trend has the maximum during the winter at F₂ and below with less marked variation in the topside. The ratio O:N₂ increases in the winter due to the neutral

circulation that results in increased O^+ densities. The reduction of N_2 available for equation (3) in Section 2.1.5 contributes to the increase in the total amount of O^+ . This increase is due to a decrease in the O^+ loss rate and counterbalances the loss of ionization due to increased solar zenith angle. The net effect is higher densities in the winter (Schunk and Nagy, 2000). The solar cycle also influences the photoionization rate. During solar minimum, EUV flux is lower and so photoionization is lower, resulting in lower densities than during solar maximum.

2.1.3 Ionospheric Electrodynamics. Since the ionosphere is a weakly ionized plasma, electric and magnetic fields play major roles in the transport of its charged constituents. The variations in these fields drive much of the dynamics of the ionosphere. In the topside, where neutral species become very rarified (although still far outnumbering the charged particles), the charged particles have fewer neutral particles to collide with, so are unobstructed in their response to the electric and magnetic fields and flow freely along the field lines. This unimpeded flow of charged particles along the magnetic field lines yields high field aligned conductivity - σ_0 . High σ_0 results in several interesting consequences. First, this effect essentially short-circuits the ionosphere and allows no steady electric fields parallel to \mathbf{B} . Secondly, since the currents can flow freely along \mathbf{B} , magnetic field lines maintain an electric-equipotential. Third, \mathbf{E}_\perp is almost independent of height in the ionosphere, so electric fields in the low levels of the ionosphere permeate into the magnetosphere, relating the $\mathbf{E} \times \mathbf{B}$ drift between all levels of the ionosphere (Rishbeth, 1988).

The effects of the large σ_0 link the ionosphere to the magnetosphere. This linking is especially important in the high latitude regions where the magnetic field lines are open

into the magnetosphere. Changes in the magnetosphere driven by solar wind variations and other phenomena cause related changes in the ionosphere. The electric fields get mapped into the ionosphere, causing changes in the plasma flow. The connection also allows ionospheric plasma (both light and heavy) to escape into the magnetosphere, as well as allowing the higher-energy magnetospheric particles entry into the ionosphere.

2.1.4 The Subauroral Ion Drift. Subauroral ion drifts (SAID) are latitudinally narrow regions of rapid westward ion drift located in the evening sector and centered on the equatorward edge of the diffuse aurora (Anderson *et al.*, 1991). Figure 5 shows the signature of a SAID event from one pass of the Dynamics Explorer 2 satellite. A SAID can be loosely defined as a narrow band of westward plasma flow with a horizontal velocity exceeding 1000 m/s and generally located equatorward of the auroral zone at lower altitudes (around the F₂ peak). The velocity profile is sharply peaked and could be a result of increased velocity and associated Joule heating of the ionosphere causing field-aligned plasma flows. The heating in turn can be attributed to enhanced electric fields caused by geomagnetic sub-storms that increase the thermal energy of the ions collisionally by driving them through the neutrals. The field-induced motion will also result in a local depletion in the total ion concentration. This depletion will enhance the mid-latitude trough and is another characteristic of a SAID event at F-region heights. This heating of the ions can be readily transferred to the electrons, so a local enhancement in T_e might reasonable be expected. At DMSP altitudes, much of these effects can be mitigated or even unseen (Anderson *et al.*, 1991).

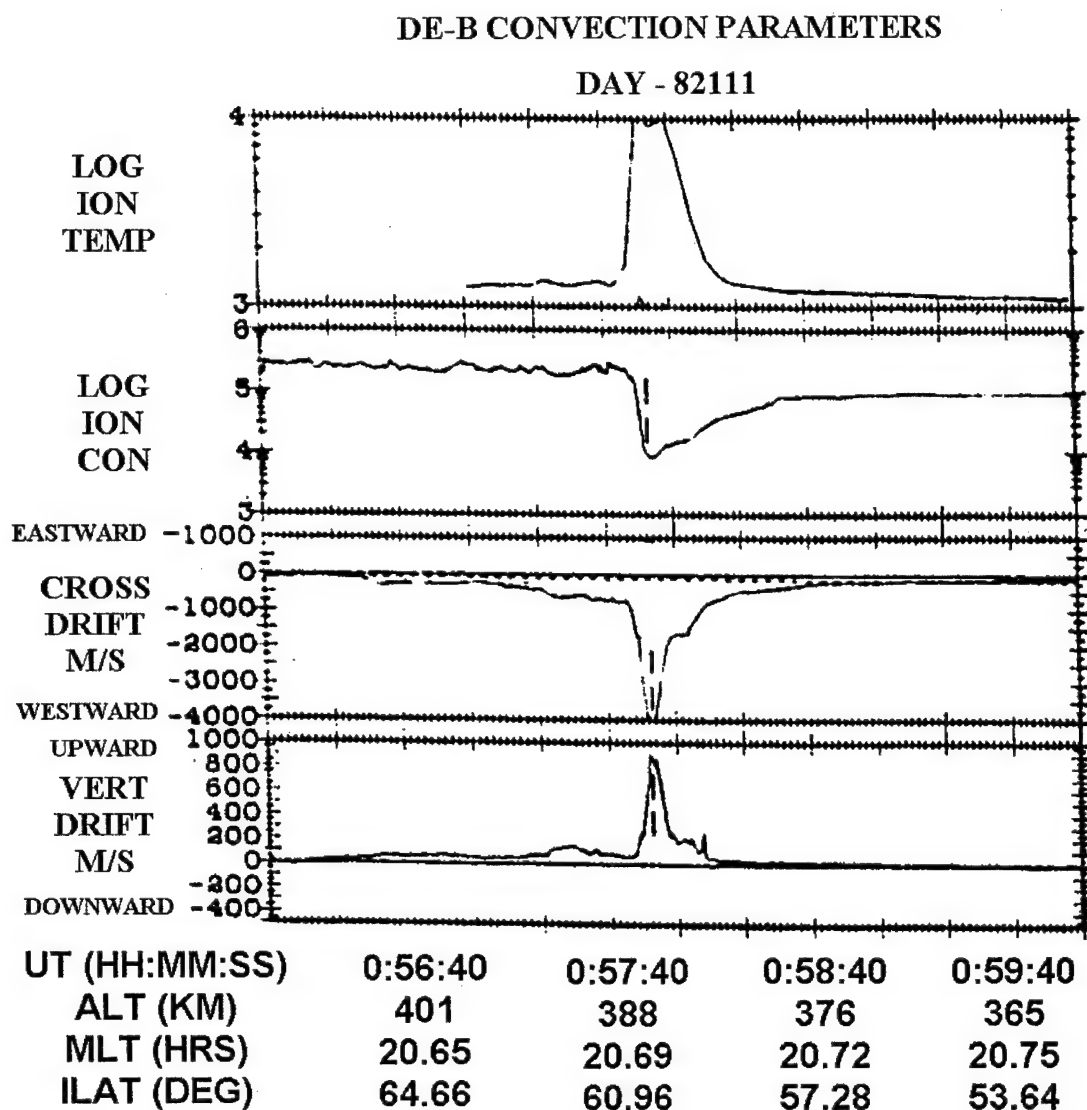


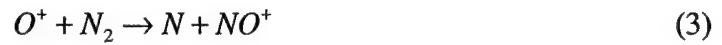
Figure 5: Signature of SAID event from the Dynamics Explorer 2 satellite showing sudden increase in velocity, corresponding trough in ion densities, and peak in ion temperatures. (From Anderson *et al.*, 1991)

SAID has been shown to be sub-storm related. It has been observed as soon as 30 minutes but never later than three hours after the sudden onset of a geomagnetic storm (Anderson *et al.*, 1991).

2.1.5 The Mid-Latitude Trough. The Mid-latitude Trough (MT) can be characterized as a decrease in N_e ; however most researchers agree the MT is primarily

attributed to a depletion of the O^+ concentration. This results from a combination of chemical and transport processes. The relative importance of chemistry versus transport is driven by several factors: (1) Rate of photo-ionization driven by time of day and season, (2) Strength of electric fields mapped from the magnetosphere, and (3) Location in polar convective scheme (Schunk, *et al.*, 1976).

The chemistry that depletes the ionosphere of O^+ is driven by the following reactions:



Equation (3) controls the rate of reaction in the topside ionosphere below the plasmopause when the concentration of N_2 becomes low and the light ions start to dominate. Equation (4) controls the reaction rate for O^+ equilibrium during hours of darkness when there is a lack of photoelectrons to enable this process and low in the ionosphere when the electron concentration is low.

Transport of O^+ from the topside, which contributes to MT formation, can occur for several reasons. First, plasma can convect across the polar cap and into the nightside, where photoionization ceases and ion density subsequently decreases. This is driven by $E_{\perp} \times B$ drifts in the auroral zone. Secondly, the H^+ escapes via a process call the polar wind. This occurs as H^+ travels along geomagnetic field lines and escape the ionosphere. The reduction in H^+ limits the charge exchange reaction (equation (1)) and inhibits the creation of O^+ while still losing O^+ in the reverse reaction. The third transport process is

the thermospheric wind. This acts to slow the rate of decay by raising the F₂ layer, but also acts to increase the amount of excited N₂ through the trough, which aids the decay of O⁺ through equation (3) (Schunk, *et al.*, 1976). Figure 6 illustrates a typical MT.

Moffett and Quegan (1982) claim the community has agreed on the following characteristics of the MT:

1. Primarily a night-side phenomenon, extending from the dusk to the dawn-side.
Also observed in the noon sector.
2. Regularly observed during winter and equinox. In summer, it is only observed near local midnight.
3. Poleward edge is relatively steep (compared to equatorward edge) and lies just equatorward of the diffuse auroral precipitation boundary.
4. Latitude of the trough decreases at night.
5. Trough moves to lower latitudes during periods of increased magnetic activity.
6. The solar cycle does not influence the occurrence and structure of the trough.

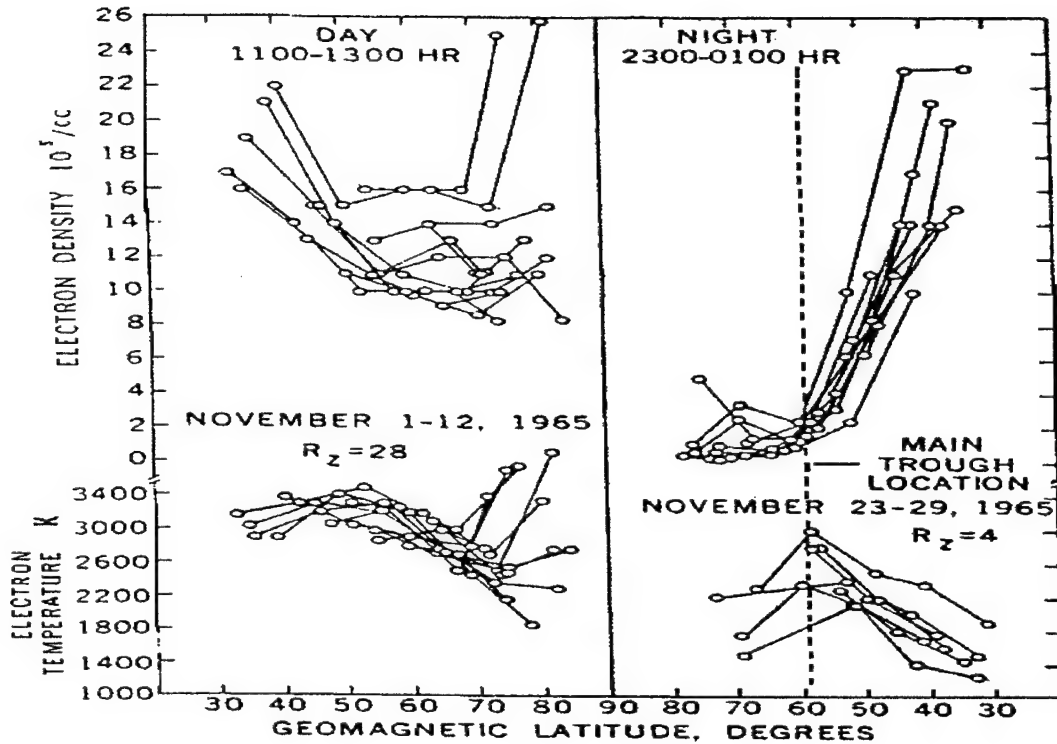


Figure 6: Mid-latitude trough (From Miller, 1970)

Other potential characteristics of the MT do not have a consensus from the community. One is the ion drift velocity. In pre-midnight troughs, large westward velocities as well as some eastward drift have been observed. Post-midnight, the velocities generally match the rotation of the earth. Also, an increase in the ion temperature can be expected. A decrease of the available mass (O^+) to absorb the flux of energy into a given volume of gas would result in a local increase in the temperature of the remaining constituents. An increase of the ion temperature would be reflected in the electron temperature.

2.1.6 The Light Ion Trough. The Light Ion Trough (LIT) is characterized by a decrease in the densities of the light ions (H^+ and He^+), with little or no change in the total electron density as seen in Figure 7. Clear signs of a LIT can be found during the

nighttime in all seasons and in the daytime sectors during the winter. It is seen in mid-latitude regions of the ionosphere, beginning near 60° magnetic latitude with its poleward edge at the diffuse auroral boundary. The LIT is more pronounced during nighttime and the dayside winter, while it is less well defined during summer and equinox daytime. The minimum will deepen and move equatorward during periods of geomagnetic activity, due mainly to the increase of plasmaspheric convection (Taylor, 1972).

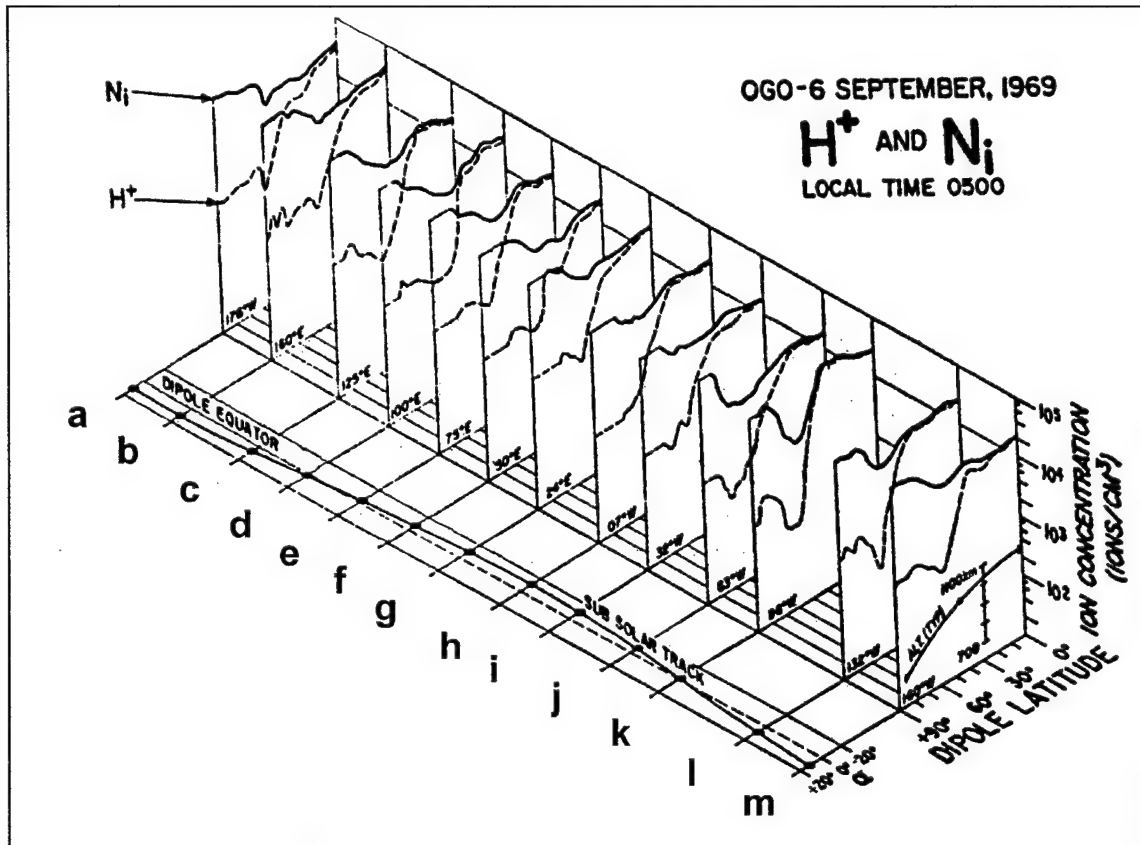


Figure 7: LIT demonstrated by isometric projection of H^+ and N_i profiles observed near 0500 LT between 22-27 September, 1969. Pairs of profiles are shown for the longitudes corresponding to each pass (Taylor, 1972). The orbits are from September 1969 at date/time of the orbits (a) 23/1613-1706, (b) 23/1753-1846, (c) 22/2020-2112, (d) 22/2200-2252, (e) 22/2339-0031, (f) 23/0115-0209, (g) 23/0256-0347, (h) 25/0442-0553, (i) 25/0621-0712, (j) 27/0807-0900, (k) 27/0847-1053, (l) 25/1259-1352, and (m) 22/1318-1411.

2.1.7 The Aurora. The aurora is the manifestation of high-energy particles from the solar wind and magnetosphere being injected into the high latitude regions of the ionosphere via the dayside cusp and the magneto-tail on the nightside. The aurora generally forms an oval around the geomagnetic north and south poles. It extends latitudinally approximately 23 degrees on the nightside and 15 degrees on the dayside, fixed on a latitude-MLT grid, but is heavily dependent on geomagnetic activity (Bruzek and Durrant, 1977:190).

While the aurora provides a “beautiful colour pattern,” it has consequences in the structure and dynamics of the high-latitude ionosphere. The increased high-energy particle precipitation creates additional ionization, increasing local densities and transferring some of that energy to the ambient plasma. Also, the atoms and ions can become collisionally excited and -- along with the optical wavelengths normally associated with the aurora -- emit short-wavelength radiation (X-ray and EUV) as the species relax back to a lower energy state. The emitted radiation can produce additional photoionization. Because the auroral oval is relatively confined, the spatial scale of these phenomena is short, particularly in latitudinal extent. Ground-based measurement techniques may have trouble resolving this scale, especially high in the topside.

2.2 Incoherent Scatter Radar

Incoherent Scatter Radar (ISR) is based on properties of electron scattering referred to as Thompson Scattering, after J. J. Thompson, the discoverer of the electron. Several parameters are directly measurable by ISR to include electron density (N_e), electron temperature (T_e), ion temperature (T_i), mass of species “i” (m_i), plasma velocity,

and the relative motion of the ions and electrons. From these measurements, conductivities and the neutral wind are derivable (Hargreaves, 1992).

Since the relatively high-density plasma at the base of the ionosphere will reflect the lower frequencies of the radio spectrum, the radar must have a sufficiently short wavelength to penetrate into the topside. To a second order approximation, the radar beam will propagate through the ionosphere without any reflection off the plasma (Evans, 1975). However, the electrons in the ionosphere will reflect a small portion of the energy from the incident radar beam. High-power radars with large collectors are required to receive this weak return signal. Since the electrons are in motion, each electron will scatter the signal with many different phase shifts (incoherently), depending on the thermal motion of each individual electron. The amount of power received at the radar will then be sum of the individual reflections and be related to the number of electrons available to scatter the radar beam. On average, the scattering cross section per unit volume will be the radar cross section of the electron -- σ_e -- multiplied by the number density, N (Evans, 1969). The radar cross section of the electron is given as

$$\sigma_e = 4\pi(r_e \sin \psi)^2 \approx 10^{-28} \sin^2 \psi \text{ m}^2 \quad (5)$$

where r_e is the classical electron radius:

$$r_e = \frac{e^2}{\epsilon_0 m_e c^2} = 2.82 \times 10^{-13} \text{ m} \quad (6)$$

and ψ is the angle between the incident electric field and a line to the receiver (polarization angle). Thus the area under the curve of returned power in the frequency domain in Figure 8 provides a straightforward indication of the number density.

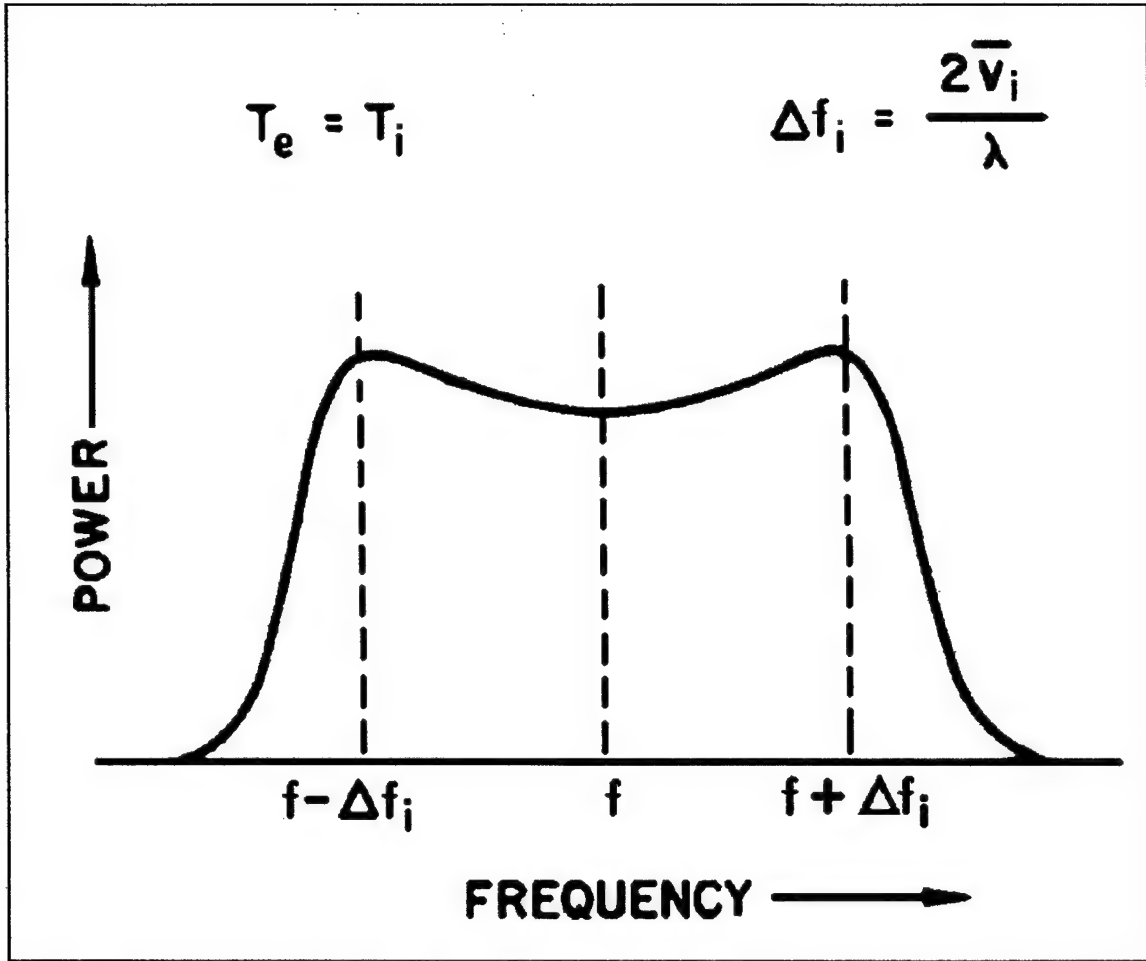


Figure 8: The power spectrum of radio waves incoherently backscattered by the ionosphere assuming $T_e = T_i$. Δf_i is the Doppler shift for ions approaching the radar at their mean thermal velocity \bar{v}_i . λ is the radar wavelength. (Evans, 1975)

The scattering by the electrons is complicated by the fact that the ions feel a Coulomb attraction to the electrons, thus the return is not totally incoherent. The width of the returned spectrum determines the temperature of the electrons. The thermal motion of the electrons would induce a Doppler shift of the transmitted frequency, giving the return a Gaussian shape with a center to half-power width of $0.71 \Delta f_e$, where

$$\Delta f_e = \frac{1}{\lambda} \left(\frac{8k_B T_e}{m_e} \right)^{\frac{1}{2}} \text{ Hz} \quad (7)$$

where λ is the radar wavelength in meters and k_B is Boltzmann's constant (Evans, 1965).

Since the electron motion is influenced by the much heavier ions, this returned spectrum is much narrower. The shape of the return in Figure 9 characterizes the ratio of the electron temperature to the ion temperature. As the electron temperature increases relative to the ion temperature, the thermal ion motion interferes less and less with the returned signal from the electrons, causing the peak to narrow and move toward larger Δf .

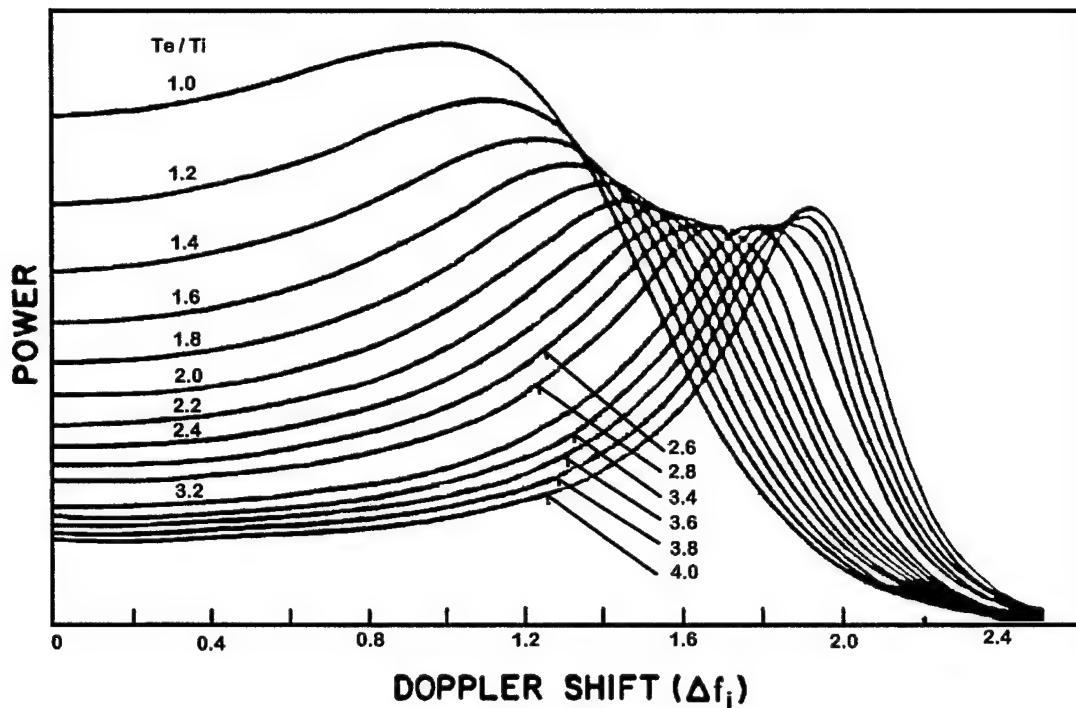


Figure 9: The power spectrum of the incoherent scatter echoes when T_e exceeds T_i by the ratio given. (Evans, 1975)

Today's ISRs have relatively long wavelengths; for example, Arecibo Radio Observatory's primary wavelength is 70 cm (430 MHz). This is much greater than the Debye length of the plasma, which is on the order of 1 cm in the ionosphere. The Debye length-- D --describes the distance away from a charged particle where the plasma effectively shields that particle from the influence of external fields. It is given by

$$D = \left(\frac{\epsilon_0 k_B T_e}{4\pi N e^2} \right)^{\frac{1}{2}} \text{ meters} \quad (8)$$

This results in the return measuring the density fluctuations in the plasma versus the individual electrons themselves (Evans, 1969).

The Millstone Hill Observatory ISR is operated by the Massachusetts Institute of Technology as part of the Haystack Observatory Atmospheric Sciences group with major funding from the National Science Foundation (NSF). The facility consists of two 2.5 MW, 440-MHz transmitters, a fully steerable 46-meter antenna, a zenith-directed 68-meter fixed antenna, and dedicated computer and database facilities. Its location at 53.2°N magnetic (42.6°N geographic) latitude places it within range of the aurora and the sub-auroral region of the ionosphere much of the time, as well as being ideally located to study mid-latitude phenomena (Erickson, 1995).

SRI International, Inc. is an independent corporation research that works closely with Stanford University, located in Menlo Park, CA. SRI operates the Sondrestrom radar under contract to the NSF and in cooperation with Denmark's Meteorology Institute. The radar is located near Kangerlussuaq, Greenland, and was moved there in 1983 from Chatanika Alaska, where it had operated since 1971. It is a 32-meter, fully steerable, parabolic dish, with accompanying low-noise amplifier, receivers, and digital signal processing computers, operated by an on-site staff and managed by the staff and scientists in Menlo Park. The site in Greenland places the radar in position to measure the auroral and polar cap ionosphere much of the time. Also, the earth's dipole field intersects the surface perpendicularly in this region, so Sondrestrom is well suited to take measurements parallel to the **B** field.

Table 1: ISR Radar Locations

ISR Site	Geographic Latitude	Geographic Longitude	Geomagnetic Latitude
Arecibo	18.3°N	66.7°W	30.0°N
Jicamarca	11.9°S	76.9°W	1.1°N
Millstone Hill	42.6°N	71.5°W	53.2°N
Sondrestrom	67.0°N	51.0°W	71.0°N
Sondrestrom Up B (@ 850 km)	65.9°N	48.8°W	

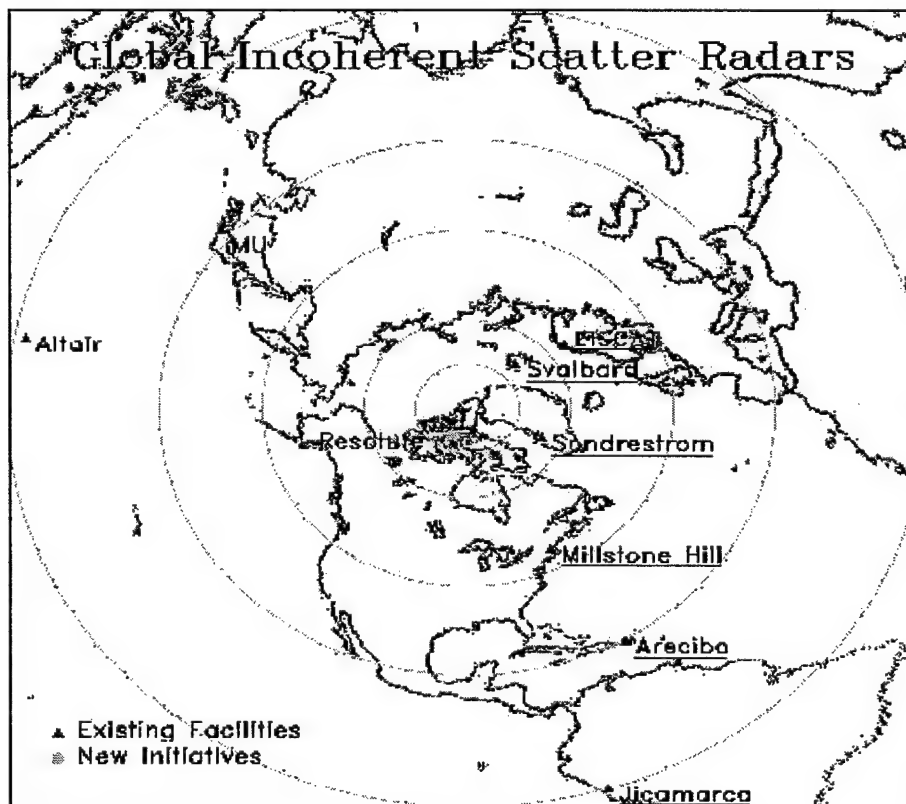


Figure 10: Map of ISR sites worldwide (SRI, Inc., 2000)

2.3 POLITE Campaigns

The Plasmaspheric Observation of Light Ions in the Topside and Exosphere (POLITE) Campaigns are coordinated efforts between the incoherent scatter radars in the chain (Erickson, 1997). These campaigns are designed to pursue science on topics that include light ion spatial variations, storm-time effects on ions and neutrals, charge exchange physics in the topside, H concentration variations, and improving the MSIS-modeled H concentrations. The radars are configured to measure the extremely weak returns from the topside of the ionosphere. The lower electron concentrations in this

Table 2: POLITE Campaign Dates

Campaign	Date	Julian Date
POLITE 1	13 – 14 Feb 1996	96044 – 96045
POLITE 2	11 – 14 November 1996	96316 – 96319
POLITE 3	3 – 6 June 1997	97154 – 97157
POLITE 4	2 – 4 December 1997	97336 – 97338
POLITE 5	26 – 28 May 1998	98146 – 98148
POLITE 6	22 – 25 November 1998	98326 – 98329
POLITE 7	8 – 9 October 1999	99281 – 99282
POLITE 8	9 – 10 December 1999	99343 – 99344
POLITE 9	6 – 7 January 2000	00006 – 00007
POLITE 10	1 – 3 July 2000	00183 – 00185

region result in a lower signal strength. This requires a longer integration of the radar return to have sufficient signal to derive the parameters. As a result of the longer integration time, problems develop from larger amount of noise in the return, thus increasing the uncertainty of the measurements.

The POLITE campaigns were ideal for this characterization effort since the radars were set to a mode that optimizes the returns from the topside. Conventional modes of the ISR generally result in returns that are unreliable above 700 km and require extensive extrapolation to derive values at DMSP altitude.

2.4 Defense Meteorological Satellite Program (DMSP)

The DMSP satellites are low-orbit (840 – 860 km), high inclination (98 degrees) polar satellites that complete one orbit every 101 minutes. This orbit allows the satellites to cover approximately the same local time over the earth's surface on each node (ascending or descending). The time of the node indicates the local time at the equator when the satellite is directly overhead. The satellites are launched into a nominal orbit, but conditions during the launch and placing the satellites in orbit determines the actual time of the overpass. Also, since the earth is not a perfect sphere and does not follow a perfectly elliptical path around the sun, variations occur in the orbits. Table 3 lists the nominal and actual time of each orbit. Figure 11 shows a schematic of the satellites' nominal locations relative to magnetic local time.

Table 3: Local Times of DMSP Overpass

Satellite	Nominal LT of Overpass	Actual LT of Overpass
F11	1730 / 0530	1919 / 0719
F12	2030 / 0830	2049 / 0849
F13	1730 / 0530	1711 / 0511
F14	2030 / 0830	2035 / 0835
F15	2110 / 0910	2110 / 0910

The first entry is the ascending node. (Rich, 2000)

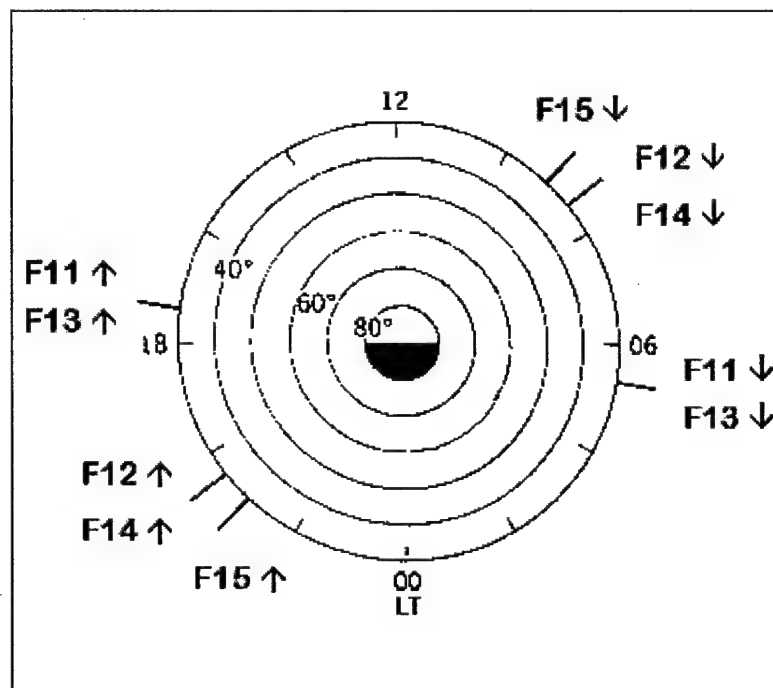


Figure 11: Location of Nominal DMSP Ascending/Descending Nodes

The DMSP's primary mission is to monitor terrestrial weather through their Optical Line Scan (OLS) sensors that image the earth's atmosphere in both the visible and infrared bands. Its secondary mission is to provide quantitative *in-situ* measurement

of the thermal plasma environment (low energy electrons and ions) in which it orbits. To accomplish this, it is equipped with the Topside Ionospheric Plasma Monitor (Special Sensor for thermal Ions, Electrons, and their Spatial variations or SSIES). The SSIES consists of a suite of instruments designed to measure the ion and electron density, temperature, density fluctuations, and velocity. Figure 12 shows the location of the SSIES instruments on the DMSP spacecraft. The Electron Sensor (EP) is a Langmuir probe that measures thermal electrons in the temperature range of 500 - 8000 K and in the density range from 10^2 to 10^6 electrons/cm³. It makes one complete measurement cycle each eight seconds consisting of four seconds of increasing bias voltages and four seconds of decreasing voltages. Each four seconds of data yield one measurement of electron temperature and density (Rich, 1994). Measurement of the thermal electrons from the ambient plasma is complicated by the presence of photoelectrons generated by the spacecraft and the sensor itself. Rich (private communication, 9 June 2000) says, "To get the density from the EP sensor it is necessary to know the electrostatic potential between the sensor and the plasma is zero. If there is an error of +/- 0.2 Volts (which is quite possible), then the electron density derived from the EP data is in error by ± 50 percent or slightly more." For this reason, the EP values were not used in this study.

The ion sensors are housed in one unit and are situated so the sensors point in the direction of spacecraft travel. The design of each of the ion sensors is based on a Faraday cup, where the ions flow through an aperture that isolates the plasma from the collector surface. The measurements are taken as voltages induced on the collector (Rich, 1994). This group consists of the Total Ion Density Sensor (Scintillation Meter), the Ion Retarding Potential Analyzer, and the Duct Meter. These sensors are held at the ambient

plasma potential through the Sensor Potential (SENPOT) which measures the potential of the plasma relative to the spacecraft and adjusts the ion sensors so they measure a flow of ions relatively undisturbed by electric fields generated by potential differences between spacecraft and the ambient plasma.

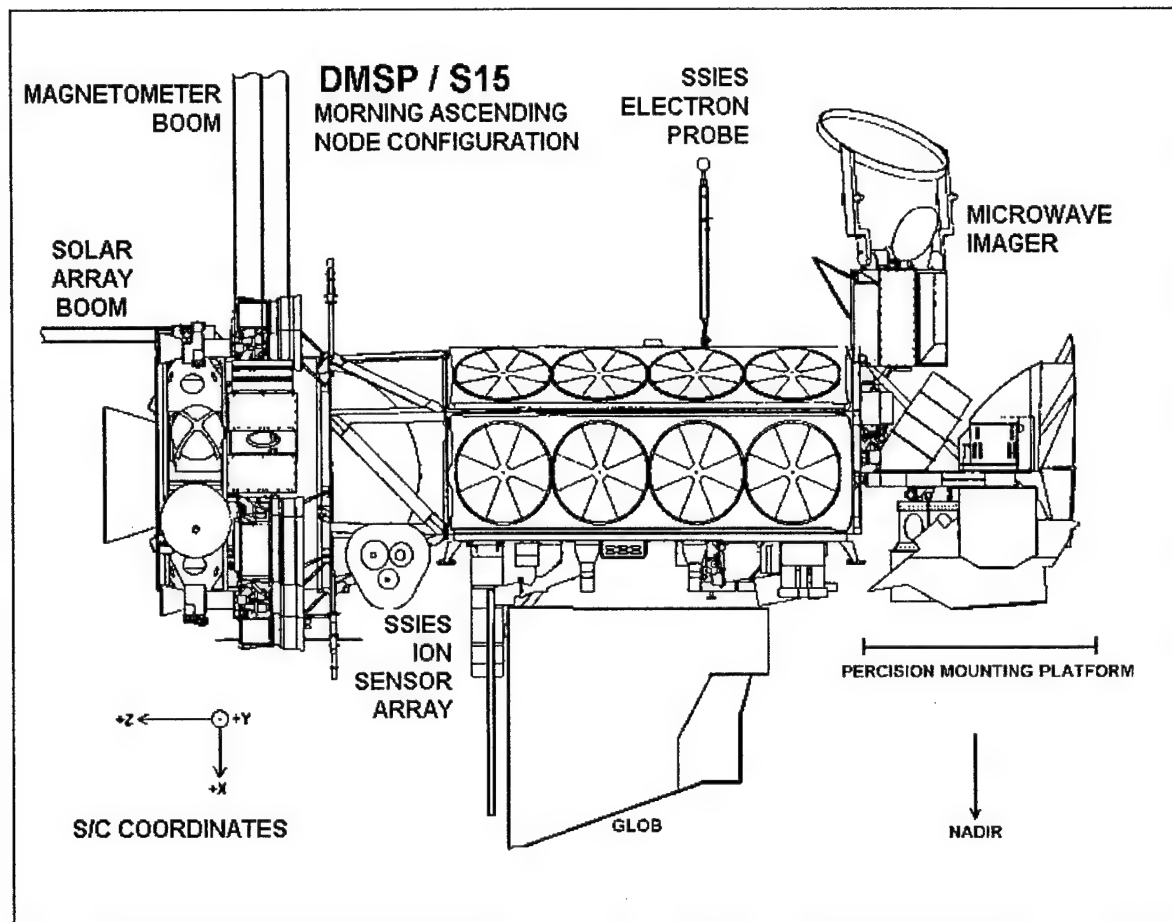


Figure 12: SSIES/SSIES2 sensors mounted on the DMSP spacecraft. (Rich, 1994)

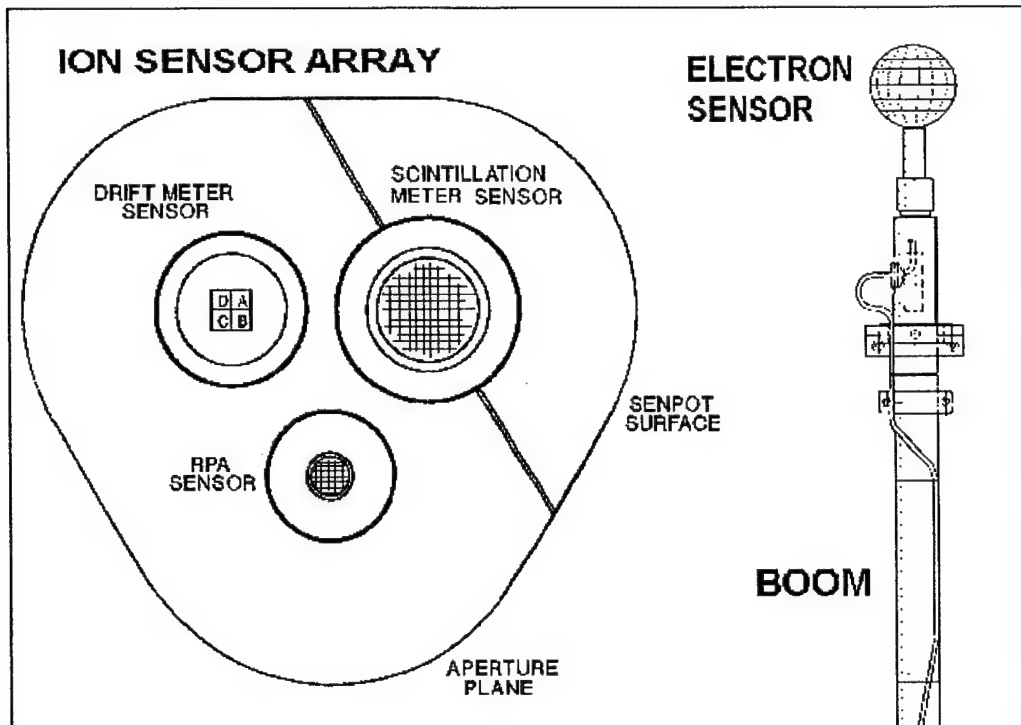


Figure 13: External view of the SSIES2 ion sensors with the aperture array and the electron sensor on the end of its boom. (Rich, 1994)

The Total Ion Trap (SM) is the simplest of the ion density instruments of the SSIES series. It consists of a very wide aperture with a minimum of grids between the aperture and collector plate (Rich, 1994). Its primary use is to measure density variations, however it also measures the total ion density. It takes 24 measurements per second and characterizes them into one of five ranges. The SM has an operational range of 10^2 - 10^6 ions/cm³. Values above this range will cause the sensor to saturate. The SM operates on a 16 second cycle in a quiet ionosphere at which point a flag is set to indicate which of the five ranges the measurement is taken. A new range is set if another 16 seconds elapse or the measurements exceed that range. If the latter occurs within the first second of the cycle, density data output ceases until the next cycle starts; if it happens after one second, density data will not be output until the next odd cycle-count.

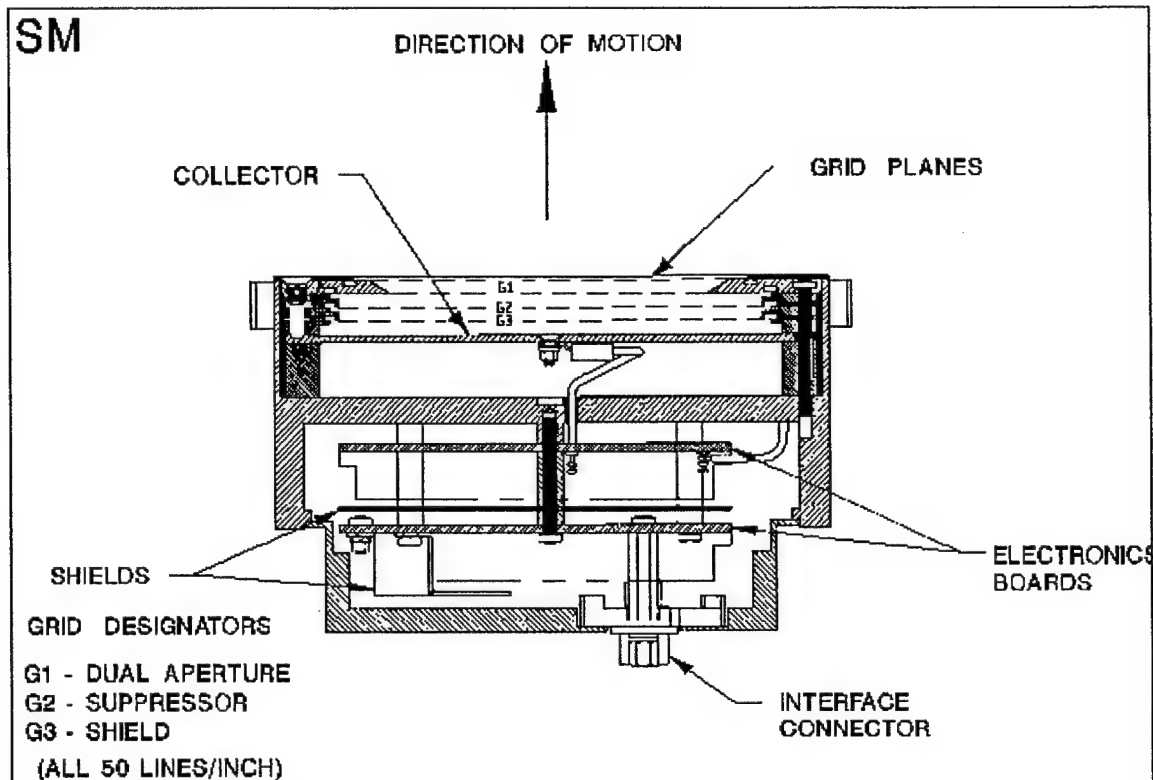


Figure 14: Total Ion Density Sensor (Scintillation Meter). (Rich, 1994)

The Ion Retarding Potential Analyzer (RPA) operates by holding the aperture as close to the plasma potential as possible, creating field lines in front of the aperture that are parallel to the surface of the instrument. This allows the ions to enter the aperture without being deflected, and without forcing additional ions into the instrument. This results in the RPA on the DMSP being able to measure lower densities than similar instruments on other spacecraft. The processing algorithms assume the ions follow a Maxwellian distribution, which allows determination of ion density, as well as ion composition, ion temperature, and average species velocity (Rich, 1994).

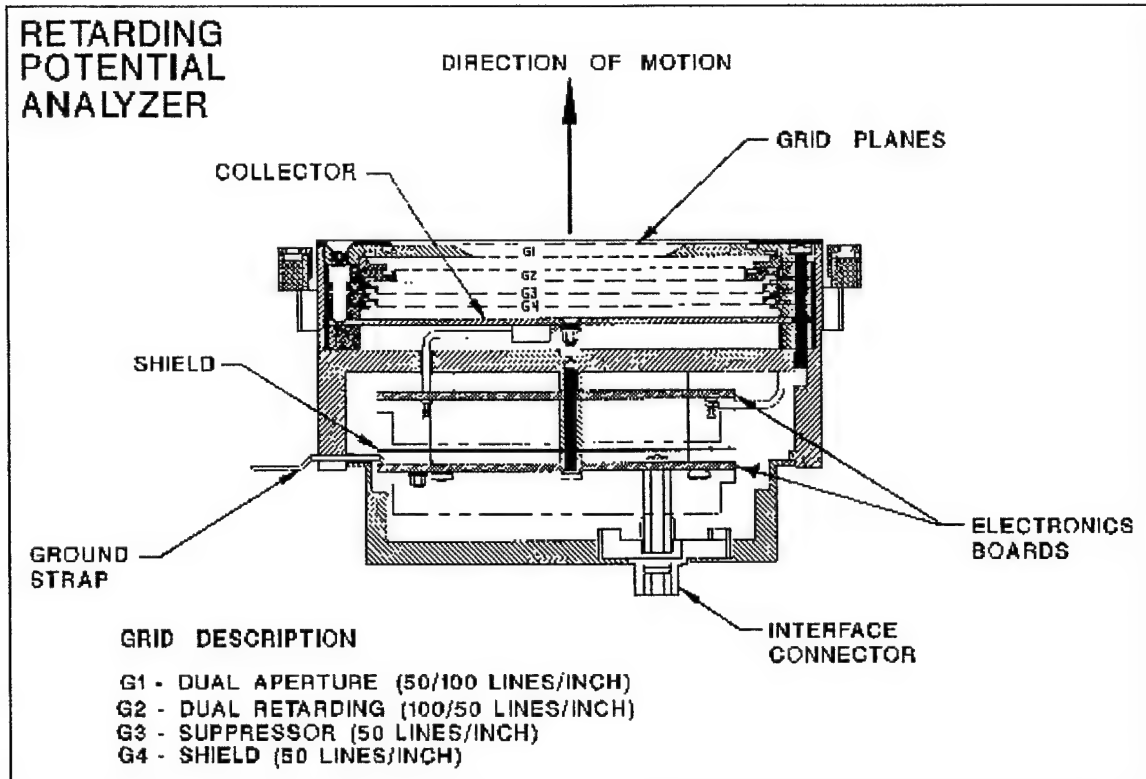


Figure 15: Retarding Potential Analyzer (Rich, 1994)

Another sensor system on the DMSP that measures the spacecraft environment is the Precipitating Energetic Particle Spectrometer, called the SSJ4. The sensor measures high-energy particles (30 eV to 30 keV) that cross the satellite's path on a nearly vertical trajectory (Rich, 1994). This system is used for detecting precipitating particles and can be used to determine whether the satellite is in the auroral zone. Gussenhaven, *et al.* (1982) used these measurements to calculate regression statistics that determine The Air Force Research Laboratory Auroral Boundary Index (Equivalent Midnight Equatorward Boundary Index -- EQB). Appendix D outlines the process.

The current family of DMSP satellites is unable to downlink the SSIES measurements of the plasma in near real time. Future spacecraft will need to have this ability for the data to be the most useful to modelers. As the DMSP program moves

under NOAA's (National Oceanographic and Atmospheric Administration) NPOES (National Polar Orbiting Environmental Satellite) program, real-time telemetry will be crucial to using plasma measurements in a global specification and forecast model.

2.5 GAIM Proposal

The Global Assimilation of Ionospheric Measurements (GAIM) proposal is a Multi-University Research Initiative (MURI) spear-headed by Utah State University's Center for Atmospheric and Space Sciences with Dr. Robert Schunk as Principal Investigator. The University of Texas at Dallas (UTD), the University of Colorado at Boulder (CU), and the University of Washington (UW) join Utah State in this MURI proposal.

The goal of the GAIM proposal is to generate a physics-based model of the space environment that will assimilate both space- and ground-based measurements of the ionosphere in near real-time. The proposed method is to use Kalman filtering. This technique incorporates an initial estimate of the error in the various measurements and models used. The procedure then applies a dynamic model to advance one time step, incorporating the expected errors. Because of the size and complexities of determining the model error, the sensor error is analyzed only for its dominant structures. This error approximation is applied to a full, non-linear forecast at each time step (Schunk and Sojka, 1999).

GAIM must have a reasonable estimate for the error in the data being assimilated. Prior to incorporation into the model, the data must be analyzed to determine the typical variability of the measurements and the random noise associated with the measurements

received from the instruments. It should be noted that this instrumental error could have significant variability depending on factors such as the season, latitude, location in the solar cycle, and storm activity (Sojka, private communication, 15 November 2000).

Once a good estimate of the error is found, this is incorporated into the automated assimilation step of the Kalman filter. This estimate is used to ensure the data the model receives are reasonable (within expected range and variations) and to account for the expected error before the model receives it. Once this is accomplished, data can be ingested and assimilated by the GAIM routine with a minimal of human intervention.

III. Methodology

3.1 Prior Research

Sultan and Rich (2000) compared DMSP-measured plasma ion density during solar maximum against data from Millstone Hill. This dataset was mined from the Millstone Hill archives and consisted of short pulse-length (640 μsec) returns with a vertical resolution of 48 km. These generally only extended to 700 – 750 km and were extrapolated to DMSP altitude. Two sequential returns were required within ± 30 minutes of the overpass time for the conjunction to be used. All the returns within the ± 30 minutes were used to arrive at an average value for the radar, provided the scatter of the radar returns were not too great. Cases with too much scatter were discarded.

The DMSP density data were averaged over a five-degree circle around the site. Instances where the gradient in the SSIES density was too great were discarded. According to Sultan and Rich (2000), this happened most often during geomagnetic disturbances.

The result of this research was that the DMSP SSIES system measured the ionospheric plasma to within nine percent of the ISR-measured density. This was within the 10 percent error published for the SSIES system (Sultan and Rich, 2000). However, no attempt was made to characterize the error in either the DMSP or ISR data in the study.

Over the span of the DMSP lifetime, numerous researchers have studied the ionosphere using the SSIES data. Greenspan *et al.* (1994) used F8 DMSP measurements to classify the topside ionosphere during solar minimum. West and Heelis (1996) used

F10 ion composition data to characterize longitudinal variation in the topside equatorial ionosphere. The community accepts these data as representative of the ionosphere, but until the Sultan and Rich study, no formal comparison had been made to the ISRs to detail the differences.

3.2 Description of ISR data

ISR data were requested from all four of the Western Hemisphere ISRs—Arecibo, Jicamarca, Millstone Hill, and Sondrestrom. Data were available for the POLITE campaigns for Millstone Hill and Sondrestrom (see Table 2).

3.2.1 Millstone Hill. The Millstone Hill ISR data used were taken during the POLITE windows, however the data did not cover the entire period. The radar observations would normally start around sunrise on the first day of the campaign (12 – 16 UT) and conclude around sunset on the last day of the campaign. This precluded a number of possible DMSP overpasses and limited the number of cases for comparison. Only data from the zenith radar were used to avoid the necessity to correct for the displacement of the beam/satellite conjunction from overhead of the radar location. The returns were analyzed using a two-ion fit (H^+ and O^+) *versus* a three-ion fit (which includes He^+) due to an inordinate increase of required processing. The difference in the two methods should be practically indistinguishable (Erickson, private communication, 11 September, 2000).

Millstone Hill operated in three main modes of its zenith antenna. For part of the time, it operated at a pulse length of 410 μ sec, which is one of its normal operating modes (the other being 640 μ sec). This mode mapped the structure of the lower ionosphere, which helped determine the overall state of the ionosphere. It returned data

in bins separated vertically by 30 km. The short pulse length provided the finest resolution of Millstone Hill data available, however this did not allow returns from DMSP altitudes. This pulse length generally did not reach above 750 km.

Millstone Hill also used longer pulse lengths of 1000 μ sec and 2000 μ sec during the POLITE campaigns that generated vertical resolutions of 75 km and 150 km, respectively. This provided measurements to altitudes well over 1000 km. While the resolution was not ideal, the return was integrated over a larger vertical extent providing a vertically averaged value useful in this study. Table 4 describes Millstone Hill's data. Parameters with an asterisk (*) were used to compare the ISR to the SSIES density.

Table 4: Millstone Hill Data Description

Parameter	Description	Parameter	Description
UTH*	Time past 0000 UT on first day of campaign	SNP3	Signal to noise ratio
GDALT*	Altitude	POPL*	Log10 uncorrected electron density
AZM	Mean azimuth angle	DPOPL*	Error Log10 uncorrected electron density
ELM	Elevation Angle	NEL*	Log10 corrected electron density
GDLAT	Geodetic latitude of measurement	Ti*	Ion temperature
GLON	Geodetic longitude of measurement	DTi*	Error ion temperature
PL	Pulse length	Te*	Electron temperature
VO	Line of sight ion velocity	DTe*	Error electron temperature
DVO	Error line of sight velocity	PH+	Composition [H ⁺]/Ne
		DPH+	Error Composition

The corrected electron density (NEL) was derived from the following equation:

$$NEL = CS * POPL * (1 + \frac{T_e}{T_i}) \quad (9)$$

where NEL is the corrected electron density, POPL is the uncorrected electron density, T_e is electron temperature and T_i is ion temperature. CS is a system parameter that accounts for the radar wavelength and is taken to be a constant. This is similar to the corrected electron density equation given in the CEDAR Database Catalogue (1998)

$$N = \frac{(1 + \alpha^2 + T_e/T_i)(1 + \alpha^2)}{2} N_{uncorrected} \quad (10)$$

$$\alpha^2 = 7.654 \times 10^5 \frac{T_e}{\lambda^2 N}$$

where

N = true electron density (m^{-3})

T_e = electron temperature (K)

T_i = ion temperature (K) and

λ = radar wavelength (m).

In the case where $\alpha^2 \ll 1$, $CS \rightarrow 0.5$.

The Millstone Hill data did not contain an uncertainty in the corrected density value. Erickson (private communication, September 2000) indicated that standard error propagation could be used to determine an uncertainty value. Using a “worst case” approach as defined by Taylor (1982), the upper bound of the error is given as

$$\delta q = \left| \frac{\partial q}{\partial x} \right| \delta x + \left| \frac{\partial q}{\partial y} \right| \delta y + \left| \frac{\partial q}{\partial z} \right| \delta z \quad (11)$$

and assuming that all three measurements are independent, a differential of equation (9) was used, which resulted in

$$DNEl = CS * (DPOPL * (1 + \frac{Te}{Ti}) + POPL * \frac{DTe}{Ti} + POPL * \frac{Te}{Ti^2} * DTi) \quad (12)$$

This method was used to determine the uncertainty for all the Millstone Hill corrected densities when all parameters were available.

For the case studies, the following, lower bound error propagation equation from Taylor (1982) was used:

$$\delta q = \sqrt{\left(\frac{\partial q}{\partial x} \delta x\right)^2 + \left(\frac{\partial q}{\partial y} \delta y\right)^2 + \left(\frac{\partial q}{\partial z} \delta z\right)^2} \quad (13)$$

which resulted in

$$DNEl = CS * \sqrt{\left(DPOPL \left(1 + \frac{Te}{Ti}\right)\right)^2 + \left(POPL \frac{DTe}{Ti}\right)^2 + \left(POPL \frac{Te * DTi}{Ti^2}\right)^2} \quad (14)$$

The values were then compared to the original uncertainty estimate to contrast the two different methods.

3.2.2 Sondrestrom. The ISR data from Sondrestrom consisted of a single density profile from their steerable antenna with an associated uncertainty. The radar used a 450-μsec pulse length and was integrated over 10 minutes to attempt to get sufficient signal to measure the topside ionosphere. The antenna was pointed parallel to the earth's magnetic field line which intersects near-perpendicularly with the surface at that latitude, called "up B." To measure "up B" the antenna is elevated to approximately 80 degrees (with 90 degrees being vertical) and to 141 degrees azimuth (with 0 degrees

being north). These returns, at best, extended to 840 km, with much of the topside data either having exceedingly high uncertainties or being missing altogether.

3.3 Description of DMSP Data

UTD provided the DMSP data. This group designed and built the SSIES sensors for the DMSP. They receive their data monthly from AFRL, who archives all the data telemetered from the satellites. See Table 5 for a description of the DMSP data provided. The data initially contained the velocity components (except for POLITE 10 and F11 data) and later contained Sensor Potential (SENPOT) and Solar Zenith Angle (SZA) to help determine when the satellite was sunlit.

Table 5: DMSP Data Description

Parameter	Description	Parameter	Description
Time	Seconds	alt	Spacecraft Altitude
Vx	m/s	frach	Fraction H ⁺
Vy	m/s	frache	Fraction He ⁺
Vz	m/s	fraco	Fraction O ⁺
density	cm ⁻³	Ti	Ion Temperature (K)
MLT	Magnetic Local Time	Te	Electron Temperature (K)
MLAT	Magnetic Latitude	SZA	Solar Zenith Angle
glong	Geographic Longitude	SENPOT	Sensor Potential
glat	Geographic Latitude		

Vx was derived from the RPA. According to Hairston (private communication, 11 December 2000), coordinates for the velocity vary from those quoted by Rich (1994). In these data, +Vx is in the direction of spacecraft travel, +Vz is vertically directed away from the earth's center, and +Vy is a horizontal flow that points to the left of the spacecraft's path. In general, this has +Vy pointing west during an ascending node and east during a descending node. Since the DMSP orbit is nearly circular, Vx represents a

horizontal flow as well. Density fractions of O^+ , H^+ , and He^+ are also derived from the RPA. This analysis has known problems that result in the reported constituent concentration going to zero when it decreases to less than eight percent of the total density (Hairston, private communication, 23 August 2000).

The density was taken from the SM, which samples the plasma environment 24 times per second. These values can also be derived from the RPA, but require considerably more processing to extract. The SM provides a straightforward number density measurement and should be unaffected in its range by the composition. If mass densities were needed, a more robust routine analyzing the RPA output would have been required.

The DMSP/SSIES data files start when the satellite crossed the geographic equator during the ascending node, and continued for one orbit, covering approximately 101 minutes. This translates to the satellite covering a little over three-and-a-half degrees latitude every minute. The data were averaged into four-second bins; so one orbit generated roughly 1500 data points. Figure 16 shows how this averaging creates a marked smoothing in the data, practically eliminating any indication of measurement error, although it does allow the physical structure of the ionosphere to be evident without much noise.

AFRL and UTD have found several problems with the various DMSP sensors. These problems range from systematic problems that removed the satellite from service, to temporary problems that eventually resolved themselves. The following list details the

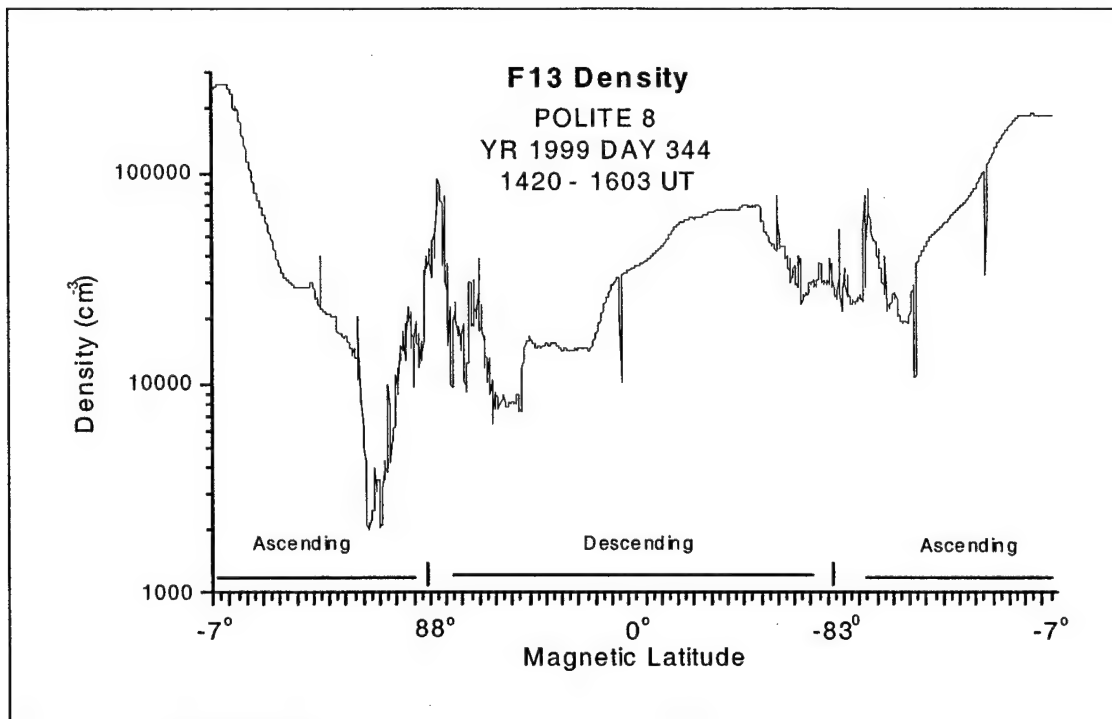


Figure 16: Example of one complete DMSP orbit, starting at the equator on the ascending node.

DMSP sensor problems that impacted this study:

1. F14 RPA derived-data were unreliable from September 1999 to January 2000, with recurrences in July 2000. This seems to be tied to a SENPOT problem.
2. F12 SM density measurement was inaccurate after the satellite left the auroral oval in the morning-side, descending node in the Northern Hemisphere winter. This was clearly evident during POLITE 1 and 2, but corrected itself during later orbits. This was attributed to O^+ composition being less than 50 percent of the total ion density.
3. F13 electron temperatures ~ 1000 K too high while the satellite is sunlit.
4. During POLITE 6, the DMSP were set in a mode to measure effects of a meteor shower on the satellites. During this period, no RPA was telemetered and the EP was set to only record once every 30 seconds.

3.4 Comparison of ISR and DMSP Data

To compare the ISR density data to the DMSP data, overpass times were required. Potential overpass times were computed using an AFRL-provided program that took the ephemeris data for the DMSP satellites and determined when the satellites were within five degrees of the radars, following Sultan and Rich (2000). Initially, the overpasses were computed for all the Western Hemisphere ISRs. This was compiled into a list of 394 potential conjunctions over the four sites for POLITEs 1 - 9. The list broke down to 69 potential overpasses for Arecibo, 71 for Jicamarca, 85 for Millstone Hill, and 169 for Sondrestrom. This turned out to be overly optimistic, since some data were unavailable from both the DMSP and radars for all the prospective times. Also, some of the conjunctions determined by this method were on the fringes of the five-degree circle and provided an insufficient number of data points (arbitrarily set at ten data points for the five degree circle) from the DMSP to be useful.

After receiving the DMSP data, it was discovered that F10 data were unavailable and F11 was available only for POLITE 6. As to be expected, some of the DMSP data from the available satellites and times were missing. On the plus side, DMSP data were available for POLITE 10. Using the geographic latitude and longitude from the DMSP files, each data point was checked to see if it fell within a five-degree circle of the radar sites. This was accomplished using a simple Pythagorean routine. Data points that fell within the circle were used to determine the actual time of the overpasses for comparison with the radar data files. This step resulted in a total of 37 conjunctions of the DMSP satellites with the Millstone Hill radar and 56 conjunctions with Sondrestrom. Later analysis indicated a one-degree circle should be used over Sondrestrom due to the

amount and variation of ionospheric structure at that latitude. Since Sondrestrom was pointed “up B,” the one-degree circle needed to be offset from the radar site to account for the departure of the beam from vertical. The center of the circle was found using trigonometry, taking into account the high-latitude of the site. This resulted in 15 overpasses of the DMSP satellites within one degree of the Sondrestrom “up B” location, with corresponding ISR data for seven of the overpasses.

Each overpass is referred to with a simple naming convention of the form RP-N. R is “M” or “S” for either Millstone Hill or Sondrestrom. P is the POLITE campaign number from Table 2, and N is the chronologically sequenced number for all conjunctions in the campaign. Cases with an “E” appended to the end had the ISR uncertainty re-evaluated using equation (14) from section 3.2.1, and were used in the case studies for a comparison of the error propagation techniques. These cases were also used when comparing measurements from two different DMSP spacecraft directly.

The SSIES density data were averaged over the prescribed circle. The average was used for the comparison, while the standard deviation of the SSIES density data indicated how much structure was evident in the ionosphere overhead of the ISR.

Since Millstone Hill provided three different pulse-length returns (See Section 3.2.1), each pulse length was plotted to determine useable returns. Using the criteria from Sultan and Rich (2000), two good consecutive profiles within ± 30 minutes of the conjunction were required. When this occurred, all the data points within the time window were used to arrive at a representative ISR value for the overpass. Figure 17 shows examples of each. Two separate techniques were then used to calculate a value for the ISR measurement.

On the long pulse lengths, the integrated return covered more than the ± 25 km vertical interval used by Sultan and Rich (2000), so the value for the bin closest to DMSP altitude was used and averaged over all the returns for the overpass. For the 1000 μ sec pulse length, this altitude bin was 874 km and represented the return integrated vertically over ± 75 km. With the 2000 μ sec pulse length, the 844 km bin was used which was integrated over ± 150 km. The data were considered useable if all the measurements required to determine the uncertainty in the corrected density (DNEL) were available (See equation (12)). NEL and DNEL were used for the comparison.

The second method for Millstone Hill took all the useable data (as described above) and fit a curve to all the topside data. When possible, the curve was fit to an exponential of the form

$$y = a + b * \exp\left(-\frac{x}{c}\right) \quad (15)$$

to attempt to stay consistent with the concept that the atmospheric density decays exponentially with height, as given by:

$$n_i = n_{i_0} e^{-(z-z_0)/H} \quad (16)$$

where n_i is ion species density, z is altitude, H is scale height, and the “0” subscript indicates an arbitrary initial altitude. Alternatively, a different exponential or logarithmic equation form was used if no fit could be found to equation (15) by the TableCurve™ 2D program (Version 4). The fit was visually compared to the density plot to ensure it

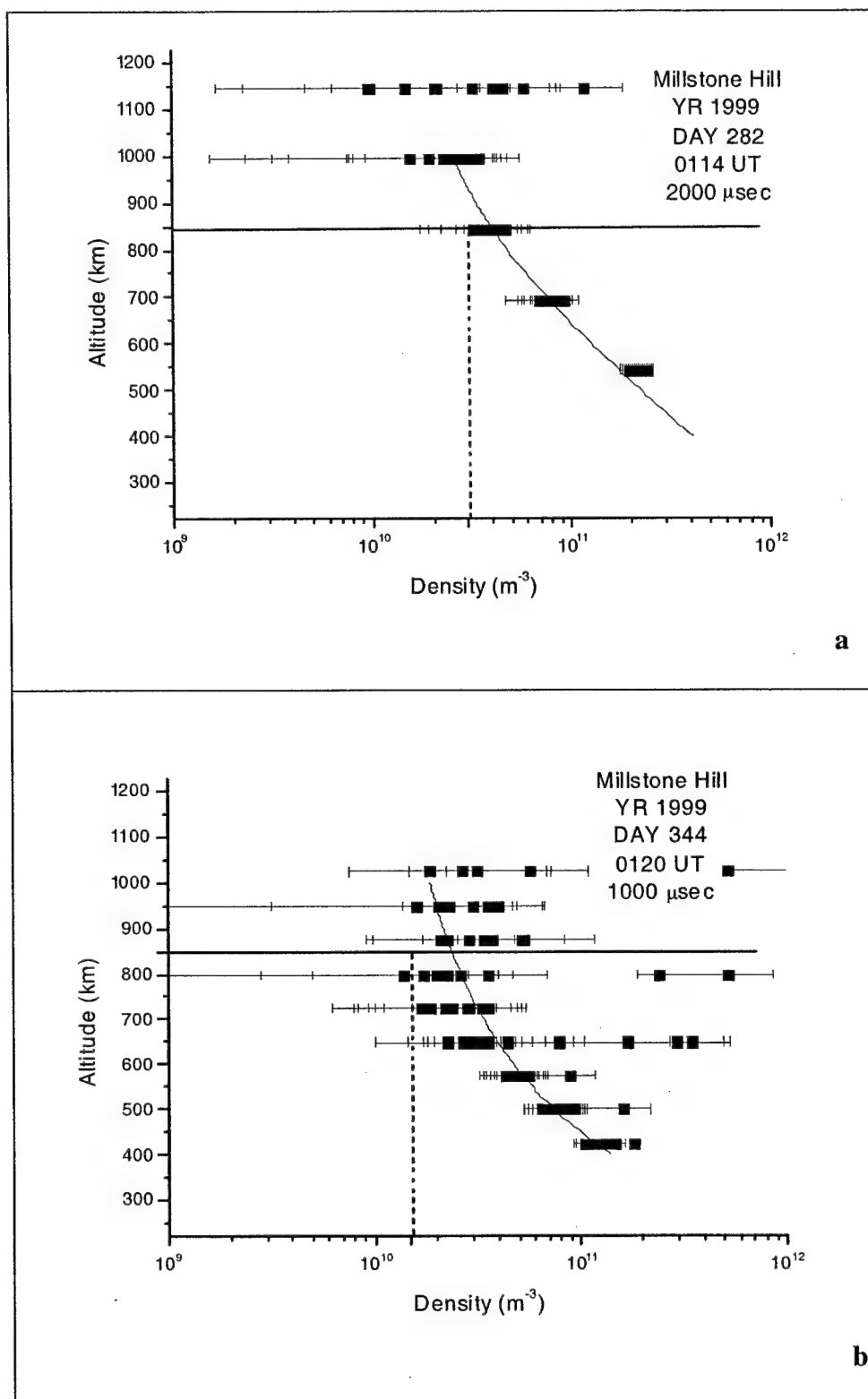


Figure 17: Example of Incoherent Scatter Radar Returns: (a) Millstone Hill 2000 μsec pulse; (b) Millstone Hill 1000 μsec pulse; (c) Millstone Hill 410 μsec pulse; and (d) Sondrestrom. The vertical dotted line shows the DMSP-measured average density.

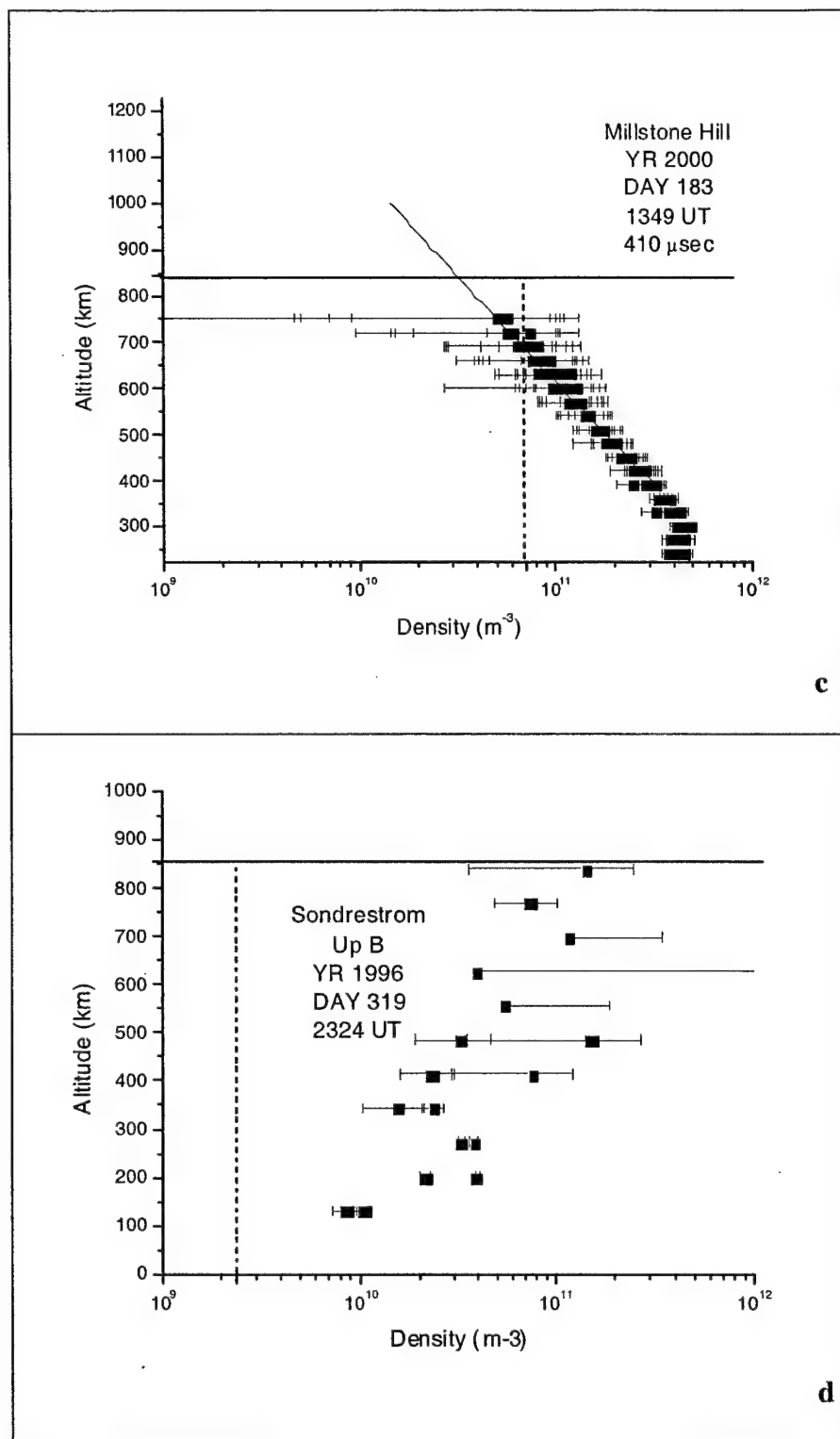


Figure 17 (c & d)

represented the ionosphere as measured by the ISR at the DMSP altitude. Obtaining a good fit was occasionally a problem because the transition from O⁺ dominance to H⁺ dominance occurs in this altitude range. The differences in scale heights of O⁺ and H⁺ served to create vastly different profiles, evident in Figure 17b. As seen in the definition of scale height:

$$H = \frac{k_B T_i}{m_i g} \quad (17)$$

with k_B again being Boltzmann's constant, T_i is ion temperature for species "i", m_i is the ion's mass, and the acceleration of gravity $g = 9.8 \text{ m s}^{-2}$ (Taken as constant here). The mass dependency of H leads to a factor of 16 between the two values. This approach also assumes that the ion temperature remains fairly constant, which is not necessarily the case. This forced the fit in some instances to be only locally consistent with the profile.

This fit curve was then either interpolated (long pulse lengths) or extrapolated (410 μsec pulse length) in 5 km steps to the DMSP altitude. The number calculated from the fit was manually compared to the actual returns for internal consistency and against the DMSP measurement. Also, following Sultan and Rich (2000), the fit data were averaged over $\pm 25 \text{ km}$ altitude of the DMSP as a tertiary comparison.

Sondrestrom used only one pulse length, so only one set of NEL and DNEL were available. Since a one-degree circle represents less than one minute of DMSP data, only the radar returns immediately before and after the overpass were examined. When data were present at 840 km for both profiles, the two values were averaged and compared directly to the DMSP average. Otherwise, the single reported value at 840 km of the valid return was compared directly to the average DMSP measurement. Figure 17d

shows a typical example where there was no simple extrapolation possible due to the large ionospheric variability.

The second part of the research focused on the variations of the DMSP measurements attempting to classify the random noise in the measurements and the ability of the sensor to measure variability in the ionosphere. The variability of the DMSP density data was diagnosed using the following sequence:

1. Perform a linear regression on the raw data.
2. Determine residuals by subtracting the fit from the raw data.
3. Compute mean (should be near zero) and standard deviation on the residuals.
4. Remove data with residuals outside of 2σ of the residual mean.
5. Compute average of the filtered data, i.e., raw data with 2σ points removed.
6. Perform a linear regression on the filtered data.
7. Determine residuals by subtracting the fit from step 6 from the filtered data.
8. Compute standard deviation of the filtered residuals and compare to the mean of the filtered data. (i.e., σ/\bar{X}).

This sequence served to first de-trend the data. After this, the outliers ($> 2\sigma$) were removed, and the remaining data were again de-trended. The final step served to provide a measurement of the relative data variability.

The statistics of the data were computed using the Numerical Recipes' "moment" subroutine from Press *et al.* (1996), and the linear regression was calculated from the "fit" subroutine in the same source. These are fairly straightforward routines, taken in their entirety to simplify the programming process.

Using a simple linear regression to de-trend the data forces some assumptions. First, it is assumed that in mid-latitudes, the latitudinal scale length of the variations in N_e is large and can be sufficiently approximated by a straight line. In auroral regions, both the temporal and spatial scale of variations is considerably shorter. Another assumption is that the ionosphere is quiescent. In geomagnetically active periods (i.e., geomagnetic storms), the spatial and temporal scales of the physical processes can be much shorter (10s of kilometers in space and minutes in time), so a linear fit over several degrees of latitude would not be appropriate. The vast majority of the cases had $Kp < 3.0$, which indicates the ionosphere was not being significantly perturbed by geomagnetic activity. The maximum Kp during the conjunction periods was 4.3, which is only moderately active.

A final check on the data was performed to determine whether the DMSP was located poleward of the equatorward edge of the aurora. This was accomplished using the EQB regression routine from AFRL (See Appendix D) and determining a local equatorward auroral boundary by taking the equivalent midnight equatorward boundary and converting it to the corresponding DMSP magnetic local time (MLT). The EQB values were retrieved from the CEDAR database maintained by NOAA's High Altitude Observatory, and the location and MLT of the satellite from the SSIES data. After converting the EQB to local time and latitude, the satellite's reported location was checked to see if it was poleward of this value. If any one point in the data set was poleward of the derived boundary, then the entire DMSP conjunction was classified "auroral."

IV. Results and Analysis

4.1 Comparison of DMSP *versus* ISR

Generally, comparison of DMSP SSIES-measured ionospheric densities to ISR-measurements was straightforward. Complications arose when trying to assess error for the measurements. The DMSP data contained no uncertainty associated with the measurements, and as Figure 18 shows, the density plots were too smooth to readily determine instrument noise, in contrast to the electron temperature. The Millstone Hill corrected electron densities also did not have associated uncertainties, but they could be determined as described in Section 3. Sondrestrom provided corrected electron density and the uncertainty in the measurement, so no further processing of the data was required before analysis.

4.1.1 Millstone Hill Overpasses. Several of the Millstone Hill cases demonstrated some signs of significant ionospheric structure. Each was examined for signs of a SAID, the MT, and the LIT. Also, three case studies were identified where two satellites over-flew the radar within ~40 minutes of each other. These were examined to see if the two satellites were in agreement with each other.

As shown in Figure 19, clear indications of a SAID were found in Case M1-1, although it occurred north of the comparison region. The density graph, Figure 19a, also shows an MT, with the gradual equatorward wall in evidence south of the radar. Looking at the velocity components for the same time in Figure 19b, where the total density is the lowest, a sharp increase exists in the westward velocity (V_y). A corresponding spike in

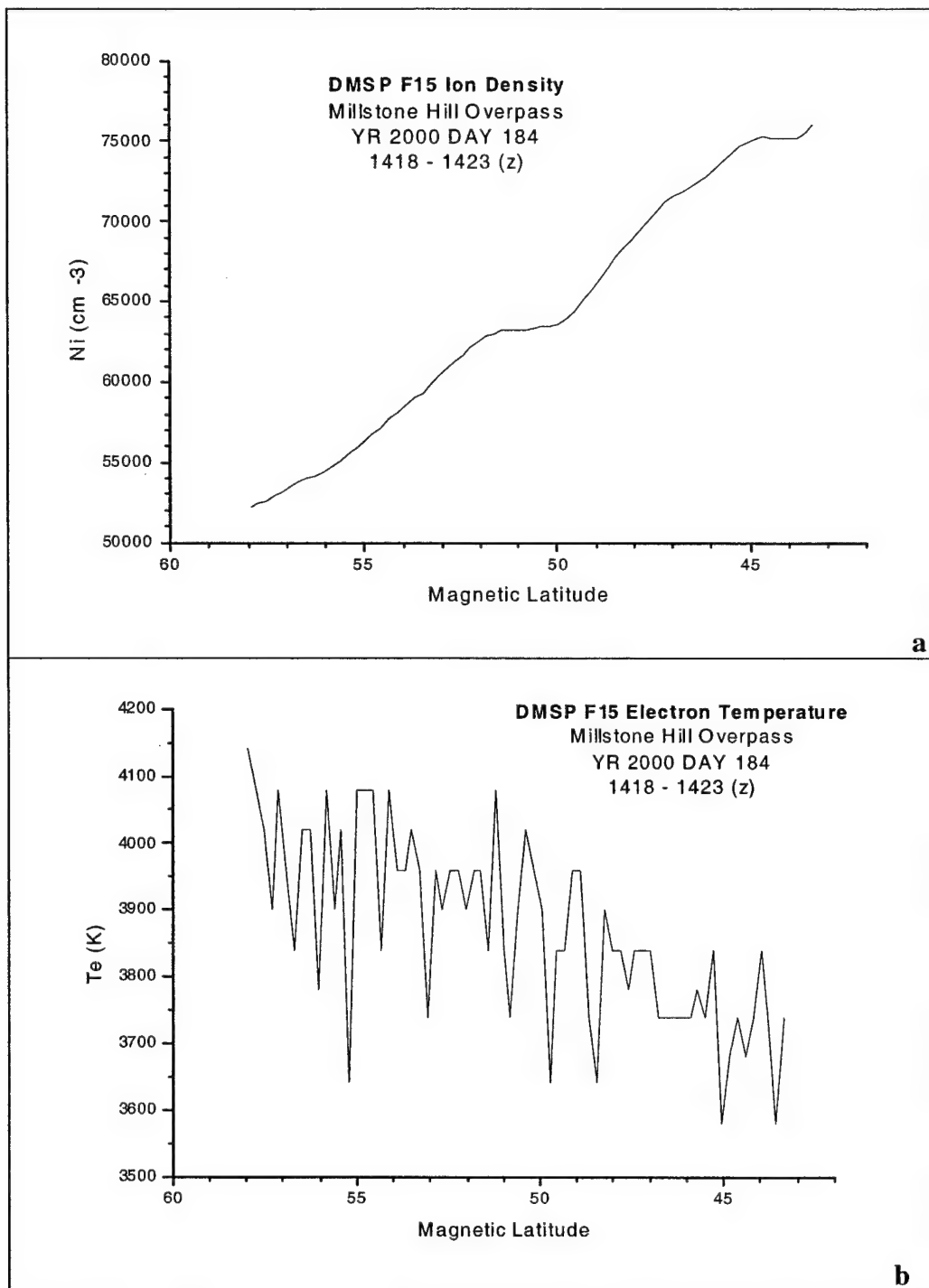


Figure 18: Example of random noise associated with DMSP (a) density and (b) electron temperature.

the electron temperature can be discerned in Figure 19c. Include the fact it occurred on the winter evening sector and that $Kp = 4.3$, and you have all the elements of the classic SAID signature. Figure 20 details case M1-2, which also shows signs of the MT, with T_e increasing as the density of O^+ decreases (slightly) accompanied by an increase in the horizontal velocity (The DMSP was in a descending node, which is reflected as decreasing magnetic latitude on the abscissa). Also there are indications of the LIT as well, with H^+ density increasing from under 1000 ions/cm³ to nearly 6000 ions/cm³. Figure 20a illustrates problems with the RPA when the concentration of O^+ appears to range from zero percent to 100 percent of the total N_i within several seconds.

Similar results are found throughout this data set for Millstone Hill. Table 6 gives a synopsis of these phenomena found in this study. Classification of some events was impossible due to missing or bad RPA data, which gives fractional densities as well as V_x . Velocities were not available during POLITE 10, and F14 T_e for POLITE 10 was unreliable.

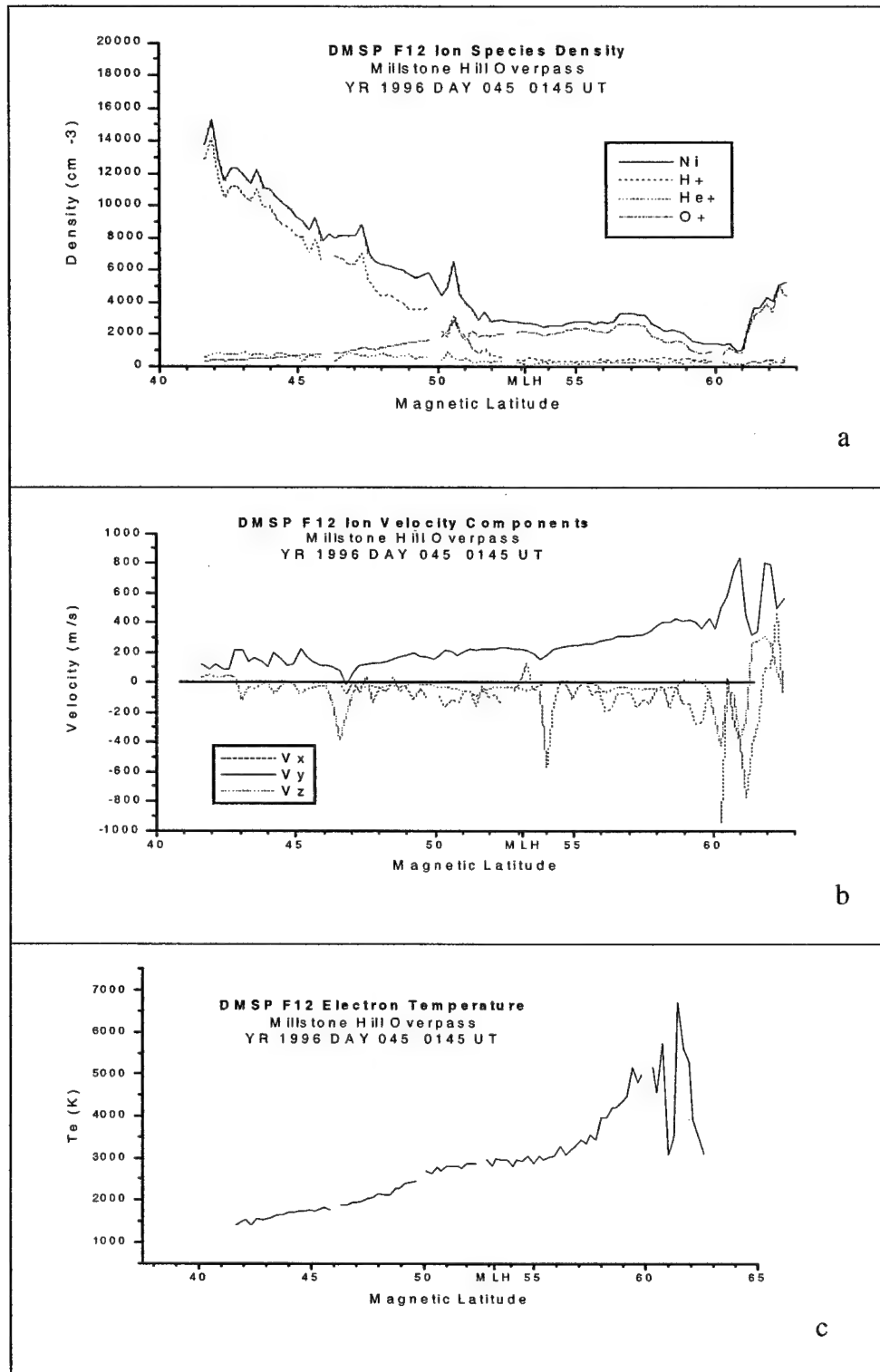


Figure 19: DMSP-measured (a) density, (b) velocity, and (c) T_e for case M1-1 showing a MT south of 50°N mag lat and a SAID near 60°N mag lat.

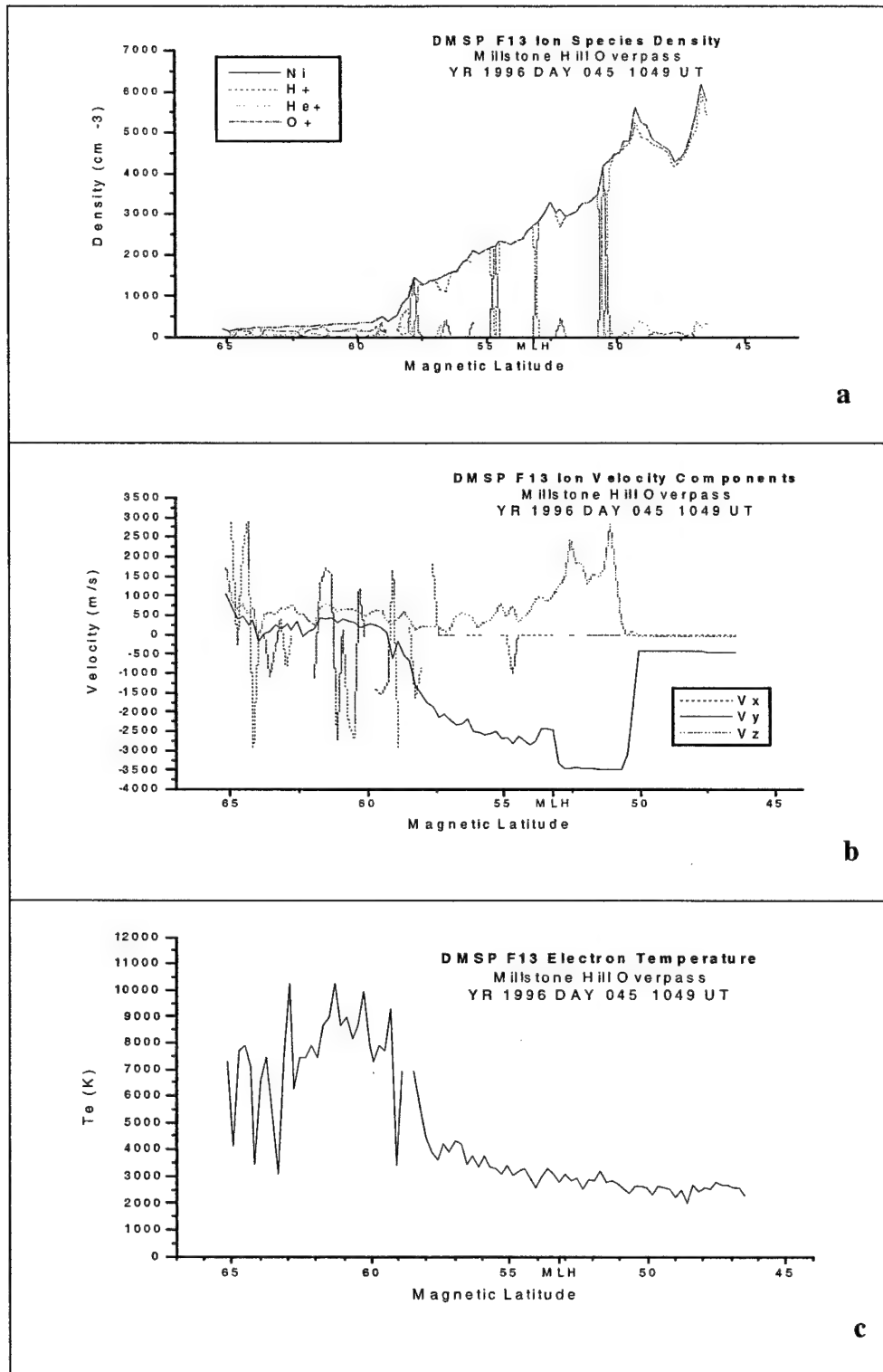


Figure 20: DMSP-measured (a) density, (b) velocity, and (c) T_e indicating a possible MT south of 50°N mag lat and a LIT north of that point.

Table 6: Ionospheric features found during Millstone Hill overpasses.

Case	SAID	MT	LIT	Case	SAID	MT	LIT
M1-1	X	X	X	M6-1		X	
M1-2		X	X	M6-2		X	
M2-1			X	M6-3			
M2-2			X	M7-1			
M2-3				M7-2			
M3-1				M7-3		X	
M3-2				M8-1			
M3-3				M8-2		X	
M3-4				M8-3			
M3-5				M9-1			
M4-1		X	X	M10-1			
M4-2		X	X	M10-2		X	
M4-3				M10-3		X	
M4-4		X	X	M10-4		X	
M4-5			X	M10-5		X	
M5-1				M10-6		X	
M5-2				M10-7			
M5-3				M10-8			
M5-4							

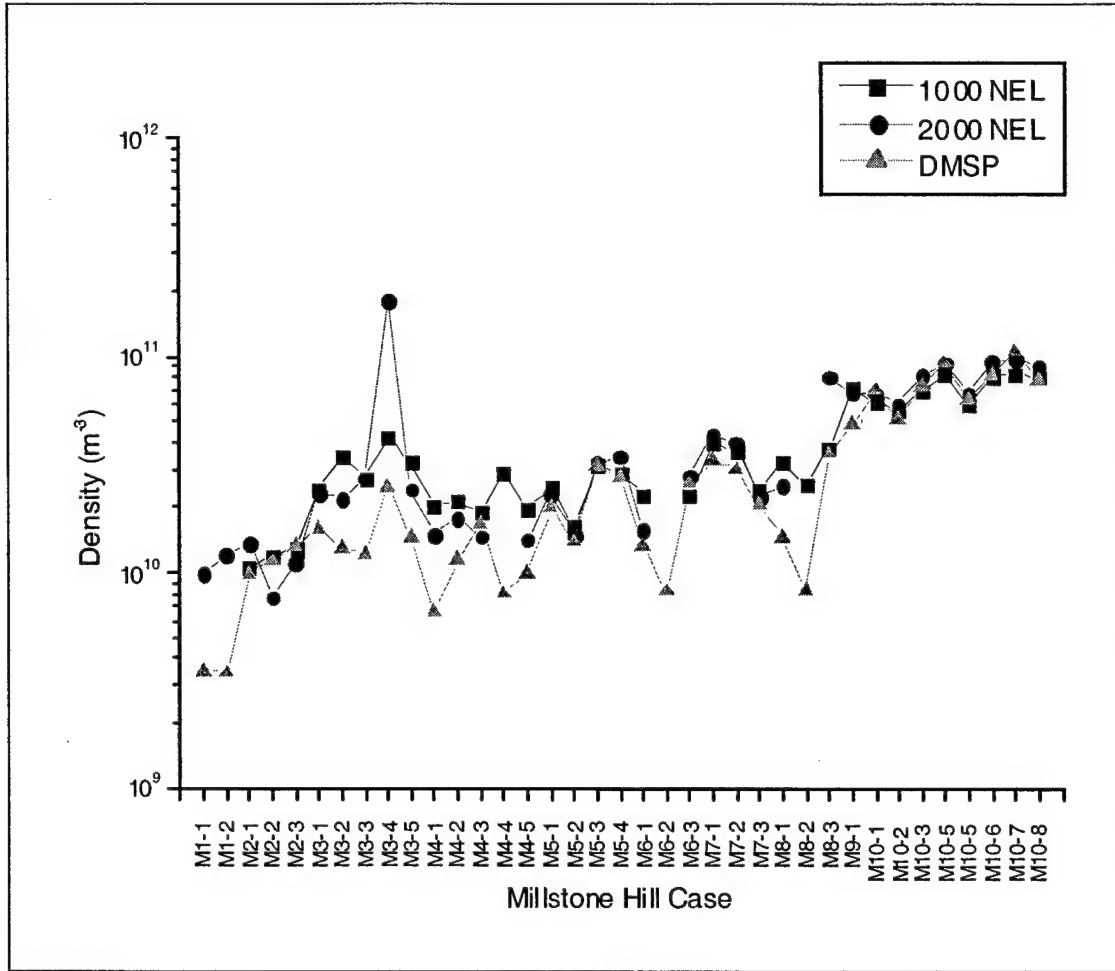


Figure 21: Millstone Hill conjunctions showing ISR and DMSP measurements.

As mentioned before, 37 conjunctions were found for Millstone Hill. Figure 21 shows the DMSP measurements with the Millstone Hill 1000 μsec and 2000 μsec densities measured at 874 km and 844 km, respectively. By inspection, the DMSP values show a negative bias when compared to the measured NEL, and will be discussed in detail in Section 4. Each profile is detailed in the available supplement, showing the ISR measurements with their associated uncertainties. In the same appendix, the ISR measurements and uncertainties from the altitude bin closest to DMSP altitude are

displayed as a time series to demonstrate the temporal variability of the density. The DMSP data are plotted on the same page.

The ISR measurements were found to have large uncertainty at DMSP altitudes. Figure 22 and Figure 23 show how the ratio of DNEL / NEL varied for the two pulse lengths. Both graphs show a similar trend. The ratio of the uncertainty decreases as the solar cycle goes from the minimum during the early campaigns, to solar maximum during the later campaigns. This was expected, since the increasing solar flux would cause the topside ionosphere's density to increase. This would return a stronger signal and less noise to the ISR, which is what the graphs show. This being the case, the later

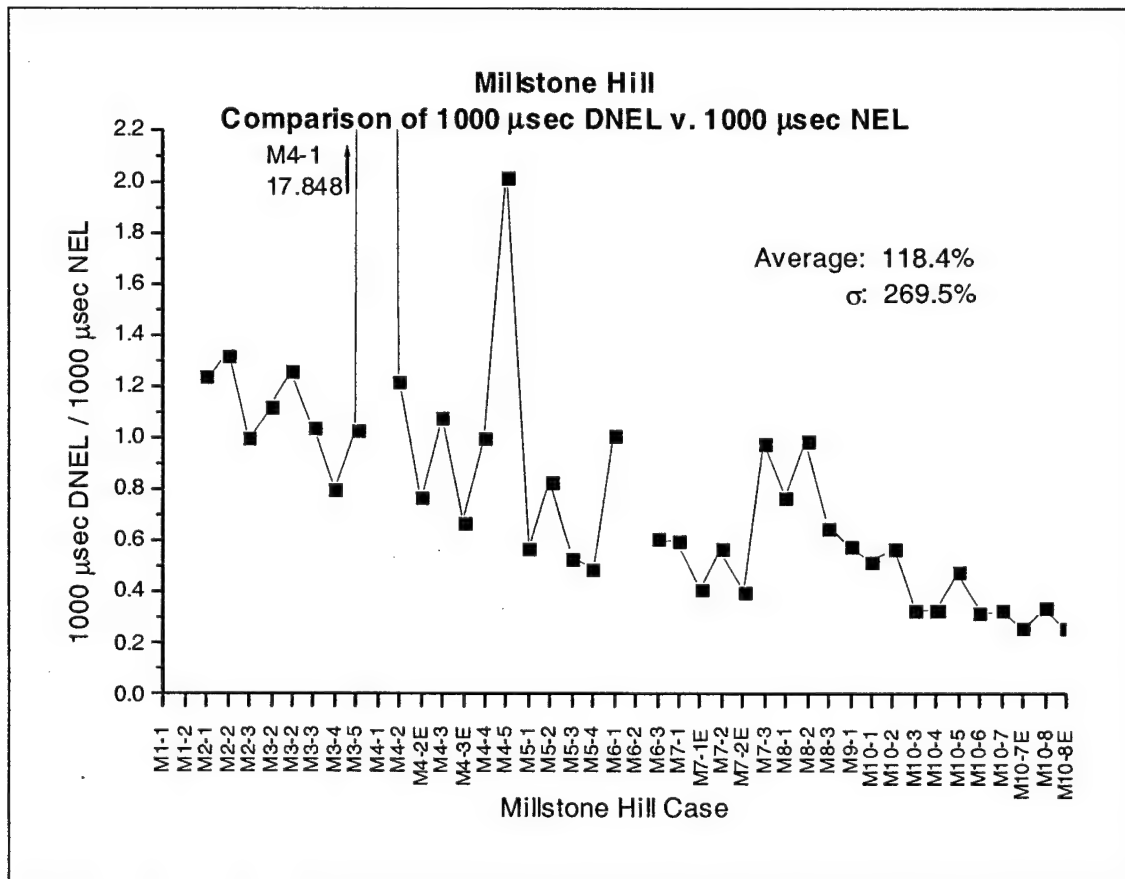


Figure 22: DNEL / NEL for Millstone Hill 1000 μ sec pulse length at 874 km.

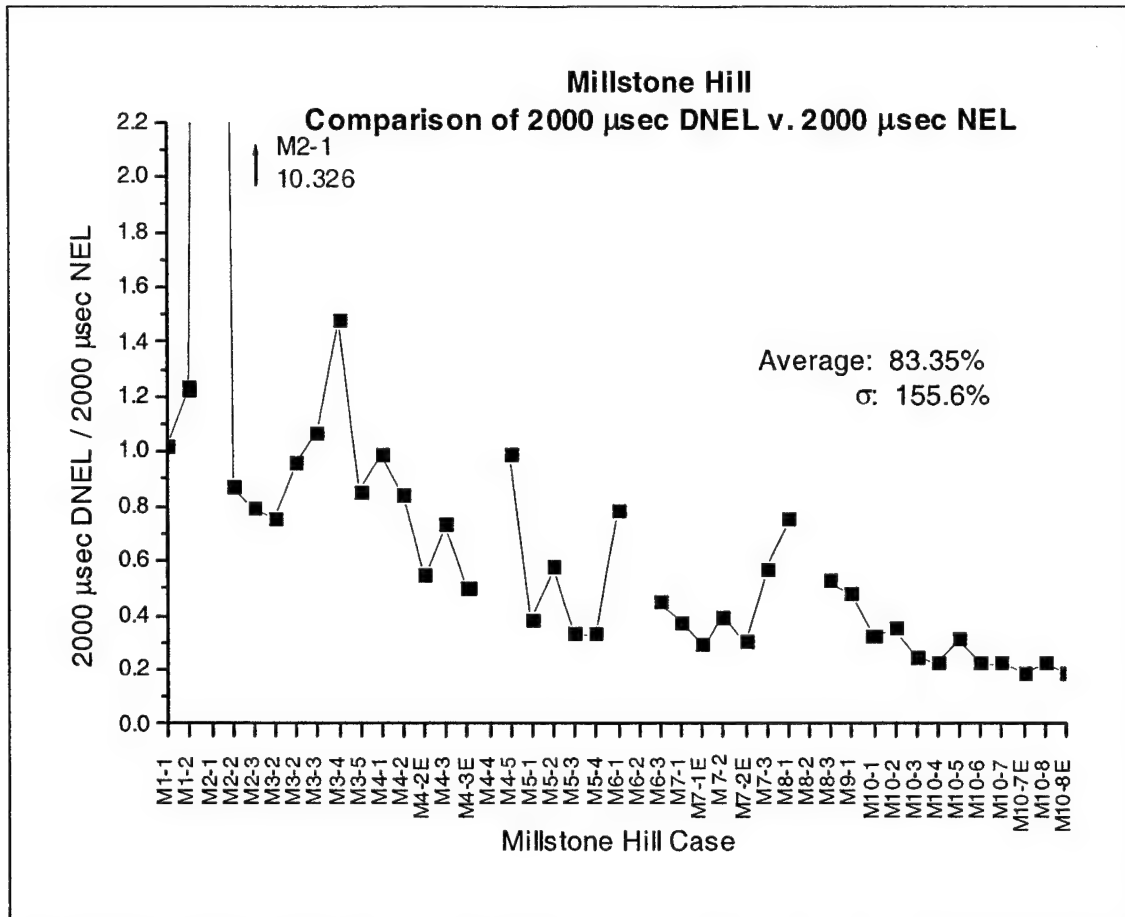


Figure 23: DNEL / NEL for Millstone Hill 2000 μ sec pulse length at 844 km.

POLITE dates still yield greater than 20 percent uncertainties. Even for the cases where the lower bound error estimate was used, the lowest ratio was 18.73 percent in Case M10-8E.

As a rough estimate of the DMSP uncertainty, Figure 24 plots the standard deviation of the measurements within the five-degree circle was compared to the average of those measurements. This did not take into account any of the “physics” that occurred in the ionosphere at that time, which can show up as a steady trend in the data, as in the case the satellite is entering or leaving a trough, or as large, local changes in the density

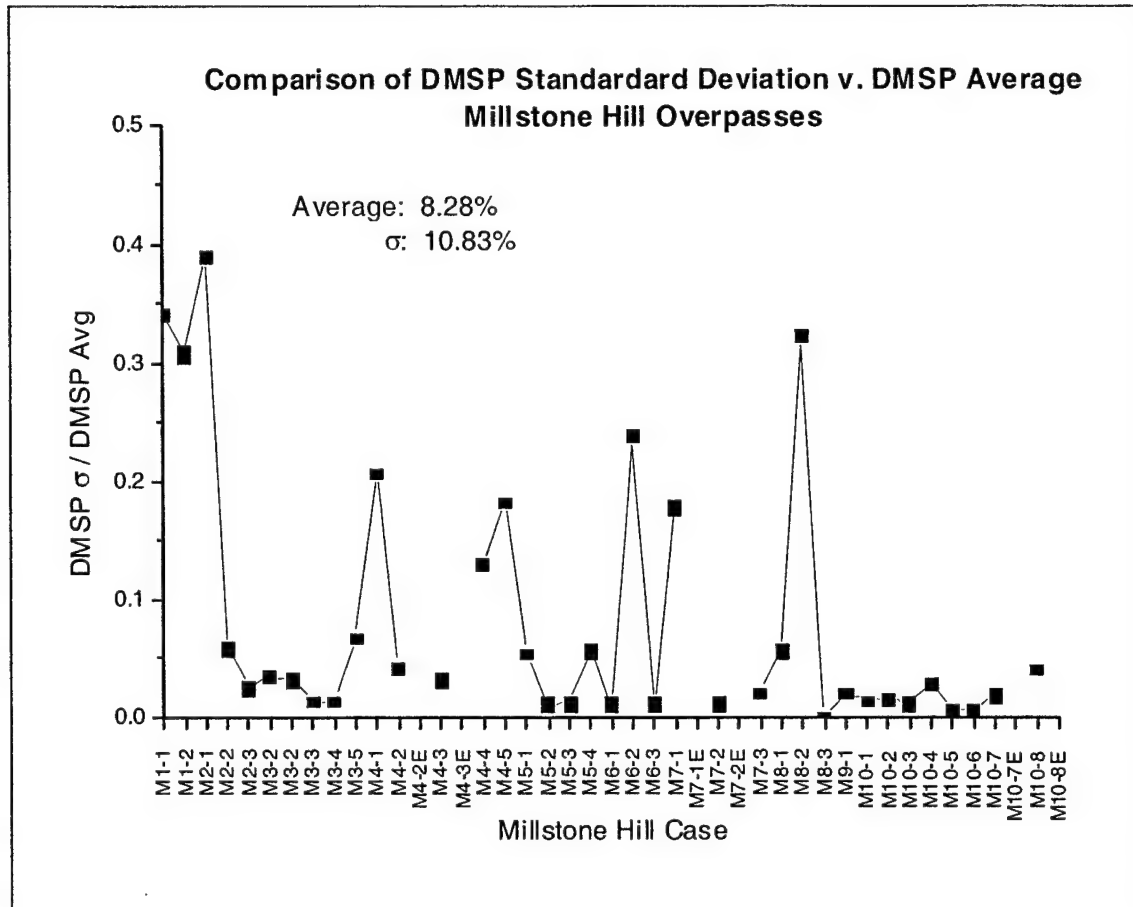


Figure 24: DMSP σ / DMSP Average for Millstone Hill Overpasses.

from small-scale structure along the DMSP's path. Any physical process that drove large variations in the overpass region resulted in a large standard deviation and so were treated as part of the instrument variation. A more detailed examination follows in Section 4.2.

To compare the DMSP to the ISR measurement, the relative error was calculated for each case. This was accomplished treating the ISR as the "true" reference value and comparing the DMSP value to it using the equation:

$$\text{Relative Error} = \frac{(DMSP - NEL)}{NEL} \quad (18)$$

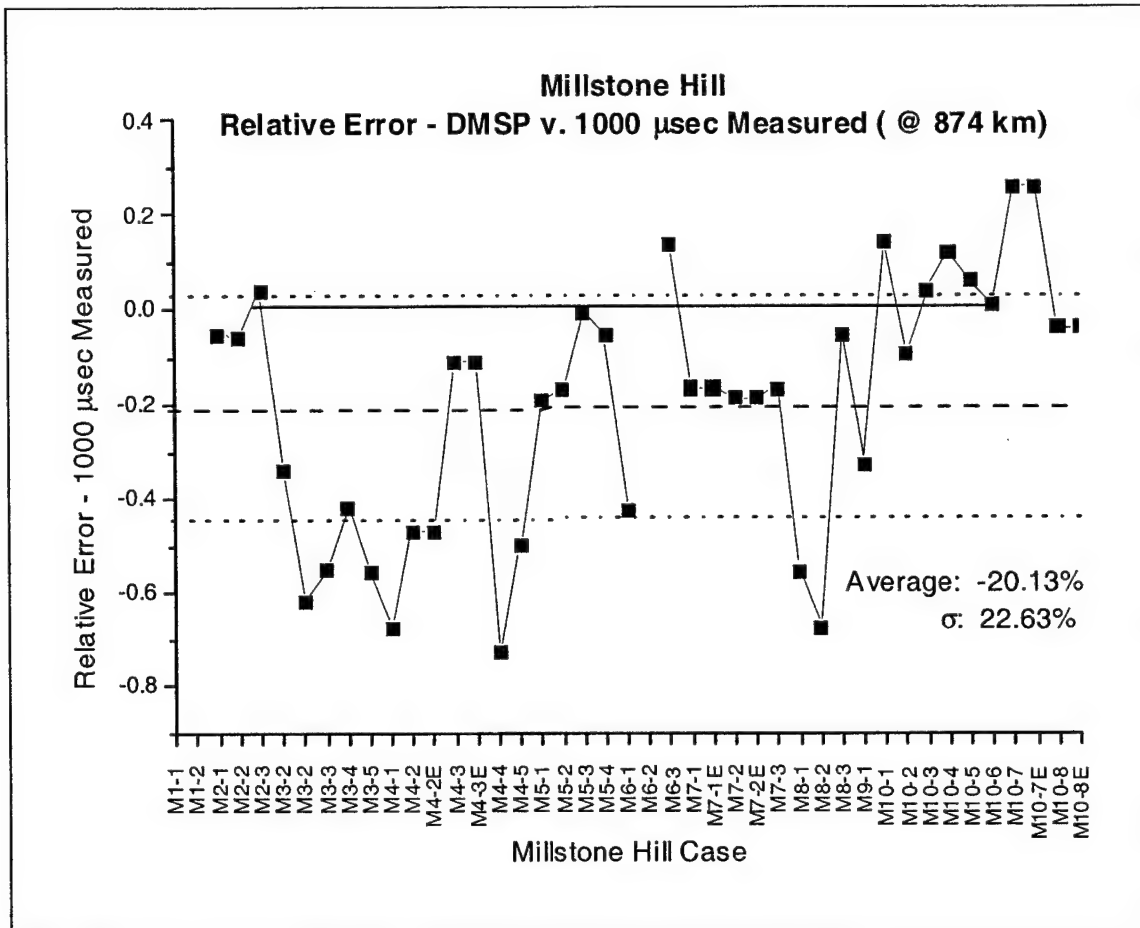


Figure 25: Relative error DMSP v. MLH 1000 μ sec measured at 874 km.

Values for relative error were computed for each type of comparison described in Section 3.4. After analysis, the values determined for the fit averaged over ± 25 km were not sufficiently different from the fit value calculated at DMSP altitude. Figure 25 and Figure 26 show the relative error of the DMSP *versus* the ISR-measured data from the data bin closest to the DMSP altitude. For both the 1000 μ sec and 2000 μ sec pulse lengths, the DMSP shows a definite trend to measure 20 percent and 22 percent low on average, respectively. However, referring to the ISR graphs in the supplement, the DMSP values fall well within the uncertainty of the radar measurements.

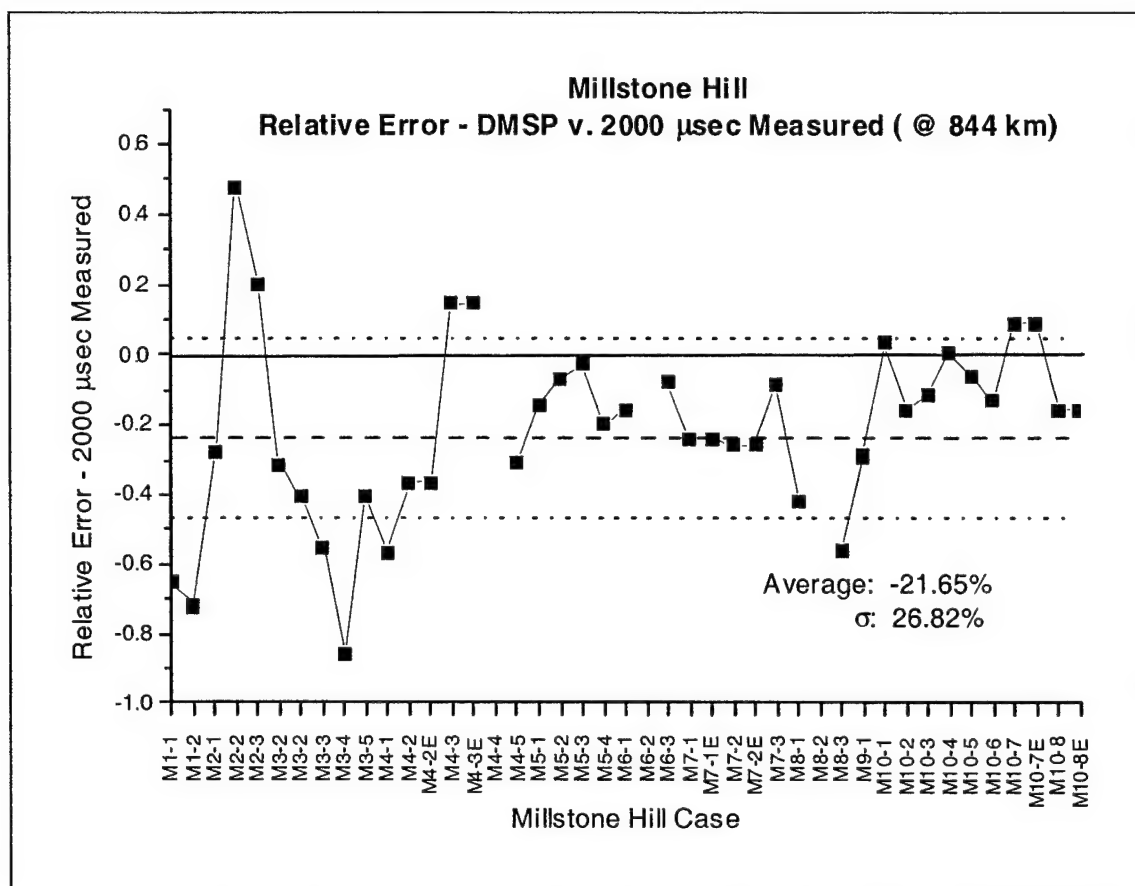


Figure 26: Relative error DMSP v. MLH 2000 μ sec measured at 844 km.

The fit data showed a similar trend, but since the data were analyzed through the entire profile for a representative fit, the relative error was generally less. To illustrate this point refer to Figure 27, Case M2-1, 2000 μ sec. The ISR-measured density was increasing at 844 km, due in part to the change from an O^+ -dominated to H^+ -dominated ionosphere. Fitting the data for the profile reduced the effect of this increase, with the fit value at the DMSP altitude (in this case 846 km) being less than the average ISR-measured data by nearly 1.5×10^9 -- over 10 percent of the value. The ISR data bin was at 844 km, and it is unreasonable to assume the mid-latitude ionosphere would vary that much in only two kilometers.

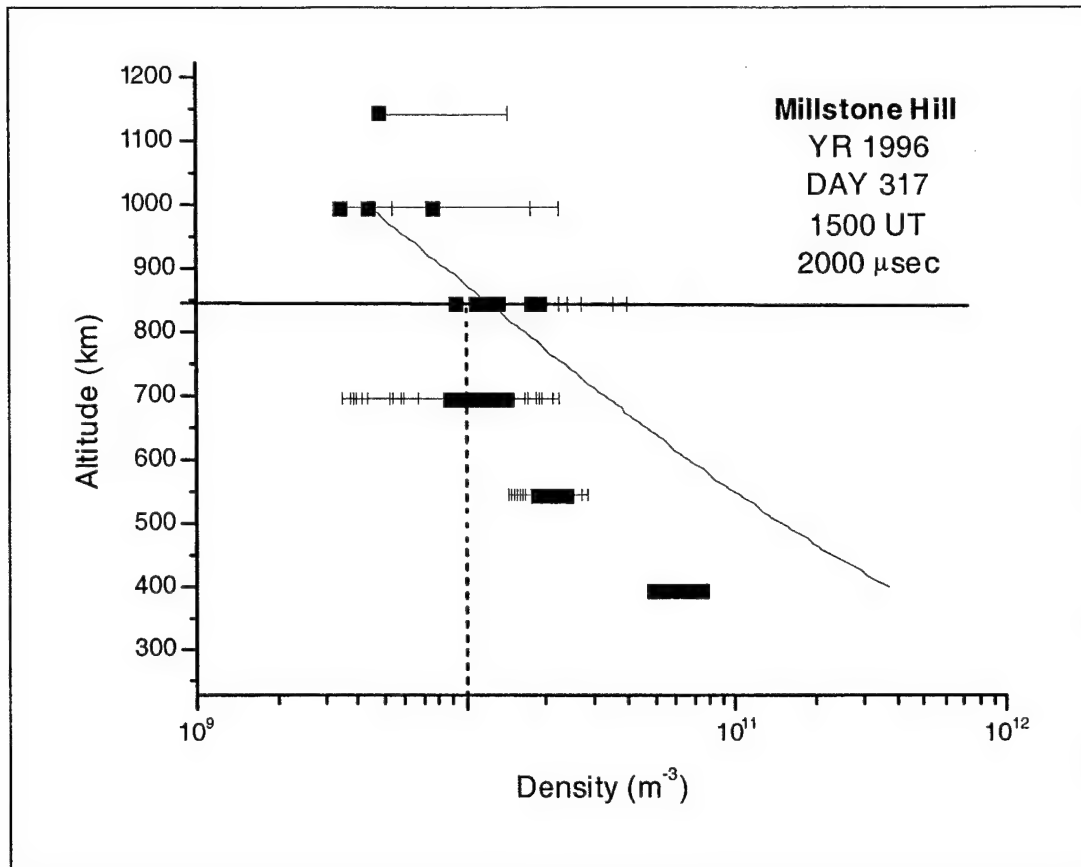


Figure 27: Case M2-1, 2000 μsec . Example of fit performing better than measured data.

The average relative error of the 1000 μsec fit was under negative nine percent with a standard deviation of 23 percent. While still measuring low compared to the ISR, the DMSP has a better agreement, but with 40 percent of the distribution greater than zero. Figure 29 shows the absolute value of the relative error of the data and shows the DMSP measuring 25 percent difference from the Millstone Hill ISR. From these two graphs, it appears the DMSP measurements are biased to the low side of the Millstone Hill ISR, particularly toward solar minimum.

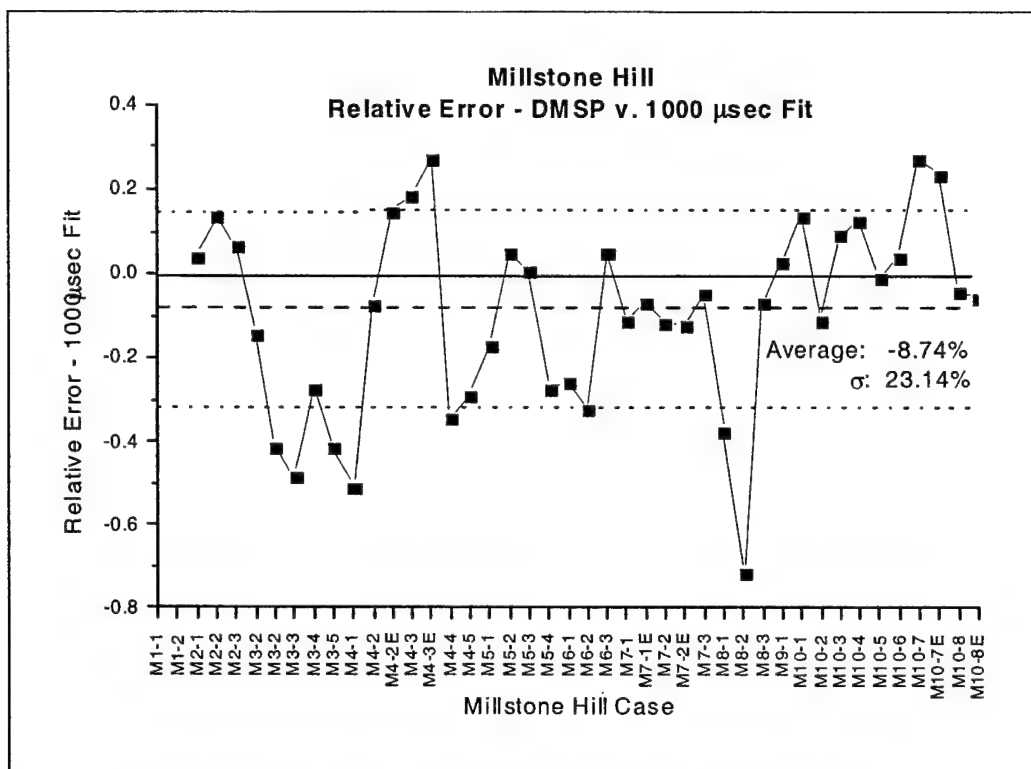


Figure 28: Relative error DMSP v. MLH 1000 μ sec fit data at DMSP altitude.

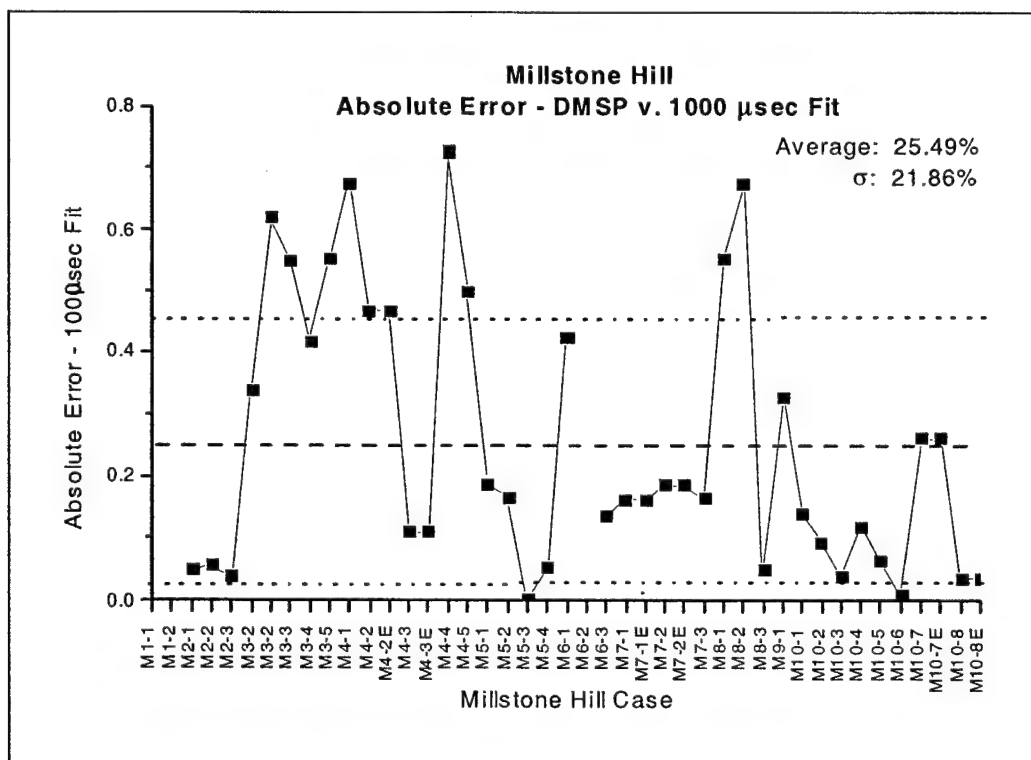


Figure 29: Absolute error DMSP v. MLH 1000 μ sec fit

Figure 30 shows the relative error of the 2000 μsec pulse length fit of the Millstone Hill data has an even greater negative difference than the 1000 μsec fit data, but with similar variability. The absolute error of the 2000 μsec pulse has similar characteristics (not shown).

The relative error of the 410 μsec fit data in Figure 31 showed an average positive difference of 10 percent, but with substantially increased variability over the other two fits. This increased variability resulted from the return not showing the structure above the heavy/light ion transition. If this occurred above 700 - 750 km, there was no indication in the profile, and so could not be accounted for. For those profiles that did show indications of the transition at lower altitudes, it was difficult to account for the transitions since the data cut off close to the changeover.

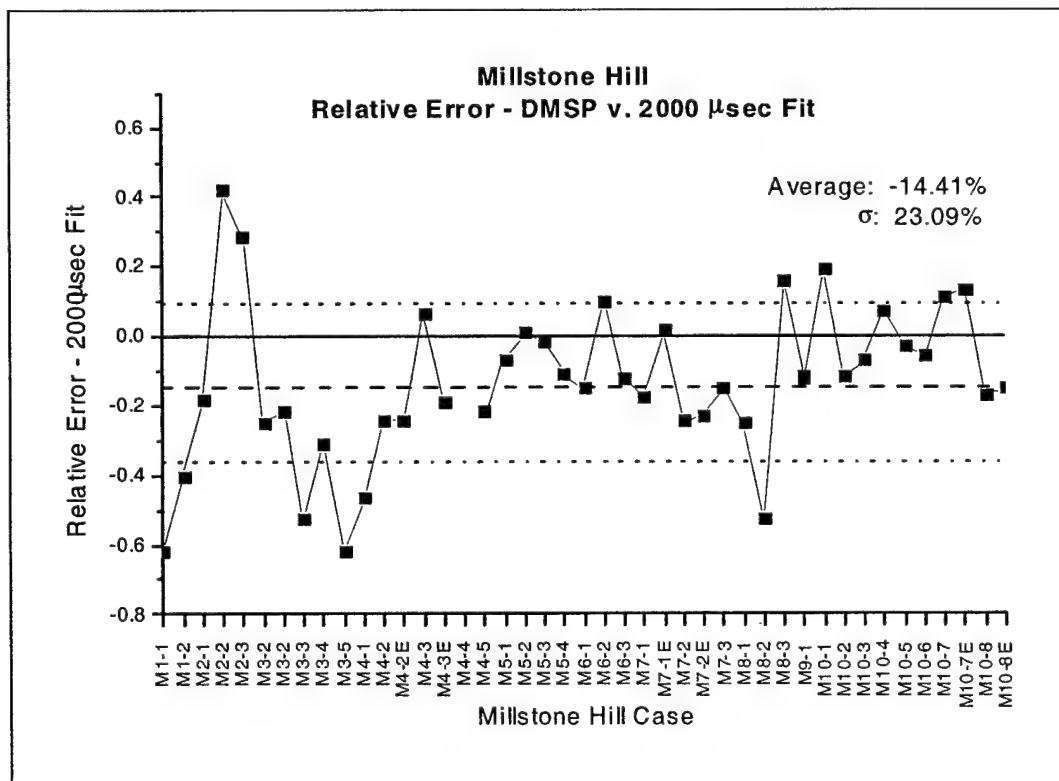


Figure 30: Relative error DMSP v. MLH 2000 μsec fit at DMSP altitude.

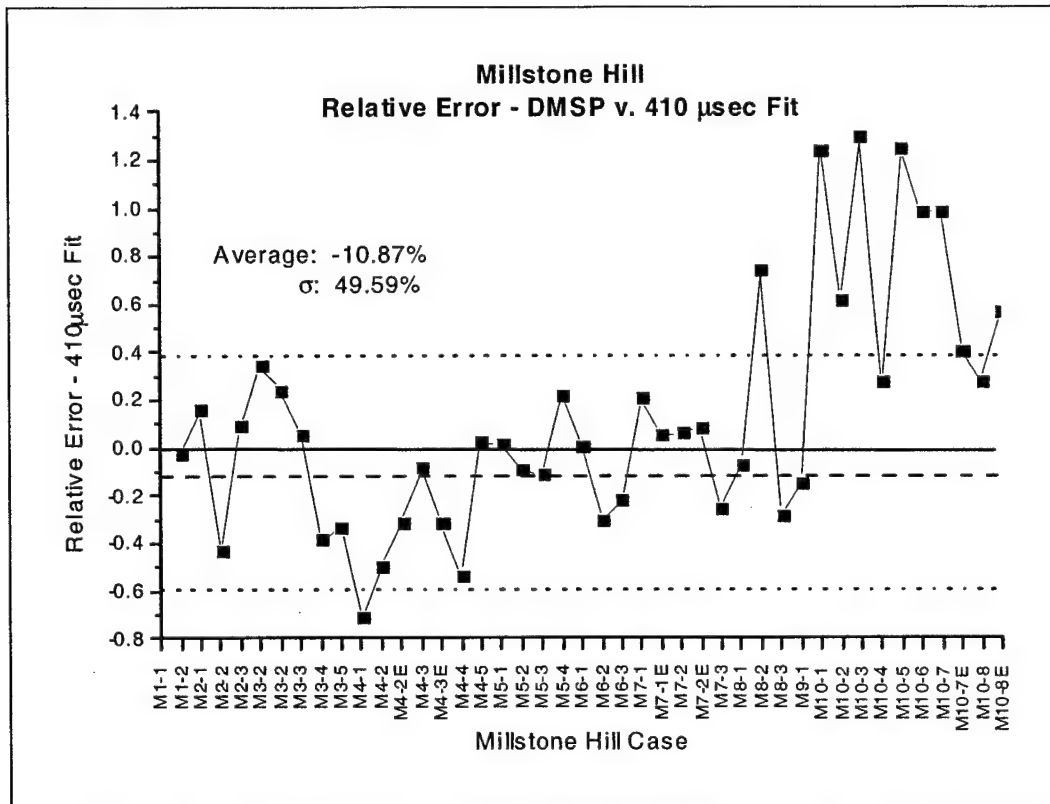


Figure 31: Relative error DMSP v. MLH 410 μ sec fit at DMSP altitude.

4.1.2 Millstone Hill Case Study. Three sets of cases were observed where two separate DMSP satellites flew over the Millstone Hill site within 45 minutes of each other. These were selected since the mid-latitude ionosphere would reasonably be expected to not have changed much on this time scale. This way, a direct comparison between two separate satellite instrument packages is possible. The cases studies were M4-2/M4-3, M7-1/M7-2, and M10-7/M10-8. Table 7 presents the individual studies with the earlier overpass (UT) compared to the later. The ratio (earlier/later) in the DMSP measurements is contrasted to the ratio in the ISR measurement for both long pulse lengths. This serves to relate the changes in the DMSP measurements to any real structure in the ionospheres, as determined by the ISR.

Table 7: Comparison of case study measurements showing satellites, the satellite Magnetic Local Time, the ratio of the DMSP measurements, and the ratio of the ISR measurements for each pulse length.

Case Ratio	POLITE 4 F14 (09.56 MLT)/ F12 (10.40 MLT)	POLITE 7 F14 (20.55 MLT)/ F12 (20.43 MLT)	POLITE 10 F14 (20.77 MLT)/ F15 (21.38 MLT)
DMSP	0.6724	1.1182	1.3702
2000 μsec	1.2155	1.0948	1.0622
1000 μsec	1.1243	1.0875	1.0475

The POLITE 7 case shows consistency between the satellite and radar measurements. The F14 satellite crossed the terminator from dark to light during the overpass, and F12 approached the terminator, but did not cross within the five-degree circle. Both satellites measured a relatively undisturbed topside region and showed little variability between the two sensors. This is also reflected in the radar measurements.

The POLITE 10 case also had a consistent change between the two radar profiles, however the satellites were significantly different. A factor that could explain the discrepancy is that forty-five minutes separated the two satellites. The two times were sufficiently far apart that only two radar profiles (2000 μ sec pulse) overlapped. Also, the F15 DMSP crossed the site on a more easterly trajectory than the F14, so an east-west variation in the density could account for the difference.

The POLITE 4 case demonstrates clearly the ionosphere defies simple treatment. The ratio of the radar measurements is significantly different between the two pulse lengths, plus the satellites measurements trend in the opposite direction as the radar (i.e. the DMSP measurements increase while the ISR measurements decrease).

Looking at the DMSP measurements, M4-2 shows clear signs of both a LIT and a MT, while M4-3 shows indications of only a slight LIT. Also, there is a 15 km altitude separation between the two satellites and the two satellites pass through different sections of the five-degree latitude circle – F14 (M4-2) traversed west of the site and F12 (M4-3) passed to the east. Both pulse lengths of the ISR show considerable variability during the course of the overpass (about an order of magnitude) for M4-2 while for M4-3 they show less (factor of 2 – 3). All these indications suggest physical processes that require treatment beyond a simple comparison of two measurements.

Table 8: Comparison of the upper bound error propagation formula to the lower bound error propagation formula for selected Millstone Hill cases.

Pulse Length Case	2000 μsec	1000 μsec
M4-2	0.2936	0.4442
M4-3	0.2264	0.4077
M7-1	0.1038	0.1813
M7-2	0.0863	0.1658
M10-7	0.0351	0.0691
M10-8	0.0351	0.0727

This set of cases was also used to compare the two error propagation schemes (see section 3.2.1). Table 8 shows the relative difference of the two methods (upper bound minus lower bound) divided by the corrected electron density. Across the limited sample, the 2000 μ sec pulse length shows less relative difference than the 1000 μ sec, by

close to a factor of two. Also, the apparent solar cycle dependence of the DNEL/NEL ratio discussed earlier in this section seems to hold.

4.1.3 Sondrestrom Overpasses. The conjunctions with Sondrestrom were not nearly as straightforward as the long pulse lengths of Millstone Hill. Several reasons can account for this:

- 1) The shorter ISR pulse length measuring the ionosphere at 840 km,
- 2) The overpasses being in the auroral oval (with correspondingly short scale lengths and times for ionospheric events), and
- 3) The composition assumed when processing the ISR data.

The DMSP overpasses tended to show considerably more physical structure, causing us to restrict the overpass criteria to a one-degree circle. An example of this can be seen in Appendix B, Case S8-1. Figure 32 shows the DMSP and ISR measurements for Sondrestrom's seven conjunctions. Even with the DMSP traversing only two degrees, which worked out to six data points or less, the DMSP measurement varied considerably. Figure 33 shows the average DMSP σ / DMSP Avg was almost 14 percent.

The ISR data were similarly challenging. To maintain consistency with the short time scale of the DMSP overpass, only data available immediately before and after the conjunction were used. This restricted the available data to two radar returns at best, with only four of the seven conjunctions having good data on both. Consequently, just under half of the comparisons were made with only one radar profile. Again, the uncertainty in

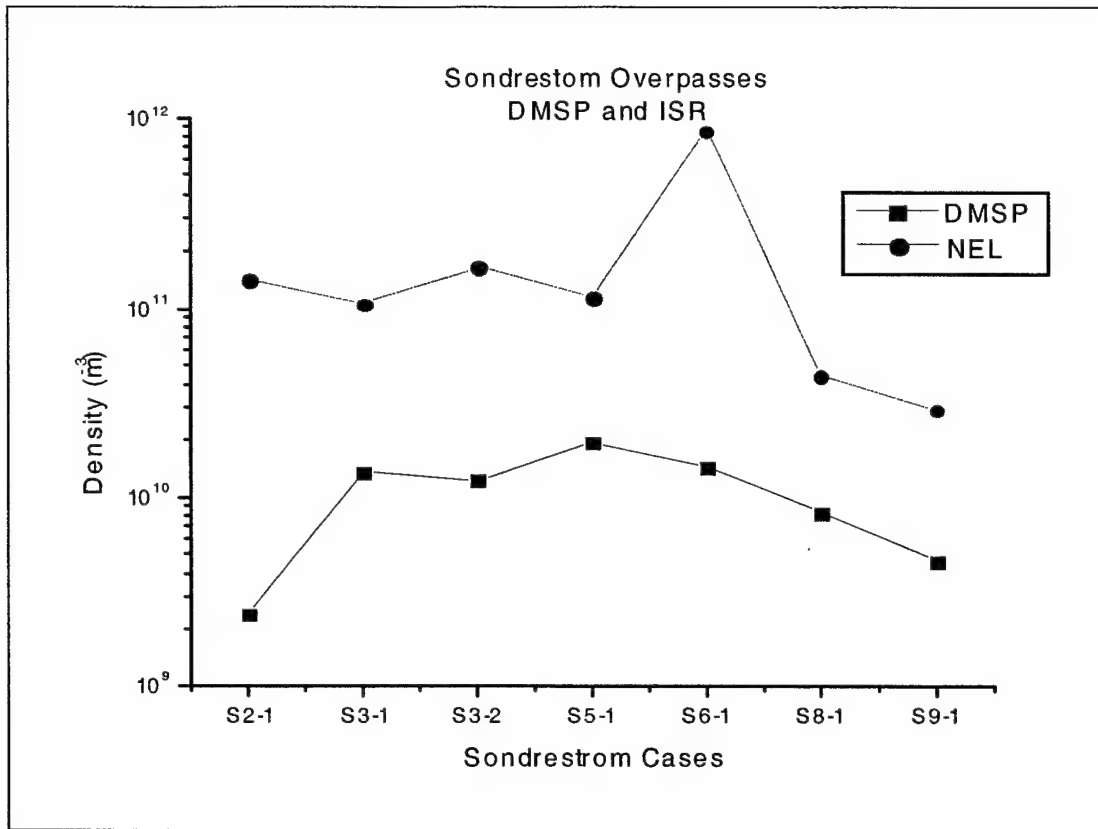


Figure 32: Sondrestrom conjunctions showing ISR and DMSP measurements

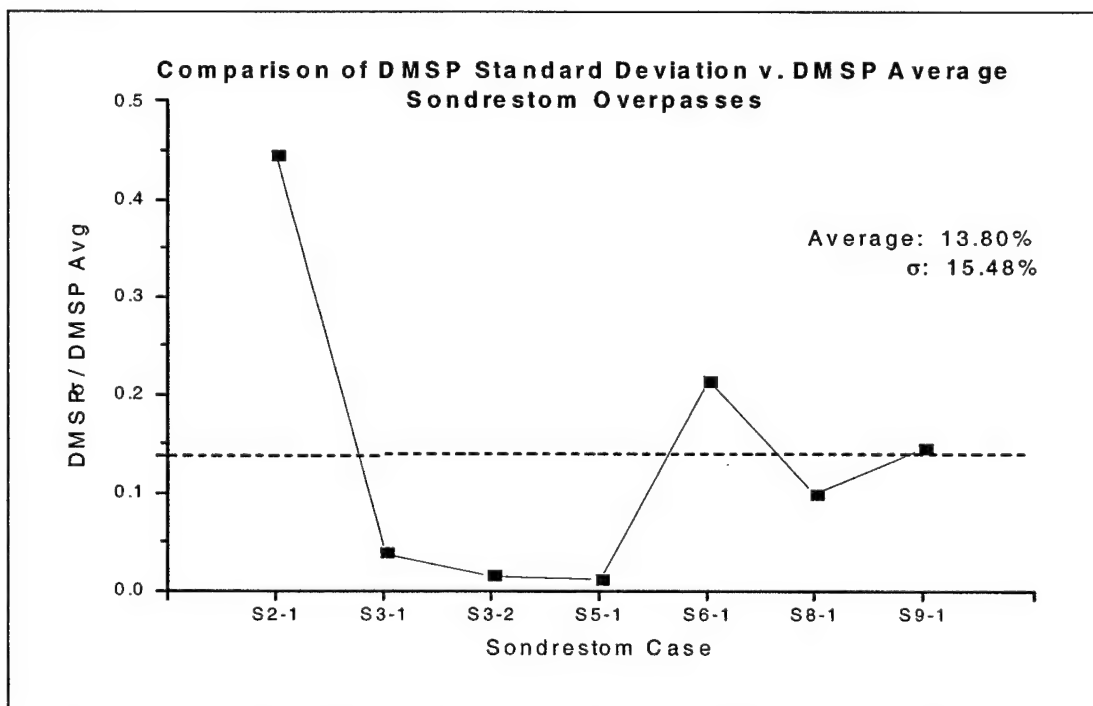


Figure 33: DMSP σ / DMSP Avg for Sondrestrom Overpasses.

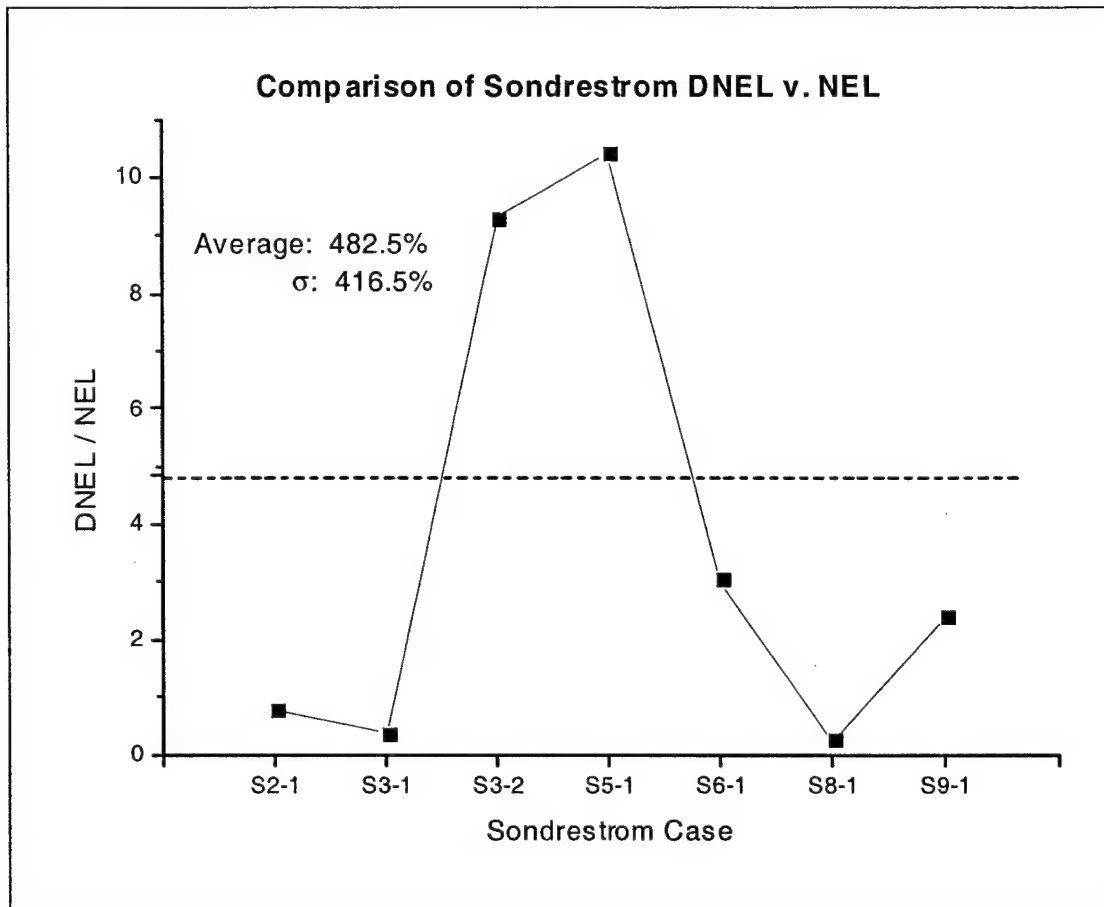


Figure 34: DNEL/NEL for Sondrestrom at 840 km.

the measurement was on the same order as the measurement; four of the seven cases have the uncertainty exceed the measurement. Figure 34 shows the ratio of the DNEL v. NEL for the overpasses.

Comparing the DMSP to the ISR at Sondrestrom resulted in large relative errors, due in part to the challenges outlined above. Equation (18) was used again and Figure 35 shows the results. While large, the relative errors were consistent around -90 percent. The DMSP measured lower than the Sondrestrom ISR anywhere from a factor of five to a factor of 60, an order of magnitude difference. While these numbers are large, they are within the uncertainty in the ISR measurements.

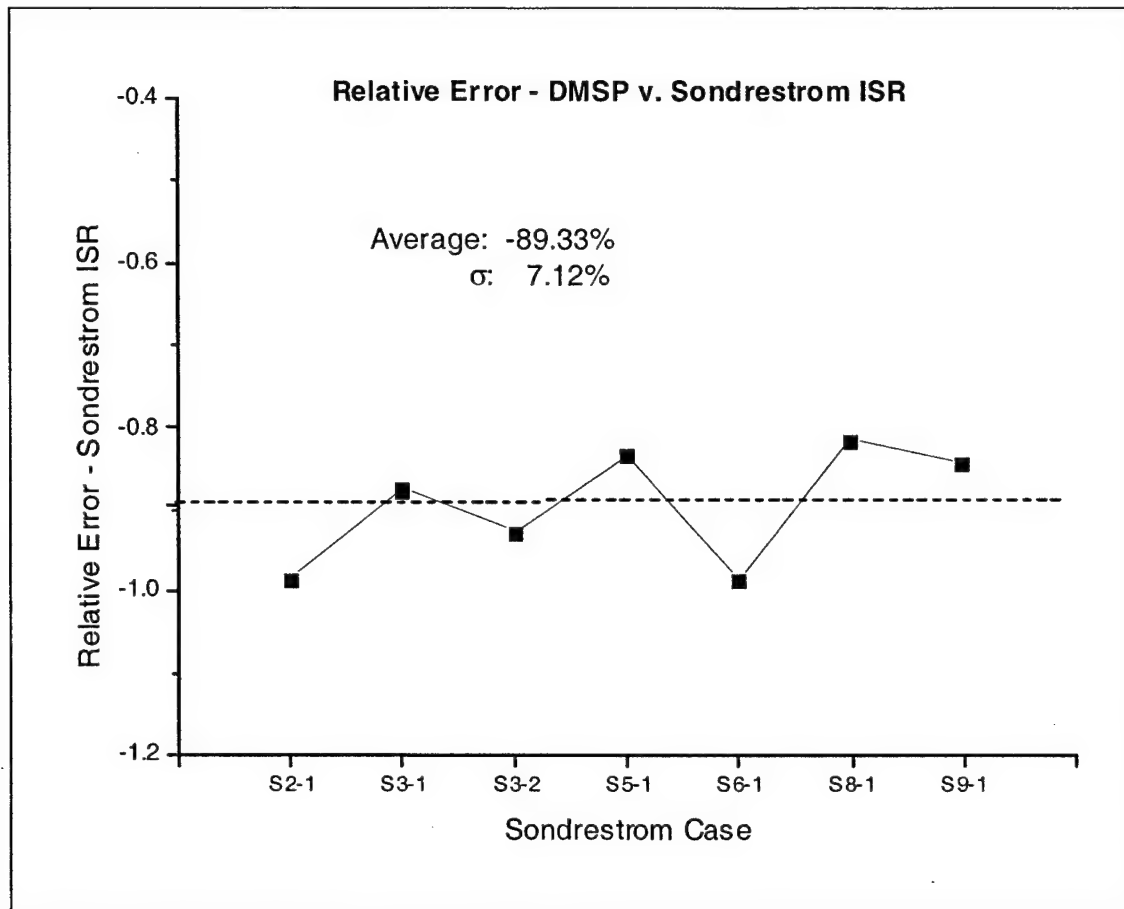


Figure 35: Relative error DMSP v. SON near 840 km.

4.2 Density Variations in the DMSP Measurements

The DMSP density measurements from the Millstone Hill overpasses were used to get a first look at the variability of the DMSP-measured ionospheric density. Most of these cases did not show highly variable structure, so a simple least-squares linear regression was used for a first-guess at de-trending the measurements. The Millstone Hill overpasses were interrogated using the Air Force Research Laboratory Auroral Boundary Index to see if any of the data fell within the auroral oval; none did. Since the data from over-passing Sondrestrom seemed to indicate a lot of physical structure, a simple linear regression would not have been appropriate and has been left for later study.

Not all of the Millstone Hill cases lent themselves to this treatment. Several cases were either too variable to be fit to the straight line, or fit too well and good data were discarded at the $2\sigma_r$ threshold. As shown in Figure 36, M9-1 is an example of this. In Figure 36a, the ionosphere shows physical structure that varies considerably (and only one point is outside the $2\sigma_r$ threshold). Removing the one point in Figure 36c does not improve the deviation of the de-trended residuals in Figure 36b and Figure 36d. In either case, it is obvious from the figure that the straight line is not appropriate.

Figure 37 demonstrates another case where legitimate data are removed. M2-2 shows where this procedure would throw out data that should be retained. The density values are relatively small and the variation from the straight line is minimal. With σ_r approximately 10 percent of the average value for this case, the $2\sigma_r$ threshold eliminates three data points that should be kept.

Figure 38 highlights the other problem with this method when the $2\sigma_r$ threshold is only applied once. In some cases, the algorithm should be run again to eliminate points that were missed. Cases M2-1 and M8-2 illustrate this. In M2-1, the obviously bad zero values fall outside the $2\sigma_r$ threshold, but the data immediately before and after should be removed as well, and are not. Similarly, three of the four outliers in M8-2 are removed, but one remains to skew the rest of the data.

A large number of the other cases that had data filtered out came from the end of the time series. This was the result of the satellite either entering or leaving a region of the ionosphere dominated by differing physical processes, for example a MT or LIT. This was not considered a problem since the straight line modeled the remainder of the

overpass fairly well. Eight of the cases had no data filtered out. The cases are enumerated in Table 9. The quantity σ_r / Avg is useful in characterizing the amount of error relative to the size of the measurement. For these cases, this parameter averaged less than three percent, with a standard deviation of 5.3 percent. The footnotes bring to light the cases where the routine used fell short, and excluding the cases with footnotes, the average and standard deviation of σ_r / Avg goes to 2.1 percent and 4.3 percent.

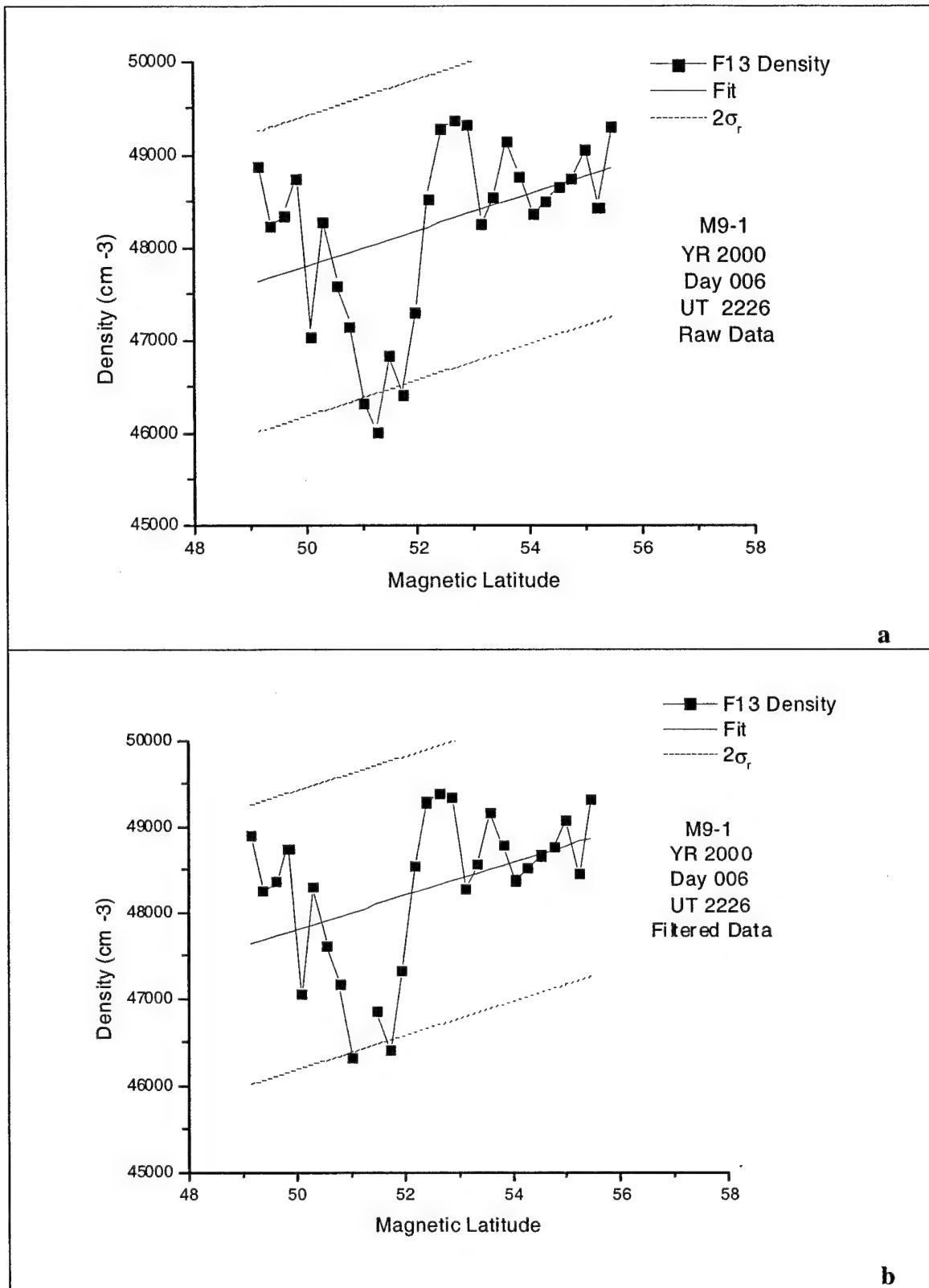


Figure 36: M9-1 shows too much physical structure for a linear fit. The two points in (a) near the lower limit plot are within $2\sigma_r$.

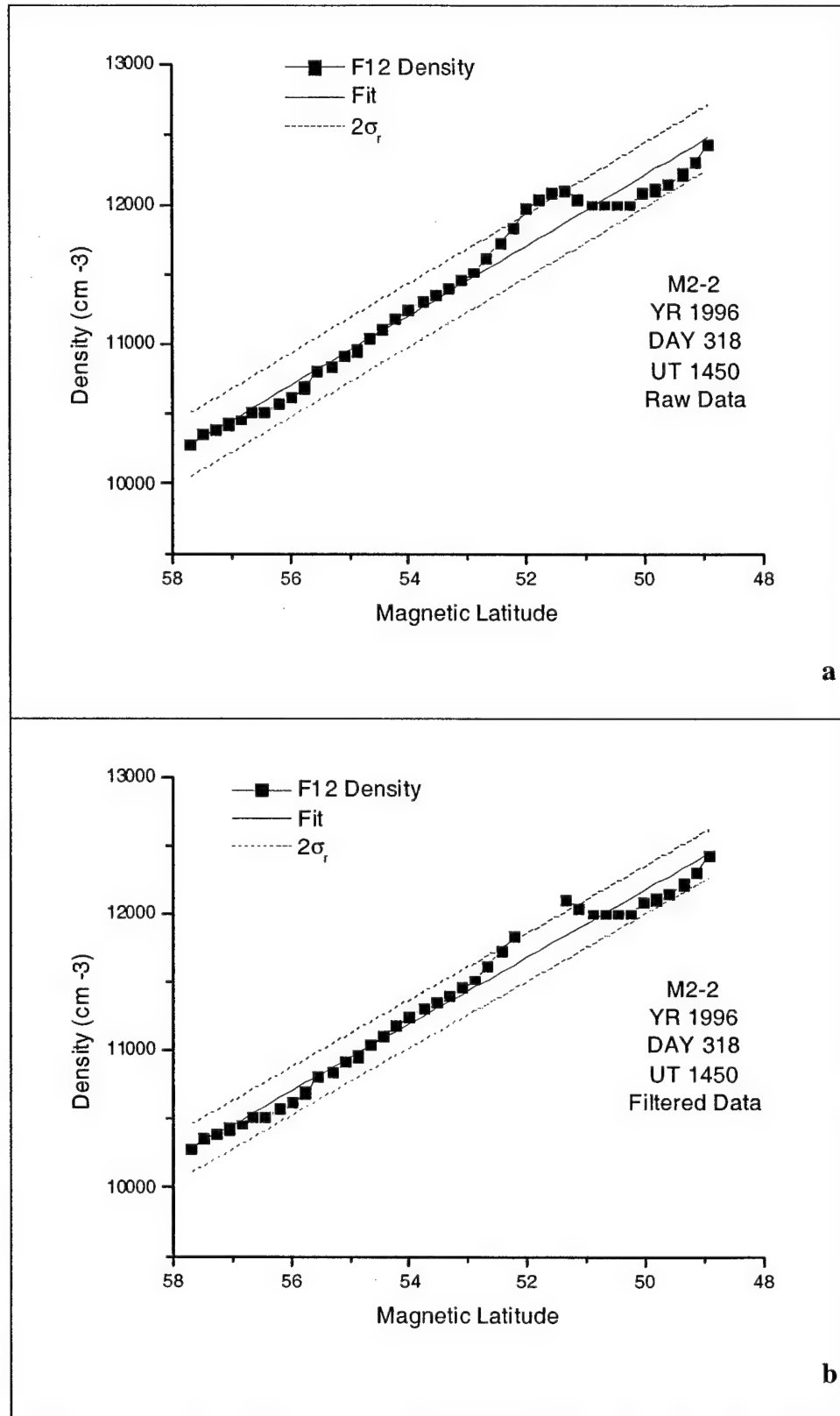


Figure 37: M2-2 shows linear fit removing good data.

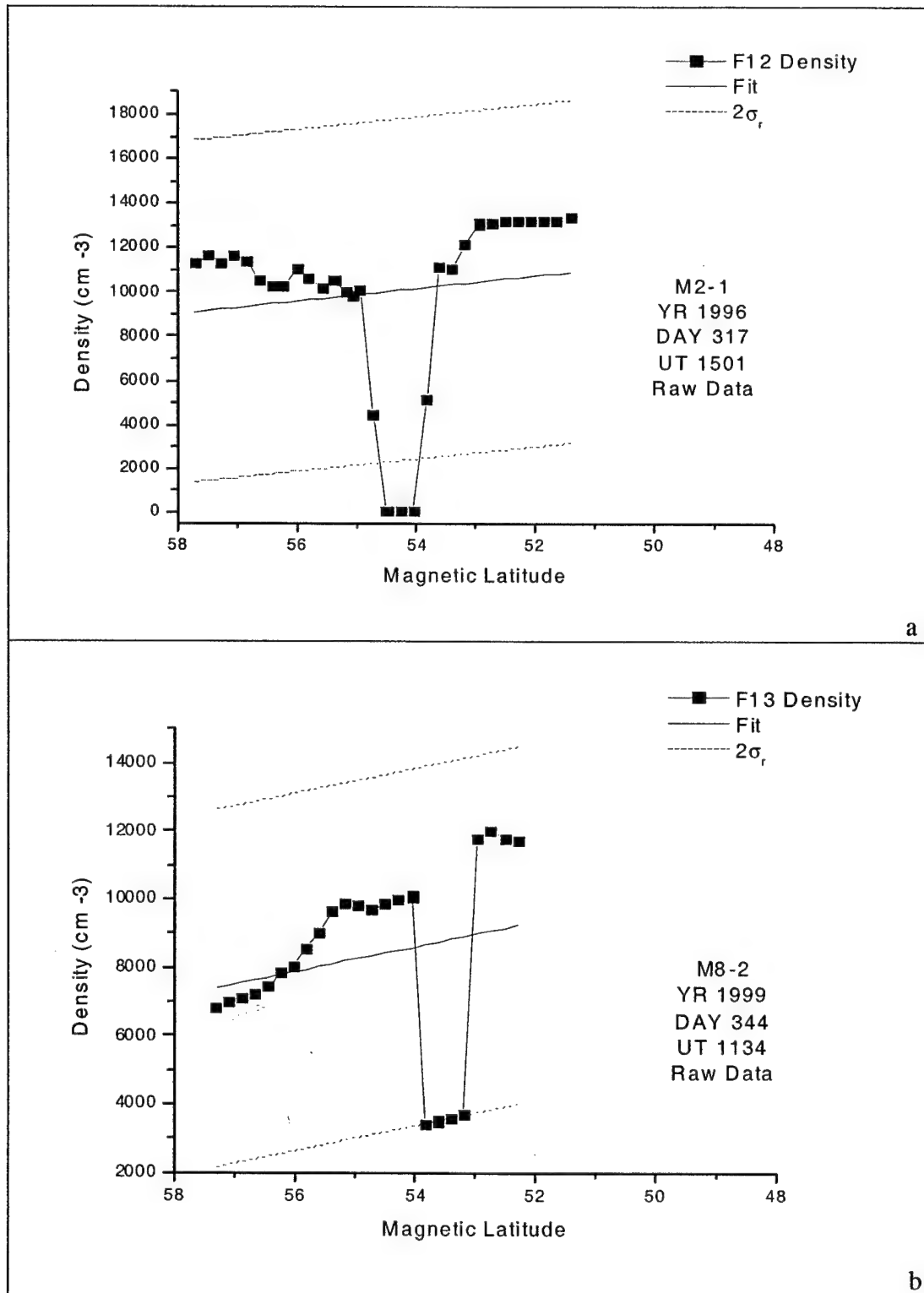


Figure 38: Examples requiring another application of filtering algorithm.

Table 9: DMSP Density Variability

Case	Filtered Average 10^4 cm^{-3}	σ Residual	σ_r / Avg	Case	Filtered Average 10^4 cm^{-3}	σ Residual	σ_r / Avg
M1-1	0.341	976	0.218	M6-1	1.329	71.3	0.005
M1-2 ⁴	0.332	284	0.085	M6-2	0.823	313	0.038
M2-1 ³	1.108	2000	0.181	M6-3 ²	2.588	250	0.010
M2-2	1.133	87.6	0.008	M7-1	3.330	3060	0.092
M2-3	1.345	79.7	0.006	M7-2 ²	2.973	274	0.009
M3-1	1.594	58.2	0.004	M7-3	2.052	101	0.005
M3-2	1.307	158	0.012	M8-1	1.471	306	0.021
M3-3 ²	1.229	145	0.012	M8-2 ³	0.899	1640	0.182
M3-4	2.479	98.8	0.004	M8-3 ¹	3.562	0.057	0.000
M3-5	1.443	213	0.015	M9-1 ²	4.828	809	0.017
M4-1	0.631	255	0.040	M10-1	7.016	356	0.005
M4-2	1.697	162	0.010	M10-2	5.110	206	0.004
M4-3	1.138	137	0.012	M10-3	7.277	340	0.005
M4-4	0.794	83.3	0.011	M10-4 ²	9.413	1078	0.011
M4-5 ⁴	1.018	90.5	0.009	M10-5	6.324	133	0.002
M5-1	2.008	342	0.017	M10-6	8.275	190	0.002
M5-2	1.394	85.0	0.006	M10-7	10.614	410	0.004
M5-3	3.110	130	0.004	M10-8	7.336	751	0.010
M5-4	2.771	483	0.017				

NOTES: ¹Data constant for overpass. ³Outliers still present
²Linear fit not good approximation. ⁴ $2\sigma_r$ threshold too small

V. Conclusions and Recommendations

5.1 Conclusions

In all cases studied, the DMSP SSIES instruments recorded a lower value of plasma density values on average than either the Millstone Hill or Sondrestrom Incoherent Scatter Radars. A difference was not unexpected, since the uncertainty of the ISR at these altitudes was found to be on the order of the size of the measurement, and a factor of two was not uncommon. The apparent bias was unexpected.

The relative error of the DMSP was negative 20 - 22 percent when compared to the measured Millstone Hill ISR values, and ranged from ~ -10 to -15 percent for the fit data. Both of these values exceed the published value of 10 percent (Rich, 1994) and at first blush, seem to disagree with Sultan and Rich (2000), whose research did not reveal such a bias. However the same parameters were not used when selecting cases for this research, and larger relative errors were expected. The Sultan and Rich (2000) study used only "good" ISR measurements at mid-latitudes during solar max, which lends itself to an ISR profile with less uncertainty. Our research also included an analysis of the uncertainty of the ISR, so less restrictive selection criteria were needed. The fit data compared better than the measured data because the entire profile was incorporated into modeling the fit. The relative error of the fit profiles approached the advertised value.

The Sondrestrom ISR measurements were significantly different than the DMSP's, averaging almost -90 percent relative error. Again, this range of the difference was not a surprise, however the bias was still unexpected. The auroral oval and polar cap have temporal and spatial characteristics that cannot be resolved by the ISR, especially at

DMSP altitudes where the ISR is forced to integrate over a 10-minute period. Even so, the DMSP measurement was within the uncertainty of the radar. All in all, this study does not contradict Sultan and Rich (2000) about the relative error of the DMSP measurements, but finds that the DMSP measures the same density as the ISRs within the radars' uncertainty. Also as shown in Figure 35, to a first approximation, the slope of the trend of the relative errors is positive, indicating a slight improvement in the relative error as the solar cycle approached solar max. Again, the bias has not been characterized previously.

The near-simultaneous Millstone Hill overpass cases explored two areas. First was the lower bound error propagation equation. This method did yield significantly smaller uncertainties in the Millstone Hill data. Even with that being the case, the DMSP still measured the density within the smaller ISR uncertainty in the cases examined. Second, SSIES instrument packages from two different satellites were compared. In the quiescent ionosphere of POLITE 7, the SSIES measured the same relative changes as the Millstone Hill ISR, but in the more active periods the SSIES-measured changes did not correspond to the ISR-measured changes. Further study is needed to determine whether this difference is instrumental or the separate satellites measured changes caused by local ionospheric structure and dynamics.

The variability study gives a first approximation of the DMSP measurement variations in mid-latitudes. For now, the variability can be interpreted as physical processes in the ionosphere that may be on a scale too small to model effectively and have to be included in the Kalman filter as noise. Because the SSIES data were averaged

24 times per second for four seconds, no real estimation of instrument noise was made since the data are too smooth for a true random noise approximation.

Given the smoothness of the DMSP data, these conclusions might be extended to equatorial latitudes with little trepidation. While small-scale features may be encountered there, except for equatorial instabilities, they will generally not exceed the amount encountered in the mid-latitude cases in this study. The auroral oval and polar cap regions need a more rigorous treatment to characterize the SSIES variability in those regions. A least-squares linear fit by no means can approximate the structure and dynamics involved poleward of the auroral boundary.

5.2 Recommendations

Further validation of the data are recommended in the polar cap and auroral oval regions; however comparing the DMSP to ground-based instrumentation will generate the same problems encountered here. Comparisons between DMSP and other *in situ* instrumentation will need to be performed to arrive at data sets that are not preordained to be overwhelmed by the uncertainties in the measurements. Another possible course of action to reduce uncertainty in the ISR profiles is to re-process the Millstone Hill data into 10-minute integration files. Since two studies (Sultan and Rich, 2000, and this one) have explicitly compared the DMSP to the Millstone Hill ISR and concluded that the difference of the measurements are within the error, this step is probably not worth the time and effort. The unexplained bias encountered here suggests further collaboration between AFRL, UTD, Millstone Hill, and Sondrestrom.

The data set collected for this thesis still has a wealth of untouched information. This and the companion electron temperature work can be extended to ion velocity, temperature, and composition with little new effort.

ISR data from Arecibo and Jicamarca for the POLITE periods could extend these results into the equatorial region, and EISCAT data could expand the comparison into the auroral oval/polar cap. This would also serve to collect the POLITE campaign data into one repository.

The characterization of the entire set of 1147 orbits of DMSP SSIES density measurements is the logical next step. This would provide a global picture of the density variations and an estimate of the typical instrument noise associated with all phases of the rising solar cycle. Once this methodology is in place, other parameters as mentioned above can be categorized with alacrity.

Since the DMSP will soon fall under NOAA auspices, an effort should be made to continue equipping the NPOES with SSIES-like instruments, and ensure real-time telemetry of the information is made a reality. The state of the science is at the point where the continuous monitoring of the topside ionosphere -- and assimilation of that data into physics-based models -- will greatly enhance the community's ability to model and forecast space weather and geomagnetic events. This will have a positive impact not only the Air Force and DoD mission, but also commercial enterprises.

Appendix A: Millstone Hill Comparison

The following pages contain the numerical data used for the comparison of the Millstone Hill ISR measurements to the DMSP SSIES density measurements. Each page contains one conjunction's data and is titled using the naming convention from Section 3.

Included are:

1. DMSP satellite number
2. ↑ if the satellite is in an ascending node and ↓ if in a descending node
(This element will have a dark background if the satellite is eclipsed)
3. Kp index
4. F10.7 solar flux
5. DMSP average and standard deviation (cm^3)
6. Number of DMSP data points within the five-degree circle
7. DMSP magnetic local time
8. Measured Millstone Hill average NEL and DNEL for each pulse (m^3)
9. Fit Millstone Hill NEL at DMSP altitude for each pulse
10. Fit Millstone Hill average and standard deviation for each pulse within
 ± 25 km of DMSP altitude

For the overpasses involved in the case studies, an additional table contains the results from the lower bound error propagation equation for DNEL (see equation (14)).

Items 8 – 10 from the above list reflect the modified DNEL results.

The supplemental data section includes the tables, plus a plot of all the data used. It is available upon request from the author, the advisor, or the Engineering Physics Department at the Air Force Institute of Technology.

M1-1
96 045 01.758

Table 10: Case M1-1

F12	↑	Kp	4.3	F10.7	67.2
DMSP Avg	3.484E+03	DMSP σ	1188	# DMSP Pts	41
MLT	20.62	Fit			
	Measured Avg		2000	1000	410
2000 NEL 845 km	9.855E+09	@ DMSP Alt	9.179E+09	****	****
DNEL	1.002E+10	± 25 km Avg	9.181E+09	****	****
1000 NEL 874 km	****	σ	3.265E+07	****	****
DNEL	****				

M1-2
96 045 10.820

Table 11: Case M1-2

F13	↓	Kp	3.3	F10.7	67.2
DMSP Avg	3.404E+03	DMSP σ	1049	# DMSP Pts	29
MLT	6.46	Fit			
	Measured Avg		2000	1000	410
2000 NEL 845 km	1.219E+10	@ DMSP Alt	5.693E+09	****	3.469E+09
DNEL	1.497E+10	± 25 km Avg	5.697E+09	****	3.470E+09
1000 NEL 874 km	****	σ	1.034E+08	****	2.230E+07
DNEL	****				

M2-1
96 317 15.033

Table 12: Case M2-1

F12	↓	Kp	1.0	F10.7	70.7
DMSP Avg	1.000E+04	DMSP σ	3901	# DMSP Pts	31
MLT	10.48	Fit			
	Measured Avg		2000	1000	410
2000 NEL 844 km	1.379E+10	@ DMSP Alt	1.226E+10	9.593E+09	8.627E+09
DNEL	1.424E+11	± 25 km Avg	1.233E+10	9.596E+09	8.680E+09
1000 NEL 874 km	1.053E+10	σ	1.362E+09	3.016E+07	1.128E+08
DNEL	1.303E+10				

M2-2
96 318 14.840

Table 13: Case M2-2

F12	↓	Kp	2.0	F10.7	70.7
DMSP Avg	1.138E+04	DMSP σ	670	# DMSP Pts	41
MLT	10.49	Fit			
	Measured Avg		2000	1000	410
2000 NEL 844 km	7.692E+09	@ DMSP Alt	8.027E+09	1.002E+10	2.006E+10
DNEL	6.679E+09	± 25 km Avg	8.034E+09	1.002E+10	2.006E+10
1000 NEL 874 km	1.205E+10	σ	1.915E+08	1.668E+08	2.645E+07
DNEL	1.588E+10				

M2-3
96 319 14.639

Table 14: Case M2-3

F12	↓	Kp	1.8	F10.7	72.1
DMSP Avg	1.343E+04	DMSP σ	337	# DMSP Pts	36
MLT	10.56	Fit			
	Measured Avg		2000	1000	410
2000 NEL 844 km	1.119E+10	@ DMSP Alt	1.046E+10	1.260E+10	1.229E+10
DNEL	8.832E+09	± 25 km Avg	1.047E+10	1.260E+10	1.229E+10
1000 NEL 874 km	1.292E+10	σ	4.521E+07	9.689E+06	2.080E+07
DNEL	1.285E+10				

M3-1
97 154 14.461

Table 15: Case M3-1

F12	↓	Kp	1.7	F10.7	77.4
DMSP Avg	1.600E+04	DMSP σ	565	# DMSP Pts	18
MLT	10.16	Fit			
	Measured Avg		2000	1000	410
2000 NEL 844 km	2.334E+10	@ DMSP Alt	2.129E+10	1.863E+10	1.193E+10
DNEL	1.765E+10	± 25 km Avg	2.124E+10	1.865E+10	1.195E+10
1000 NEL 874 km	2.414E+10	σ	8.983E+08	5.349E+08	7.246E+10
DNEL	2.697E+10				

M3-2
97 155 01.906

Table 16: Case M3-2

F12	↑	Kp	2.0	F10.7	76.1
DMSP Avg	1.307E+04	DMSP σ	396	# DMSP Pts	16
MLT	21.52	Fit			
	Measured Avg		2000	1000	410
2000 NEL 844 km	2.197E+10	@ DMSP Alt	1.671E+10	2.227E+10	1.054E+10
DNEL	2.104E+10	± 25 km Avg	1.674E+10	2.278E+10	1.057E+10
1000 NEL 874 km	3.436E+10	σ	1.032E+09	4.986E+07	7.330E+08
DNEL	4.311E+10				

M3-4
97 155 22.298

Table 17: Case M3-4

F13	↑	Kp	1.0	F10.7	76.1
DMSP Avg	2.479E+04	DMSP σ	324	# DMSP Pts	22
MLT	17.70	Fit			
	Measured Avg		2000	1000	410
2000 NEL 844 km	1.801E+11	@ DMSP Alt	3.608E+10	3.411E+10	4.036E+10
DNEL	2.664E+11	± 25 km Avg	3.612E+10	3.414E+10	4.039E+10
1000 NEL 877 km	4.247E+10	σ	1.459E+09	1.113E+09	4.653E+08
DNEL	3.398E+10				

M3-5
97 156 01.713

Table 18: Case M3-5

F12	↑	Kp	1.0	F10.7	76.1
DMSP Avg	1.447E+04	DMSP σ	972	# DMSP Pts	39
MLT	21.60	Fit			
	Measured Avg		2000	1000	410
2000 NEL 844 km	2.422E+10	@ DMSP Alt	3.812E+10	2.467E+10	2.180E+10
DNEL	2.064E+10	± 25 km Avg	3.812E+10	2.469E+10	2.183E+10
1000 NEL 874 km	3.240E+10	σ	8.221E+07	3.455E+08	3.422E+08
DNEL	3.329E+10				

M4-1
97 337 11.077

Table 19: Case M4-1

F13	↓	Kp	1.3	F10.7	109.0
DMSP Avg	6.546E+03	DMSP σ	1354	# DMSP Pts	40
MLT	7.00	Fit			
	Measured Avg		2000	1000	410
2000 NEL 844 km	1.000E+10	@ DMSP Alt	1.083E+10	1.330E+10	2.276E+10
DNEL	1.789E+10	± 25 km Avg	1.041E+10	1.330E+10	2.277E+10
1000 NEL 874 km	2.021E+10	σ	7.580E+07	6.080E+06	9.506E+07
DNEL	3.607E+11				

M4-2
97 337 14.023

Table 20: Case M4-2

F14	↓	Kp	2.0	F10.7	109.0
DMSP Avg	1.141E+04	DMSP σ	480	# DMSP Pts	39
MLT	9.56	Fit			
	Measured Avg		2000	1000	410
2000 NEL 844 km	1.799E+10	@ DMSP Alt	1.506E+10	1.231E+10	2.261E+10
DNEL	1.516E+10	± 25 km Avg	1.508E+10	1.232E+10	2.262E+10
1000 NEL 874 km	2.143E+10	σ	1.841E+08	1.872E+08	1.657E+08
DNEL	2.604E+10				

Modified Error

Table 21: Case M4-2 Modified Error

	Measured Avg		2000	1000	410
2000 NEL 844 km	1.799E+10	@ DMSP Alt	1.506E+10	9.938E+09	1.655E+10
DNEL	9.879E+09	± 25 km Avg	1.508E+10	9.404E+09	1.657E+10
1000 NEL 874 km	2.143E+10	σ	1.920E+08	4.435E+08	1.365E+08
DNEL	1.652E+10				

M4-3
97 337 14.396

Table 22: Case M4-3

F12	↓	Kp	2.0	F10.7	109.0
DMSP Avg	1.697E+04	DMSP σ	526	# DMSP Pts	26
MLT	10.40	Fit			
	Measured Avg		2000	1000	410
2000 NEL 844 km	1.480E+10	@ DMSP Alt	1.589E+10	1.430E+10	1.855E+10
DNEL	1.080E+10	± 25 km Avg	1.591E+10	1.432E+10	1.857E+10
1000 NEL 874 km	1.906E+10	σ	5.188E+08	5.306E+08	6.094E+08
DNEL	2.049E+10				

Modified Error

Table 23: Case M4-3 Modified Error

	Measured Avg		2000	1000	410
2000 NEL 844 km	1.480E+10	@ DMSP Alt	2.089E+10	1.334E+10	2.483E+10
DNEL	7.449E+09	± 25 km Avg	2.705E+10	1.335E+10	2.485E+10
1000 NEL 874 km	1.906E+10	σ	2.450E+09	4.608E+07	2.042E+08
DNEL	1.272E+10				

M4-4
97 338 10.869

Table 24: Case M4-4

F13	↓	Kp	1.3	F10.7	104.2
DMSP Avg	8.012E+03	DMSP σ	1038	# DMSP Pts	26
MLT	7.09	Fit			
	Measured Avg		2000	1000	410
2000 NEL 844 km	****	@ DMSP Alt	****	1.218E+10	1.717E+10
DNEL	****	± 25 km Avg	****	1.218E+10	1.730E+10
1000 NEL 874 km	2.937E+10	σ	****	6.293E+06	3.371E+10
DNEL	2.937E+10				

M4-5
97 338 13.819

Table 25: Case M4-5

F14	↓	Kp	1.3	F10.7	104.2
DMSP Avg	9.942E+03	DMSP σ	1806	# DMSP Pts	38
MLT	9.62	Fit			
	Measured Avg		2000	1000	410
2000 NEL 844 km	1.426E+10	@ DMSP Alt	1.274E+10	1.398E+10	9.736E+09
DNEL	1.412E+10	± 25 km Avg	1.275E+10	1.399E+10	9.271E+09
1000 NEL 874 km	1.983E+10	σ	1.737E+08	1.741E+07	3.592E+08
DNEL	3.990E+10				

M5-1
98 147 00.928

Table 26: Case M5-1

F14	↑	Kp	2.0	F10.7	96.6
DMSP Avg	2.008E+04	DMSP σ	1061	# DMSP Pts	39
MLT	20.81	Fit			
	Measured Avg		2000	1000	410
2000 NEL 844 km	2.336E+10	@ DMSP Alt	2.154E+10	2.415E+10	1.973E+10
DNEL	8.883E+09	\pm 25 km Avg	2.162E+10	2.421E+10	1.977E+10
1000 NEL 874 km	2.474E+10	σ	1.417E+09	4.088E+09	1.007E+09
DNEL	1.403E+10				

M5-2
98 147 10.912

Table 27: Case M5-2

F13	↓	Kp	1.7	F10.7	96.6
DMSP Avg	1.392E+04	DMSP σ	148	# DMSP Pts	27
MLT	6.45	Fit			
	Measured Avg		2000	1000	410
2000 NEL 844 km	1.495E+10	@ DMSP Alt	1.381E+10	1.324E+10	1.536E+10
DNEL	8.586E+09	\pm 25 km Avg	1.384E+10	1.326E+10	1.558E+10
1000 NEL 874 km	1.668E+10	σ	5.231E+08	6.328E+08	5.990E+08
DNEL	1.384E+10				

M5-3
98 147 22.352

Table 28: Case M5-3

F13	↑	Kp	2.0	F10.7	96.6
DMSP Avg	3.108E+04	DMSP σ	363	# DMSP Pts	23
MLT	17.76	Fit			
	Measured Avg		2000	1000	410
2000 NEL 844 km	3.183E+10	@ DMSP Alt	3.158E+10	3.079E+10	3.508E+10
DNEL	1.062E+10	± 25 km Avg	3.163E+10	3.085E+10	3.512E+10
1000 NEL 874 km	3.118E+10	σ	1.565E+09	1.426E+09	1.055E+09
DNEL	1.663E+10				

M5-4
98 148 00.722

Table 29: Case M5-4

F14	↑	Kp	0.7	F10.7	101.1
DMSP Avg	2.771E+04	DMSP σ	1522	# DMSP Pts	34
MLT	20.89	Fit			
	Measured Avg		2000	1000	410
2000 NEL 844 km	3.430E+10	@ DMSP Alt	3.112E+10	3.807E+10	2.265E+10
DNEL	1.127E+10	± 25 km Avg	3.123E+10	2.815E+10	2.270E+10
1000 NEL 874 km	2.928E+10	σ	1.800E+09	1.300E+09	1.083E+09
DNEL	1.441E+10				

M6-1
98 327 00.647

Table 30: Case M6-1

F14	↑	Kp	2.7	F10.7	126.7
DMSP Avg	1.327E+04	DMSP σ	141	# DMSP Pts	11
MLT	20.59	Fit			
	Measured Avg		2000	1000	410
2000 NEL 844 km	1.580E+10	@ DMSP Alt	1.565E+10	1.781E+10	1.318E+10
DNEL	1.237E+10	± 25 km Avg	1.569E+10	1.784E+10	1.335E+10
1000 NEL 874 km	2.305E+10	σ	5.609E+08	4.577E+08	4.829E+08
DNEL	2.335E+10				

M6-2
98 327 11.262

Table 31: Case M6-2

F13	↓	Kp	2.0	F10.7	126.7
DMSP Avg	8.235E+03	DMSP σ	1964	# DMSP Pts	40
MLT	7.08	Fit			
	Measured Avg		2000	1000	410
2000 NEL 844 km	****	@ DMSP Alt	7.518E+09	1.218E+10	1.185E+10
DNEL	****	± 25 km Avg	7.537E+09	1.219E+10	1.180E+10
1000 NEL 874 km	****	σ	2.005E+08	8.955E+07	1.913E+08
DNEL	****				

M6-3
98 327 14.252

Table 32: Case M6-3

F12	↓	Kp	3.0	F10.7	126.7
DMSP Avg	2.587E+04	DMSP σ	292	# DMSP Pts	37
MLT	10.15	Fit			
	Measured Avg		2000	1000	410
2000 NEL 844 km	2.801E+10	@ DMSP Alt	2.961E+10	2.465E+10	3.317E+10
DNEL	1.261E+10	± 25 km Avg	2.967E+10	2.411E+10	3.321E+10
1000 NEL 874 km	2.277E+10	σ	1.568E+09	1.298E+09	9.197E+08
DNEL	1.386E+10				

M7-1
99 282 01.002

Table 33: Case M7-1

F14	↑*	Kp	0.7	F10.7	152.8
DMSP Avg	3.330E+04	DMSP σ	5890	# DMSP Pts	41
MLT	20.55	Fit			
	Measured Avg		2000	1000	410
2000 NEL 844 km	4.378E+10	@ DMSP Alt	4.055E+10	3.752E+10	2.760E+10
DNEL	1.641E+10	± 25 km Avg	4.067E+10	3.759E+10	2.767E+10
1000 NEL 874 km	3.976E+10	σ	2.433E+09	1.571E+09	1.445E+09
DNEL	2.369E+10				

* Satellite Crosses Terminator

Modified Error

Table 34: Case M7-1 Modified Error

	Measured Avg		2000	1000	410
2000 NEL 844 km	4.378E+10	@ DMSP Alt	3.276E+10	3.571E+10	3.167E+10
DNEL	1.284E+10	± 25 km Avg	3.320E+10	3.580E+10	3.173E+10
1000 NEL 874 km	3.976E+10	σ	1.240E+09	1.645E+09	1.341E+09
DNEL	1.648E+10				

M7-2
99 282 01.244

Table 35: Case M7-2

F12	↑	Kp	0.7	F10.7	152.8
DMSP Avg	2.978E+04	DMSP σ	359	# DMSP Pts	27
MLT	20.43	Fit			
	Measured Avg		2000	1000	410
2000 NEL 844 km	3.999E+10	@ DMSP Alt	3.938E+10	3.377E+10	2.802E+10
DNEL	1.551E+10	± 25 km Avg	3.949E+10	3.386E+10	2.808E+10
1000 NEL 874 km	3.656E+10	σ	2.394E+09	1.277E+09	2.526E+09
DNEL	2.072E+10				

Modified Error

Table 36: Case M7-2 Modified Error

	Measured Avg		2000	1000	410
2000 NEL 844 km	3.999E+10	@ DMSP Alt	3.865E+10	3.390E+10	2.750E+10
DNEL	1.206E+10	± 25 km Avg	3.869E+10	3.397E+10	2.757E+10
1000 NEL 874 km	3.656E+10	σ	1.789E+09	1.338E+09	8.860E+08
DNEL	1.466E+10				

M7-3
99 282 11.017

Table 37: Case M7-3

F13	↓	Kp	1.0	F10.7	152.8
DMSP Avg	2.053E+04	DMSP σ	426	# DMSP Pts	24
MLT	12.79	Fit			
	Measured Avg		2000	1000	410
2000 NEL 844 km	2.243E+10	@ DMSP Alt	2.411E+10	2.158E+10	2.749E+10
DNEL	1.269E+10	± 25 km Avg	2.514E+10	2.162E+10	2.752E+10
1000 NEL 874 km	2.455E+10	σ	5.550E+08	6.917E+08	8.647E+08
DNEL	2.403E+10				

M8-1
99 344 01.346

Table 38: Case M8-1

F14	↑	Kp	2.0	F10.7	159.5
DMSP Avg	1.466E+04	DMSP σ	805	# DMSP Pts	15
MLT	20.18	Fit			
	Measured Avg		2000	1000	410
2000 NEL 844 km	2.523E+10	@ DMSP Alt	1.958E+10	2.351E+10	1.574E+10
DNEL	1.901E+10	± 25 km Avg	1.963E+10	2.359E+10	1.575E+10
1000 NEL 874 km	3.275E+10	σ	9.000E+08	7.525E+08	1.033E+07
DNEL	2.513E+10				

M8-2
99 344 11.581

Table 39: Case M8-2

F13	↓	Kp	1.3	F10.7	159.5
DMSP Avg	8.305E+03	DMSP σ	2682	# DMSP Pts	24
MLT	7.09	Fit			
	Measured Avg		2000	1000	410
2000 NEL 844 km	****	@ DMSP Alt	1.741E+10	2.913E+10	4.760E+09
DNEL	****	\pm 25 km Avg	1.793E+10	2.913E+10	4.778E+09
1000 NEL 874 km	2.546E+10	σ	3.043E+08	7.297E+08	3.162E+08
DNEL	2.514E+10				

M8-3
99 344 14.088

Table 40: Case M8-3

F12	↓	Kp	2.0	F10.7	159.8
DMSP Avg	3.562E+04	DMSP σ	0	# DMSP Pts	22
MLT	9.57	Fit			
	Measured Avg		2000	1000	410
2000 NEL 844 km	8.135E+10	@ DMSP Alt	3.080E+10	3.826E+10	4.958E+10
DNEL	4.264E+10	\pm 25 km Avg	3.089E+10	3.828E+10	4.964E+10
1000 NEL 874 km	3.751E+10	σ	1.963E+09	9.191E+08	1.188E+09
DNEL	2.454E+10				

M9-1
00 006 22.444

Table 41: Case M9-1

F13	↑	Kp	3.3	F10.7	140.0
DMSP Avg	4.820E+04	DMSP σ	976	# DMSP Pts	28
MLT	17.52	Fit			
	Measured Avg		2000	1000	410
2000 NEL 844 km	6.765E+10	@ DMSP Alt	5.475E+10	4.691E+10	5.643E+10
DNEL	3.244E+10	± 25 km Avg	5.493E+10	4.704E+10	5.650E+10
1000 NEL 874 km	7.145E+10	σ	3.563E+09	2.945E+09	4.915E+08
DNEL	4.163E+10				

M10-1
00 183 13.825

Table 42: Case M10-1

F14	↓	Kp	1.0	F10.7	169.2
DMSP Avg	6.998E+04	DMSP σ	883	# DMSP Pts	29
MLT	9.27	Fit			
	Measured Avg		2000	1000	410
2000 NEL 844 km	6.751E+10	@ DMSP Alt	5.878E+10	6.144E+10	3.122E+10
DNEL	2.178E+10	± 25 km Avg	5.890E+10	6.155E+10	3.132E+10
1000 NEL 874 km	6.135E+10	σ	3.232E+09	2.236E+09	2.614E+09
DNEL	3.210E+10				

M10-2
00 183 14.600

Table 43: Case M10-2

F15	↓	Kp	1.0	F10.7	169.2
DMSP Avg	5.109E+04	DMSP σ	766	# DMSP Pts	39
MLT	9.91	Fit			
	Measured Avg		2000	1000	410
2000 NEL 844 km	6.045E+10	@ DMSP Alt	5.790E+10	5.750E+10	3.151E+10
DNEL	2.106E+10	± 25 km Avg	5.803E+10	5.760E+10	3.160E+10
1000 NEL 874 km	5.636E+10	σ	3.067E+09	2.405E+09	2.549E+09
DNEL	3.217E+10				

M10-3
00 183 22.169

Table 44: Case M10-3

F13	↑	Kp	2.3	F10.7	169.2
DMSP Avg	7.282E+04	DMSP σ	839	# DMSP Pts	40
MLT	17.91	Fit			
	Measured Avg		2000	1000	410
2000 NEL 844 km	8.176E+10	@ DMSP Alt	7.837E+10	6.672E+10	3.166E+10
DNEL	2.019E+10	± 25 km Avg	7.854E+10	6.686E+10	3.183E+10
1000 NEL 874 km	7.001E+10	σ	4.924E+10	3.514E+09	3.619E+09
DNEL	2.334E+10				

M10-4
00 184 01.258

Table 45: Case M10-4

F14	↑	Kp	1.1	F10.7	167.9
DMSP Avg	9.413E+04	DMSP σ	2741	# DMSP Pts	22
MLT	20.77	Fit			
	Measured Avg		2000	1000	410
2000 NEL 844 km	9.325E+10	@ DMSP Alt	8.773E+10	8.352E+10	7.371E+10
DNEL	2.100E+10	± 25 km Avg	8.802E+10	8.371E+10	7.374E+10
1000 NEL 874 km	8.408E+10	σ	5.837E+09	4.928E+09	1.462E+08
DNEL	2.815E+10				

M10-5
00 184 14.354

Table 46: Case M10-5

F15	↓	Kp	1.0	F10.7	167.9
DMSP Avg	6.324E+04	DMSP σ	367	# DMSP Pts	12
MLT	10.03	Fit			
	Measured Avg		2000	1000	410
2000 NEL 844 km	6.750E+10	@ DMSP Alt	6.521E+10	6.365E+10	2.816E+10
DNEL	2.095E+10	± 25 km Avg	6.540E+10	6.376E+10	2.829E+10
1000 NEL 874 km	5.950E+10	σ	4.047E+09	3.450E+09	3.032E+09
DNEL	2.879E+10				

M10-6
00 184 21.949

Table 47: Case M10-6

F13	↑	Kp	1.0	F10.7	167.9
DMSP Avg	2.288E+04	DMSP σ	509	# DMSP Pts	21
MLT	13.01	Fit			
	Measured Avg		2000	1000	410
2000 NEL 844 km	9.517E+10	@ DMSP Alt	8.805E+10	7.956E+10	4.175E+10
DNEL	2.092E+10	± 25 km Avg	8.832E+10	7.976E+10	4.197E+10
1000 NEL 874 km	8.210E+10	σ	5.547E+09	4.972E+09	4.952E+09
DNEL	2.647E+10				

M10-7
00 185 01.055

Table 48: Case M10-7

F14	↑	Kp	2.0	F10.7	161.5
DMSP Avg	1.060E+05	DMSP σ	1892	# DMSP Pts	40
MLT	20.77	Fit			
	Measured Avg		2000	1000	410
2000 NEL 844 km	9.718E+10	@ DMSP Alt	9.510E+10	8.337E+10	5.327E+10
DNEL	2.187E+10	± 25 km Avg	9.536E+10	8.358E+10	5.346E+10
1000 NEL 874 km	8.410E+10	σ	6.410E+09	5.488E+09	4.028E+09
DNEL	2.774E+10				

Modified Error

Table 49: Case M10-7 Modified Error

	Measured Avg		2000	1000	410
2000 NEL 844 km	9.718E+10	@ DMSP Alt	9.340E+10	8.582E+10	7.567E+10
DNEL	1.846E+10	± 25 km Avg	9.368E+10	8.604E+10	7.582E+10
1000 NEL 874 km	8.410E+10	σ	6.274E+09	4.894E+09	3.859E+09
DNEL	2.193E+10				

M10-8
00 185 01.796

Table 50: Case 10-8

F15	↑	Kp	2.0	F10.7	161.5
DMSP Avg	7.736E+04	DMSP σ	3150	# DMSP Pts	32
MLT	21.38	Fit			
	Measured Avg		2000	1000	410
2000 NEL 844 km	9.149E+10	@ DMSP Alt	9.327E+10	8.075E+10	6.072E+10
DNEL	2.035E+10	± 25 km Avg	9.355E+10	8.102E+10	6.094E+10
1000 NEL 874 km	8.029E+10	σ	6.575E+09	4.873E+09	3.672E+09
DNEL	2.701E+10				

Modified Error

Table 51: Case M10-8 Modified Error

	Measured Avg		2000	1000	410
2000 NEL 844 km	9.149E+10	@ DMSP Alt	9.090E+10	8.200E+10	4.935E+10
DNEL	1.714E+10	± 25 km Avg	9.122E+10	8.223E+10	4.957E+10
1000 NEL 874 km	8.029E+10	σ	6.718E+09	5.564E+09	4.322E+09
DNEL	2.117E+10				

Appendix B: Sondrestrom Comparison

The following pages contain the numerical data used for the comparison of the Sondrestrom ISR measurements to the DMSP SSIES density measurements. Each page contains one conjunction's data and is titled using the naming convention from Section 3.

Included are:

1. DMSP satellite number
2. ↑ if the satellite is in an ascending node and ↓ if in a descending node
(This element will have a dark background if the satellite is eclipsed)
3. Kp index
4. F10.7 solar flux
5. DMSP average and standard deviation (cm^3)
6. Number of DMSP data points within the one-degree circle
7. DMSP magnetic local time
8. Measured Sondrestrom average NEL and DNEL (m^3)
9. Number of Sondrestrom radar profiles used
10. DNEL / NEL, Relative Error, and DMSP σ / DMSP Avg

The supplemental data section includes the tables, plus a plot of all the data used.

It is available upon request from the author, the advisor, or the Engineering Physics Department at the Air Force Institute of Technology.

S2-1
96 319 22.399

Table 52: Case S2-1

F12	↑	Kp	1.0	F10.7	70.0
DMSP Avg	2.422E+03	DMSP σ	1081	# DMSP Pts	6
MLT	21.59	DMSP Alt	856	SON Alt	840
SON NEL	1.436E+11	SON DNEL	1.074E+11	# SON Returns	1
<u>DNEL</u> NEL	0.7479	Relative Error	-0.9831	<u>DMSP σ</u> DMSP Avg	0.4463

S3-1
97 156 22.353

Table 53: Case S3-1

F14	↑	Kp	1.0	F10.7	76.1
DMSP Avg	1.353E+04	DMSP σ	514	# DMSP Pts	6
MLT	20.63	DMSP Alt	854	SON Alt	840
SON NEL	1.072E+11	SON DNEL	3.766E+10	# SON Returns	1
<u>DNEL</u> NEL	0.3513	Relative Error	-0.8738	<u>DMSP σ</u> DMSP Avg	0.0380

S3-2
97 157 10.319

Table 54: Case S3-2

F13	↓	Kp	0.7	F10.7	76.4
DMSP Avg	1.223E+04	DMSP σ	180	# DMSP Pts	5
MLT	8.04	DMSP Alt	856	SON Alt	840
SON NEL	1.654E+11	SON DNEL	1.537E+12	# SON Returns	2
<u>DNEL</u> NEL	9.2926	Relative Error	-0.9261	<u>DMSP σ</u> DMSP Avg	0.0147

S5-1
98 146 13.339

Table 55: Case S5-1

F14	↓	Kp	1.0	F10.7	94.9
DMSP Avg	1.945E+04	DMSP σ	203	# DMSP Pts	5
MLT	11.10	DMSP Alt	855	SON Alt	864
SON NEL	1.162E+11	SON DNEL	1.208E+12	# SON Returns	1
<u>DNEL</u> NEL	10.3959	Relative Error	-0.8326	<u>DMSP σ</u> DMSP Avg	0.0104

S6-1
98 328 22.632

Table 56: Case S5-2

F14	↑	Kp	2.7	F10.7	136.7
DMSP Avg	1.430E+04	DMSP σ	3044	# DMSP Pts	6
MLT	20.87	DMSP Alt	857	SON Alt	840
SON NEL	8.623E+11	SON DNEL	2.620E+12	# SON Returns	2
<u>DNEL</u> NEL	3.0384	Relative Error	-0.9834	<u>DMSP σ</u> DMSP Avg	0.2129

S8-1
99 343 19.952

Table 57: Case S8-1

F13	↑	Kp	3.0	F10.7	151.5
DMSP Avg	8.281E+03	DMSP σ	820	# DMSP Pts	4
MLT	17.99	DMSP Alt	854	SON Alt	872
SON NEL	4.447E+10	SON DNEL	1.009E+10	# SON Returns	2
<u>DNEL</u> NEL	0.2269	Relative Error	-0.8138	<u>DMSP σ</u> DMSP Avg	0.0990

S9-1
00 007 10.655

Table 58: Case S9-1

F13	↓	Kp	2.0	F10.7	144.8
DMSP Avg	4.653E+03	DMSP σ	672	# DMSP Pts	3
MLT	8.82	DMSP Alt	863	SON Alt	872
SON NEL	2.918E+10	SON DNEL	7.018E+10	# SON Returns	2
<u>DNEL</u> NEL	2.4051	Relative Error	-0.8405	<u>DMSP σ</u> DMSP Avg	0.1444

Appendix C: Ionospheric Layers

Table 59: Ionospheric Layers and Their Properties. From Tascione (1994) and Rees (1989)

Layer	Height/ Peak— Day (Night) (km)	Electron Conc. Noon (Night) (cm ⁻³)	Ionization Source	Important Reactions (** Rate Controlling)	Effective Recom. Coefficient α_{eff}	Neutrals Major (Minor)	Major Ions	Remarks
D	50 – 95 /90 Lower following solar flare	1.5 x 10 ⁴	Solar X-rays ($\lambda < 10 \text{ \AA}$) Lyman α (NO) ($\lambda < 1216 \text{ \AA}$) EUV (Excited O ₂) ($\lambda < 1118 \text{ \AA}$)	Photo-detachment O + O ⁻ → O ₂ + e O ⁻ + A → O + A NO Chemistry N + O + M → NO + O N + O ₂ → NO + O NO + O → N ₂ + O N ₂ ⁺ rapidly removed N ₂ ⁺ + O ₂ → N ₂ + O ₂ ⁺ O ₂ ⁺ + NO → NO ⁺ + O ₂ O ₂ ⁺ + N ₂ → NO ⁺ + NO	3 x 10 ⁻⁸	O, O ₂ , N ₂ (NO)	O ₂ ⁺ , N ₂ ⁺ , NO ⁺ O ⁻	Negative Ions v. electrons Disappears at Night Electron Attachment/ Detachment Important $\lambda = N/N_e$ ~ ω/δ (at night)

E	90 – 150 /110	1.5×10^5 ($< 1 \times 10^4$)	$h\nu < 12.0 \text{ eV}$ Corpuscular Ionization $O_2 + h\nu \rightarrow O_2^+ + e$ $N_2 + h\nu \rightarrow N_2^+ + e$ $(\lambda < 900 \text{ \AA})$ Coronal X-rays Ionize O, O_2, N_2 $(10 < \lambda < 170 \text{ \AA})$ EUV $(911 < \lambda < 1027 \text{ \AA})$	$O_2 + h\nu \rightarrow O_2^+ + e$ $(\lambda < 1027 \text{ \AA})$ $N_2 + h\nu \rightarrow N_2^+ + e$ $(\lambda < 796 \text{ \AA})$ <u>N_2^+ Disappears Fast</u> $N_2^+ + O_2 \rightarrow O_2^+ + N_2$ $k = 5 \times 10^{-10}$ $N_2^+ + O \rightarrow NO^+ + N$ $k = 10^{-10}$ Ion-Atom Interchange $O + h\nu \rightarrow O^+$ $O^+ + O_2 \rightarrow O_2^+ + O$ $k = 2 \times 10^{-11}$ $O^+ + N_2 \rightarrow N_2^+ + O$ $k = 1 \times 10^{-12}$ **	10^{-8}	O, O ₂ , N ₂	NO ⁺ , O ⁺ , O ₂ ⁺	Photo-ionization Dominant Characteristic – Molecular Ionization Ion-Atom Interchange Negative Ions Insignificant But Fast! Electron Loss D-R $N_e = \sqrt{(q/\alpha)}$ I-A $N_e = q/\beta$
---	------------------	--	---	---	-----------	------------------------------------	---	--

F ₁	140 – 200 /200	2.5 x 10 ⁵	Lyman Continuum O + hv → O ⁺ + e (λ < 911 Å) He emission lines	<p>Dissociative Recombination</p> <p>O₂⁺ + e → O + O NO⁺ + e → N + O k = 3 x 10⁻⁷</p> <p>Other Important Reactions O⁺ + N₂ → NO⁺ + N O₂⁺ + N₂ → NO⁺ + NO N₂⁺ + O → O⁺ + N₂</p>	7 x 10 ⁻⁹	O	<p>O₂⁺(Lower) O⁺(Upper) τ ≈ 60s (6 in lower) NO⁺ τ ≈ 10s Ions “locked” in atomic form Lifetimes very altitude (density) dependent At z = 150 q(O⁺) = 10³ q(O₂⁺) = 150</p>	Disappears at Night O ⁺ readily transfers charge to N ₂ and O ₂ . Result is most ionization in molecular form and disappears by dissociative recombination
----------------	-------------------	-----------------------	--	--	----------------------	---	---	--

F_2	> 220 / 300	10^6 (10^5)	Lyman Continuum $O + h\nu \rightarrow O^+ + e$ Little attenuation of radiation.	<p>Dissociative Recombination</p> $O_2^+ + e \rightarrow O + O$ $NO^+ + e \rightarrow N + O$ $k = 1 \times 10^{-7}$	$10^{-10} - 10^{-9}$ Variable, probably decreases with increasing height	O		O^+, O_2^+, N_2^+	<p>Height and e density highly variable. Large daily, seasonal and sunspot-cycle variations are combined with general erratic behavior. O^+ readily transfers charge to N_2 and O_2. Result is most ionization in molecular form and disappears by dissociative recombination, however limited by charge transfer. Peak due to a mix of ambipolar diffusion and chemical processes Diffusion Time ~ Recombination Lifetime</p>
				<p>Dissociative Recombination</p> $O_2^+ + e \rightarrow O + O$ $k = 10^{-7}$ $NO^+ + e \rightarrow N + O$ $k = 10^{-7}$					
				<p>Attachment</p> $O^+ + e \rightarrow O + h\nu$ Slow **					
				<p>Ion-Atom Interchange</p> $O^+ + O_2 \rightarrow O_2^+ + O$ $k = 10^{-12}$ $O^+ + N_2 \rightarrow NO^+ + O$ $k = 10^{-11}$					

Appendix D: The Air Force Research Laboratory Auroral Boundary Index

(Equivalent Midnight Equatorward Boundary Regression)

REGRESSIONS

The complete set of F8, F9, F10 and F11 boundaries for 1991 to 1993 were used for creating regressions for every 1-hour local time bin. A least squares fit is done with the equatorward boundary and KP value at the time of boundary. This results in a series of slopes and intercepts that can then be used to project every boundary to an "equivalent midnight" boundary. The following is the calculation for the equatorward boundary.

1) For an absolute latitude 'GLAT' and an hourly local time bin 'LT' (1-24), a provisional KP 'TKP' is calculated as follows:

$$TKP = (GLAT - INTERCEPT(LT)) / SLOPE(LT) \quad (19)$$

2) Then the equivalent midnight boundary 'EQLAT' can then be calculated as follows:

$$EQLAT = INTERCEPT(24) + SLOPE(24) * TKP \quad (20)$$

NOTE: You may notice that MLT bins of 11 to 15 have no observations and no correlation. That is because the boundaries in this local time range do not correlate well with KP and are flagged accordingly. The regression values listed are based on 'hand' fitting.

Table 60: EQB Regression Statistics

MLT	#OBS	SLOPE	INTERCEPT	CORRELATION
1	1066.	-1.65	66.54	-0.749
2	1075.	-1.45	66.35	-0.685
3	1649.	-1.64	66.01	-0.783
4	2717.	-1.82	66.97	-0.798
5	7533.	-1.79	66.70	-0.742
6	15000.	-1.81	67.62	-0.770
7	9132.	-1.65	68.23	-0.728
8	6535.	-1.47	69.11	-0.689
9	7754.	-1.34	69.73	-0.650
10	1675.	-1.24	69.99	-0.624
11	-1.	-1.19	70.50	0.000*
12	-1.	-1.15	71.00	0.000*
13	-1.	-1.10	72.50	0.000*
14	-1.	-1.05	73.00	0.000*
15	-1.	-1.10	73.50	0.000*
16	2338.	-1.15	74.02	-0.646
17	4945.	-1.45	73.64	-0.747
18	6017.	-1.48	72.43	-0.761
19	11980.	-1.74	71.79	-0.823
20	12274.	-1.85	70.88	-0.827
21	12212.	-1.73	69.74	-0.801
22	6681.	-2.02	69.34	-0.837
23	5051.	-1.93	67.90	-0.849
24	3101.	-1.71	66.78	-0.789

(Rich, private communication, 19 October, 2000)

Bibliography

- Anderson, P. C., R. A. Heelis, and W. B. Hanson. "The Ionospheric Signatures of Rapid Subauroral Ion Drifts," Journal of Geophysical Research, vol 96, No. A4: pp. 5785 -5792 (April 1, 1991)
- Bruzak, A. and C. J. Durrant, Illustrated Glossary for Solar and Solar-Terrestrial Physics, Dordrecht, Holland: D. Reidel Publishing Company, 188-193 (1977).
- CEDAR Database User's Guide, n. pag. <http://cedarweb.hao.ucar.edu>, November 1998.
- Erickson, P.J., "The Millstone Hill Observatory," n. pag. http://www.haystack.mit.edu/mhrobs/instrument_summary.html#MHISR. 21 June 1995
- Erickson, P.J., "POLITE Campaign Home Page" n. pag. <http://www.haystack.edu/polite/index.html> 21 June 1997
- Evans, J. V. "Theory and Practice of Ionosphere Study by Thompson Scatter Radar," Proceedings of the IEEE, 57: 504 (April 1969).
- Evans, J. V. "High-Power Radar Studies of the Ionosphere," Proceeding of the IEEE, Vol. 62, No. 12: 1636-1650 (December, 1975)
- Greenspan, M. E., W. J. Burke, F. J. Rich, W. J. Hughes, and R. A. Heelis. "DMSP F8 Observation of the Mid-latitude and Low-latitude Topside Ionosphere Near Solar Minimum," Journal of Geophysical Research, Vol. 99, No. A3, pp 3817-3826 (1 March 1994).
- Gussenhoven, M.S., D.A. Hardy, N. Heinemann, and E. Holeman, 1978 Diffuse Auroral Boundaries and a Derived Auroral Boundary Index, AFGL-TR-82-0398, Air Force Geophysics Laboratory, Hanscom AFB, MA, (ADA130175), 1982
- Hargreaves, J. K. The Solar-Terrestrial Environment, London: Cambridge University Press, 1992.
- Miller, N. J. "The Main Electron Trough During the Rising Solar Cycle," Journal of Geophysical Research, Space Physics, Vol. 75, No. 34, 7175-7181, (1 December, 1970)
- Press, W. H., S. A. Teukolsky, W. T. Vetterling, and B. P. Flanery. Numerical Recipes in Fortran 90: The Art of Parallel Scientific Computing, New York: 1996.
- Rees, M. H. Physics and Chemistry of the Upper Atmosphere, London: Cambridge University Press, 1989.

- Rich, F. Users Guide for the Topside Ionospheric Plasma Monitor (SSIES, SSIES-2, and SSIES-3) on Spacecraft of the Defense Meteorological Satellite Program (DMSP). Volume 1: Technical Description, PL-TR-94-2187: (June 1994)
- Rich, F. "DMSP: General Information, Data Availability and SSIES - Thermal Plasma & Electric Field," n. pag <http://www-vsbg.plh.af.mil/projects/dmsp/dmspssies.html>: 4 October 2000.
- Rishbeth, H. "Basic Physics of the Ionosphere: A Tutorial Review," Journal of the Institution of Electronic and Radio Engineers, Vol. 58, No. 6 (Supplement), S207 - S223. (September - December 1988)
- Schunk, R. W., P. M. Banks, and W. J. Raitt, "Effects of Electric Fields and Other Processes Upon the Nighttime High-Latitude F Layer," Journal of Geophysical Research, Vol. 81, No. 19, 3271 - 3282 (1 July, 1976).
- Schunk, R. W., and A. F. Nagy. Ionospheres: Physics, Plasma Physics, and Chemistry, New York: Cambridge University Press, 2000.
- Schunk, R. W., and J. J. Sojka. "Global Assimilation of Ionospheric Measurements Proposal," Utah State University, 1999.
- SRI, Inc. "Map of Existing and Planned Incoherent Scatter Facilities," <http://isr.sri.com/iono/issnetwk.html>: 2000.
- Sultan, P. J., and F. J. Rich. "Validation of DMSP SSIES Ion Density Measurements with Ground-Based Incoherent Scatter Radar," Draft Manuscript [2000]
- Tascione, T. F. An Introduction to the Space Environment, Second Edition, Malabar, FL: Krieger Publishing Co., 1994
- Taylor, H. A., Jr. "The Light Ion Trough," Planetary Space Science, 20, pp. 1593 - 1605 1972.
- Taylor, J. R. An Introduction to Error Analysis: The Study of Uncertainty in Physical Measurements, Sausalito, CA: University Science Books, 1982.
- West, K. H., and R. A. Heelis. "Longitudinal Variations in Ion Composition in the Morning and Evening topside Equatorial Ionosphere Near Solar Minimum," Journal of Geophysical Research, Vol. 101, No. A4, 7591 - 7960 (1 April, 1996).

Vita

Captain Herbert L. Keyser was born on in Sellersville, Pennsylvania, and graduated with honors from Souderton Area High School in Souderton, Pennsylvania in June 1983. He enlisted in the Air Force in May 1984 as an Airborne Computer/Display Maintenance Technician on the E-3 Airborne Warning and Control System. He was selected for the Airman Education and Commissioning Program and entered the Florida State University in April 1993. He graduated summa cum laude with a Bachelor of Science in Meteorology, and received his commission from the Air Force Officer Training School in November 1995.

His first weather assignment was at Misawa AB, Japan, as an Operational Meteorologist in January 1996. In August 1999, he entered the Graduate School of Engineering and Management, Air Force Institute of Technology. Upon graduation, he will be assigned to the Air Force Weather Agency in Offutt AFB, Nebraska.

REPORT DOCUMENTATION PAGE				<i>Form Approved</i> OMB No. 074-0188	
The public reporting burden for this collection of information is estimated to average 1 hour per response, including the time for reviewing instructions, searching existing data sources, gathering and maintaining the data needed, and completing and reviewing the collection of information. Send comments regarding this burden estimate or any other aspect of the collection of information, including suggestions for reducing this burden to Department of Defense, Washington Headquarters Services, Directorate for Information Operations and Reports (0704-0188), 1215 Jefferson Davis Highway, Suite 1204, Arlington, VA 22202-4302. Respondents should be aware that notwithstanding any other provision of law, no person shall be subject to a penalty for failing to comply with a collection of information if it does not display a currently valid OMB control number.					
PLEASE DO NOT RETURN YOUR FORM TO THE ABOVE ADDRESS.					
1. REPORT DATE (DD-MM-YYYY) 03-01-2001		2. REPORT TYPE Master's Thesis		3. DATES COVERED (From - To) Aug 2000 - Mar 2001	
4. TITLE AND SUBTITLE VALIDATION AND CHARACTERIZATION OF IONOSPHERIC DENSITIES MEASURED BY DMSP				5a. CONTRACT NUMBER 5b. GRANT NUMBER 5c. PROGRAM ELEMENT NUMBER 5d. PROJECT NUMBER 5e. TASK NUMBER 5f. WORK UNIT NUMBER	
6. AUTHOR(S) Keyser, Herbert L., Captain, USAF				8. PERFORMING ORGANIZATION REPORT NUMBER AFIT/GAP/ENP/01M-05	
7. PERFORMING ORGANIZATION NAMES(S) AND ADDRESS(S) Air Force Institute of Technology Graduate School of Engineering and Management (AFIT/EN) 2950 P Street, Building 640 WPAFB OH 45433-7765				10. SPONSOR/MONITOR'S ACRONYM(S) 11. SPONSOR/MONITOR'S REPORT NUMBER(S)	
9. SPONSORING/MONITORING AGENCY NAME(S) AND ADDRESS(ES) HQ Air Force Weather Agency Space Weather Operations Center (HQ AFWA/XOGS) 106 Peacekeeper Drive Ste 2N3 Offutt AFB, NE 68113				12. DISTRIBUTION/AVAILABILITY STATEMENT APPROVED FOR PUBLIC RELEASE; DISTRIBUTION UNLIMITED.	
13. SUPPLEMENTARY NOTES					
14. ABSTRACT Future models of the thermosphere-ionosphere-magnetosphere system will require near real-time assimilation of ionospheric parameters to specify and forecast these regions. One of the current sensors that will be used in the GAIM model is the DMSP SSIES. Knowledge of the SSIES's reliability and data characteristics is key to using the data when relying on automated processes to ingest the data. To validate the DMSP value, the DMSP-measured density is compared to ground-based ISR measurements from solar minimum to solar maximum. The DMSP data are compared to data from the ISRs located at the Millstone Hill Observatory in Massachusetts and Sondrestrom in Greenland. The DMSP was found to measure densities 10 percent - 20 percent lower than Millstone Hill and 90 percent lower than Sondrestrom, however both were within the uncertainties of the ISR measurements. The DMSP data over Millstone Hill were analyzed for variability. After de-trending the data, the variability was found to range from 0.2 percent in geomagnetically quiescent periods to over 20 percent during active periods.					
15. SUBJECT TERMS Topside Ionosphere, Plasma Density, Incoherent Scatter Radar (ISR), Defense Meteorological Satellite Program (DMSP), Topside Plasma Monitor (SSIES), Millstone Hill, Sondrestrom, Coupling Energetics and Dynamics of Atmospheric Regions (CEDAR), Global Assimilation of Ionospheric Measurements (GAIM)					
16. SECURITY CLASSIFICATION OF:		17. LIMITATION OF ABSTRACT		18. NUMBER OF PAGES	
a. REPORT U	b. ABSTRACT U	c. THIS PAGE U	UU	136	19a. NAME OF RESPONSIBLE PERSON Maj D. J. Della-Rose, ENP 19b. TELEPHONE NUMBER (Include area code) (937) 255-3636, ext 4514

Standard Form 298 (Rev. 8-98)
 Prescribed by ANSI Std. Z39-18

	<i>Form Approved</i> OMB No. 074-0188
--	---